IMPROVED SIMULATION OF NATURALLY FRACTURED RESERVOIRS USING UNSTRUCTURED GRIDS AND MULTI-RATE DUAL-POROSITY MODELS

CHRISTINE MAIER

Submitted for the degree of Doctor of Philosophy

Institute of Petroleum Engineering

Heriot-Watt University

November 2014

To my wonderful family.

ABSTRACT

Naturally Fractured Reservoirs (NFR) hold about half of the world's remaining oil reserves and are typically very heterogeneous. NFR are also important for many other subsurface engineering applications including (nuclear) waste storage, CO_2 sequestration, groundwater aquifers, and geothermal energy extraction. They contain faults, fracture corridors, large fractures but also many small-scale fractures as well as a heterogeneous rock matrix. Multi-phase flow in NFR is strongly influenced by this multi-scale heterogeneity. Therefore, accurate conceptual models that reliably quantify fluid flow in NFR are needed.

In this thesis, three important contributions are made towards an improved simulation of multi-phase flow processes in NFR. First, the Implicit Pressure Implicit Saturation (IMPIS) method using unstructured grids was implemented to numerically simulate two-phase flow in a Discrete Fracture and Matrix (DFM) model. Second, a Multi-Rate Dual-Porosity (MRDP) model was developed including fracture-matrix transfer functions that are based on analytical solutions for spontaneous imbibition and gravity drainage. Finally, the two approaches were combined to a DFM-MRDP model. This model represents the multi-scale heterogeneity inherent to NFR more accurately by resolving fluid-flow processes in large-scale fractures directly using the DFM model while accounting for complex matrix heterogeneities when modelling fluid exchange between small-scale fractures and rock matrix using the MRDP model.

PUBLICATIONS

This thesis contains excerpts from the following papers:

- Crutchley, G.J., Berndt, C., Geiger, S., Klaeschen, D., Papenberg, C., Klaucke, I., Hornbach, M.J., Bangs, N.L.B., & **Maier, C.**, Drivers of focused fluid flow and methane seepage at south Hydrate Ridge, offshore Oregon, USA. Geology, 41(5), pp.551-554, March 2013.

- **Maier, C.**, Schmid, K. S., Ahmed Elfeel, M., & Geiger, S., Multi-Rate Mass-Transfer Dual-Porosity Modelling Using the Exact Analytical Solution for Spontaneous Imbibition. SPE-164926, In SPE Europec/EAGE Annual Conference, London, UK, June 2013.

- **Maier, C.**, & Geiger, S., Combining Unstructured Grids, Discrete Fracture Representation and Dual-Porosity Models for Improved Simulation of Naturally Fractured Reservoirs. SPE 166049, In SPE Reservoir Characterisation and Simulation Conference, Abu Dhabi, UAE, September 2013.

- Ahmed Elfeel, M., Agada, S., **Maier, C.**, & Geiger, S., Integrating Discrete Fracture Models for Static and Dynamic Calibration of Fractured Reservoirs. Th E103 05, 76th EAGE Conference and Exhibition, Amsterdam, Netherlands, June 2014.

One never notices what has been done,
one can only see what remains to be done.

— Marie Curie

ACKNOWLEDGMENTS

Many people have helped me on this journey and I am here to thank them. First of all, I want to thank Sebastian for his tremendous support and believe in his students. Thank you for your supervision, for your encouragements exactly then, when they were needed and for your leading by example work style.
Second, I take this opportunity to sincerely acknowledge the itf-ISF consortium and thank my sponsors from ConocoPhilips, ExxonMobil, OMV, Saudi Aramco and Total for funding this PhD and for all your comments, suggestions and questions which influenced this work a lot. Dual-Porosity models were not on the agenda at the beginning of my journey, but I am glad I took this path as it led me to the DFM-MRDP model. Thanks goes also to the academic members of itf-ISF, especially to the MU Leoben group which who I was working closely together.
I also would like to thank ExxonMobil Research Alliance $(FC)^2$, for giving me the opportunity to attend their meetings and present my work. Thanks to Susan for being always kind, helpful and so inspiring. I also want to take the opportunity and thank Enrique Rosero, Sonja Boorman, Gregory Benson, Camille Casey and Luke Shafer for the great time during my internship in Houston at EMURC.
I thank CMG Reservoir Simulation Foundation for inviting me twice to Canada. The weekend trip Edinburgh-Vancouver-Edinburgh was one of my most adventurous journeys so far.
I also would like to thank Matthew Jackson from Imperial College London and Florian Dorster for being my examiners. Thank you for the motivating and inspiring discussions during the viva and for making it a really enjoyable day.
A huge Thank You goes to my second family, the previous and present members of EA1.16. Karen, I am so fortunate that we both not only share a 'passion' for spontaneous imbibition but also a great friendship. Yan, thank you for practising Russian with me and for inviting me to all the concerts. Adnan, for being always kind and for visiting us on a regular basis. Very special thanks goes to Claudia who actually convinced me to apply for this PhD position. Claudia, without you, not a single word of this work would exist. Robert, for all the chats about almost everything and for being my soul mate. Mohamed and Simeon for the great collaboration and exchange of ideas but also for your tutorials on Eclipse. Thanks to Qing for spending some weekends with me in EA1.16 especially that day,

when I forgot my keys. Alessandro, thank you for teaching me Italian properly and for your cheerfulness. Shanti thanks for organising the BBQ and other come-togethers. I really enjoyed our last hand crafting session and we should repeat it soon. I should not forget Daniel, Rafael, Adnan, Tianshen and Zhao who joined our group recently, thank you for all the coffee breaks. I am really fortunate to have met such bright and great people who became true friends. You will be truly missed!

Last but not least, the biggest thanks go to Denis, my friends in Germany and UK - you know who you are - and my family for all the support during the last years, and especially to my little niece who does not realise yet how helpful she was by sending me so much positive energy on the darkest winter days.

Edinburgh, November 2014

ACADEMIC REGISTRY
Research Thesis Submission

Name*:*	Christine Maier		
School/PGI:	IPE		
Version: *(i.e. First, Resubmission, Final)*	Final	Degree Sought (Award **and** Subject area)	PhD in Petroleum Engineering

Declaration

In accordance with the appropriate regulations I hereby submit my thesis and I declare that:

1) the thesis embodies the results of my own work and has been composed by myself
2) where appropriate, I have made acknowledgement of the work of others and have made reference to work carried out in collaboration with other persons
3) the thesis is the correct version of the thesis for submission and is the same version as any electronic versions submitted*.
4) my thesis for the award referred to, deposited in the Heriot-Watt University Library, should be made available for loan or photocopying and be available via the Institutional Repository, subject to such conditions as the Librarian may require
5) I understand that as a student of the University I am required to abide by the Regulations of the University and to conform to its discipline.

* *Please note that it is the responsibility of the candidate to ensure that the correct version of the thesis is submitted.*

Signature of Candidate*:*		Date:	

Submission

Submitted By *(name in capitals):*	
Signature of Individual Submitting:	
Date Submitted:	

For Completion in the Student Service Centre (SSC)

Received in the SSC by *(name in capitals):*			
Method of Submission *(Handed in to SSC; posted through internal/external mail):*			
*E-thesis Submitted (**mandatory for final theses)***			
Signature:		Date:	

Please note this form should bound into the submitted thesis.

Updated February 2008, November 2008, February 2009, January 2011

CONTENTS

LIST OF FIGURES

LIST OF TABLES

ACRONYMS

CFL Courant-Friedrich-Lewy

CPU Central Processing Unit

CSMP++ Complex Systems Modelling Platform

DF Discrete Fracture

DFM Discrete Fracture and Matrix

DFN Discrete Fracture Network

DP Dual-Porosity

DPDP Dual-Porosity-Dual-Permeability

EOR Enhanced Oil Recovery

FD Finite Difference

FDM Finite Difference Method

FE Finite Element

FEM Finite Element Method

FEFV Finite Element - Finite Volume

FV Finite Volume

FVM Finite Volume Method

IMPES Implicit Pressure Explicit Saturation

IMPIS Implicit Pressure Implicit Saturation

MC Multiple Continua

MINC Multiple Interacting Continua

MRDP Multi-Rate Dual-Porosity

MRMT Multiple Rate Mass Transfer

MSR Multiple Sub-Region

NAPL Non-Aqueous Phase Liquids

NFR Naturally Fractured Reservoirs

PDE Partial Differential Equation

SCAL Special Core Analysis

SRDP Single-Rate Dual-Porosity

SP Single-Porosity

WAG Water-Alternating-Gas

1

INTRODUCTION

Fractures and faults are generated by large-scale tectonic events through folding, faulting and uplift but also through subsidence of sediments, erosion, excess fluid pressures, and thermal chemical action over geological time (Kazemi and Gilman, 1993; Odling et al., 1999). They are ubiquitous in almost all outcrops of geological formation highlighting their prevalence in many subsurface reservoirs (Fig. 1.1) (Nelson, 2001; Narr et al., 2006; Agar et al., 2010). Today, many oil companies adopt the approach that a reservoir is assumed to be fractured until proven otherwise. Fractures often comprise the main flow conduit for migration of hydrothermal fluids in geothermal systems, water and contaminants in groundwater systems, radioactive and toxic industrial waste in subsurface storage sites, and hydrocarbons in petroleum reservoirs. In contrast, the rock matrix is the main storage for fluids (Berkowitz, 2002). If mass transfer between fractures and the rock matrix is slow, fluids (e.g. oil, contaminants, brine) are left behind in the matrix. The latter is particularly problematic in fractured carbonate reservoirs, which host over 50% of the world's remaining hydrocarbon reserves but suffer from very low recovery factors (Montaron, 2008). A similar argument can be made for shale gas reservoirs which revolutionised gas production in the US (e.g., Warpinski et al., 2008; Dershowitz et al., 2011; Patzek et al., 2013). Here production occurs mainly from the hydraulic fractures and gas is left behind in the tight rock matrix.

Understanding multi-phase flow in fractured porous media is therefore important for many applications including but not limited to, CO_2 storage, ground water remediation and enhanced/improved oil recovery. For CO_2 sequestration, it is important to know how readily CO_2 will enter the rock matrix and how

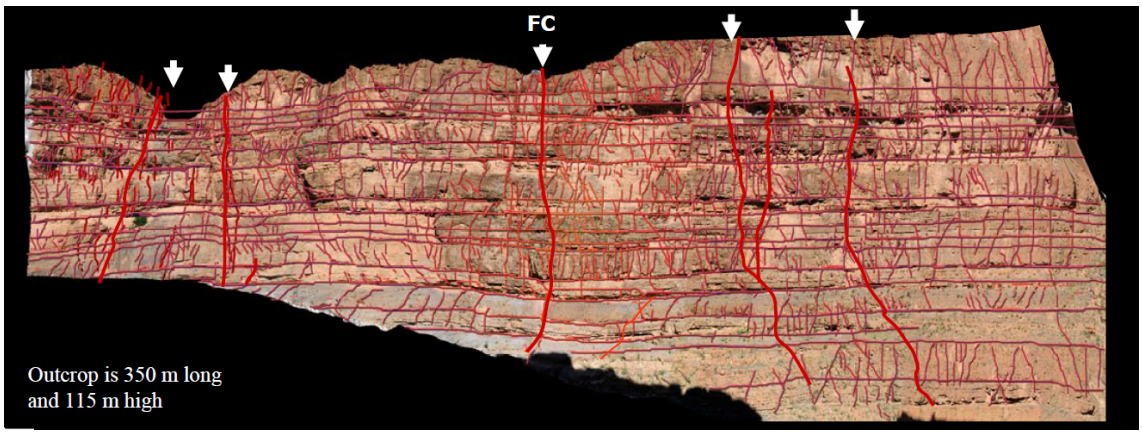

Figure 1.1: Interpretation of fracture traces of a Jurassic Carbonate Ramp outcrop from the High Atlas, Morocco. The horizontal lines represent the bed boundaries. Fractures are represented by vertical lines. Thick red lines indicate the locations of fracture corridors (Agar et al., 2010).

much CO_2 will be trapped in the matrix (e.g., Bond et al., 2013; Civile et al., 2013; Oh et al., 2013). For groundwater contamination, it is more of interest to understand how fast and efficient Non-Aqueous Phase Liquids (NAPL) can be removed from the rock while injecting water, surfactants or steam (e.g., Meinardus et al., 2002; Huyakorn et al., 1994; Ochs et al., 2010). Similarly, efficient and economic hydrocarbon production from fractured reservoirs rely greatly on the injection cycles of aqueous and gaseous phase fluids to exploit capillary and gravitational forces to sweep oil towards the production wells (e.g., Denoyelle et al., 1988; Christensen et al., 2001; Panda et al., 2009). For example, an early water breakthrough has a negative influence on the oil recovery volumetric sweep efficiency as water production competes directly with oil production (Sydansk and Romero-Zeron, 2011). Selecting the appropriate injection strategy is therefore crucial to maximise the recovery of contaminants and hydrocarbons, and to optimise CO_2 storage. Injection strategies are typically evaluated using numerical simulations, hence good conceptual models and fast numerical algorithms are needed. This thesis focusses on oil recovery applications in Naturally Fractured Reservoirs (NFR) but results are equally applicable to other scenarios in NFR such as groundwater remediation or CO2 storage or multiphase flow in hydraulically fractured formations.

1.1 RESERVOIR SIMULATION MODELS

Models for multi-phase flow simulations in fractured reservoirs can be classified into three groups listed in order of their accuracy of fracture representation and their numerical complexity:

1. Single Porosity Models
2. Multiple Continua Models
3. Discrete Fracture Models

These models are briefly described in the next sections.

1.1.1 *Single-Porosity Models*

The Single-Porosity (SP) model is characterised by its 'simplicity' and is therefore available in all simulators. The grid cells are populated with averaged properties obtained by applying suitable upscaling techniques treating the fractures as an equivalent porous medium (e.g., Dershowitz et al., 2000; Cosentino et al., 2001; Matthai and Nick, 2009; Ahmed Elfeel et al., 2010; Lemonnier and Bourbiaux, 2010; Hui et al., 2013; Ahmed Elfeel et al., 2014). The simulation is then performed on a model with spatially varying petrophysical properties but without special treatment of the fractures, as they are represented by equivalent permeabilities and porosities (Fig. 1.2). Faults and large fractures are commonly modelled through transmissibility multipliers. This approach is also often used in the simulations of shale gas reservoirs (Fig. 1.3) (Warpinski et al., 2008).

1.1.2 *Multiple Continua Models*

The Multiple Continua (MC) models take into account that the flow in NFR occurs on different time scales. MC models assume that the matrix comprises the main storage of the fluids while the main flow capacity is contributed by the fractures.

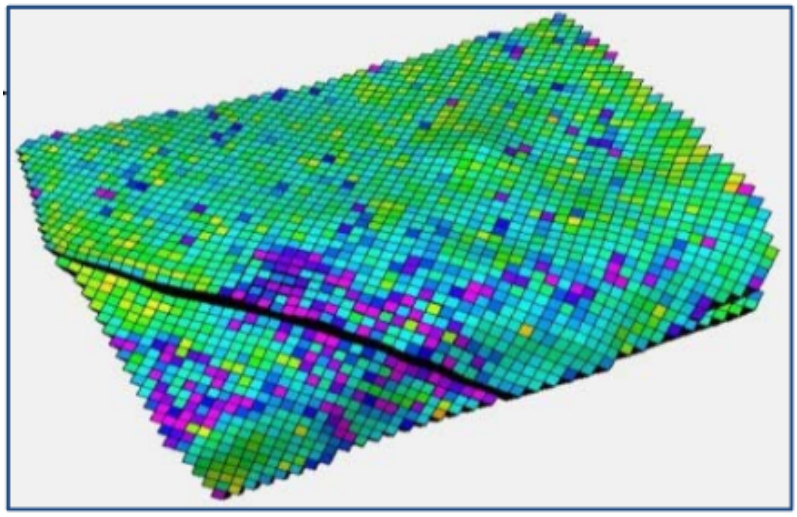

Figure 1.2: Structured grid representation of the Tensleep formation in the Teapot Dome Field in Wyoming, USA. The field comprises a well connected fracture network. Grid cells are populated with upscaled fracture permeabilities, ready for Single-Porosity (SP) simulations. The values of the upscaled fracture permeabilities ranges over three order of magnitude (Ahmed Elfeel et al., 2013).

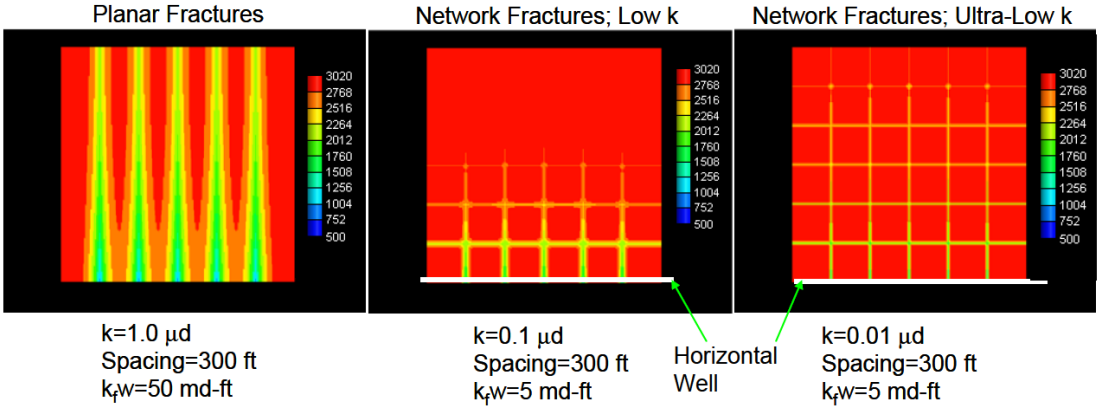

Figure 1.3: Single-Porosity (SP) simulation of pressure depletion in a hydraulically fractured tight sandstone reservoir with matrix permeability of $K = 1.0\ \mu D$ (left) and low permeability shale reservoir with $K = 0.1\ \mu D$ (centre) and $K = 0.01\ \mu D$ (right). Fractures are modelled through their conductivity $K_f w$. After three months the tight sandstone reservoir provides an efficient drainage whereas the shale reservoir simulations show a limited depletion (Warpinski et al., 2008).

Therefore, fractures and matrix are treated separately as overlapping continua coupled via a mathematically derived or experimentally quantified transfer function. This transfer function describes the rate of fracture-matrix fluid transfer. A general transfer function was introduced by Lu et al. (2008) which accounts for the four principal drives for fracture-matrix fluid exchange, i.e. (1) spontaneous counter-current imbibition, (2) gravity drainage, (3) fluid expansion and (4) diffusion (Fig. 1.4). This thesis will mainly focus on the two most dominant oil recovery mechanisms, spontaneous imbibition and gravity drainage, and will use a slightly different formulation of the Lu et al. (2008) transfer function as proposed by Di Donato et al. (2007). In this formulation, spontaneous counter-current imbibition and gravity drainage will be treated separately. Another difference is that a new, general scaling group (Schmid and Geiger, 2012, 2013) that is based on an analytical solution of spontaneous imbibition (Fig. 1.5) (McWhorter and Sunada, 1990) is used for the evaluation of fluid exchange rate due to spontaneous counter-current imbibition (see Chapter 3).

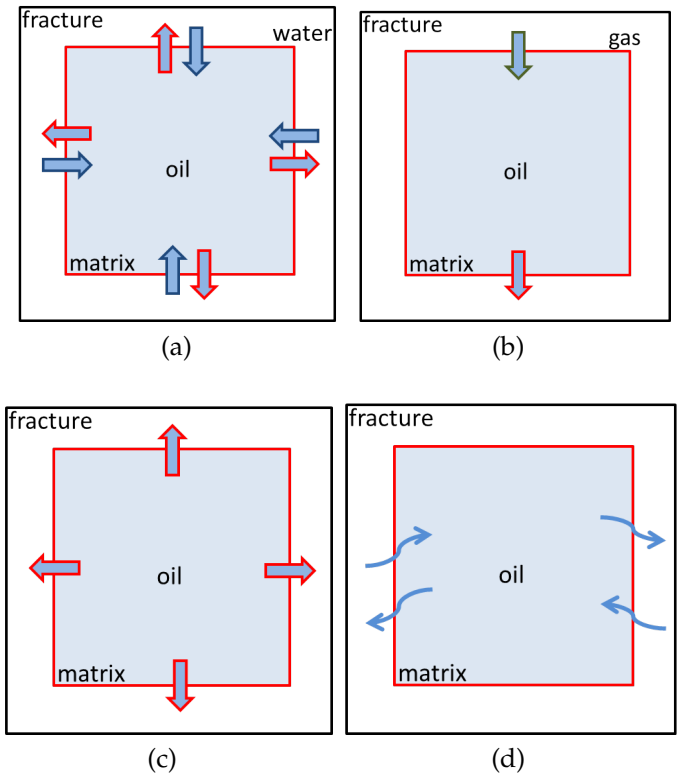

Figure 1.4: Four principle recovery mechanism from rock matrix surrounded by fractures after Lu et al. (2008): spontaneous counter-current imbibition (a), gravity drainage (b), fluid expansion (c) and diffusion (d).

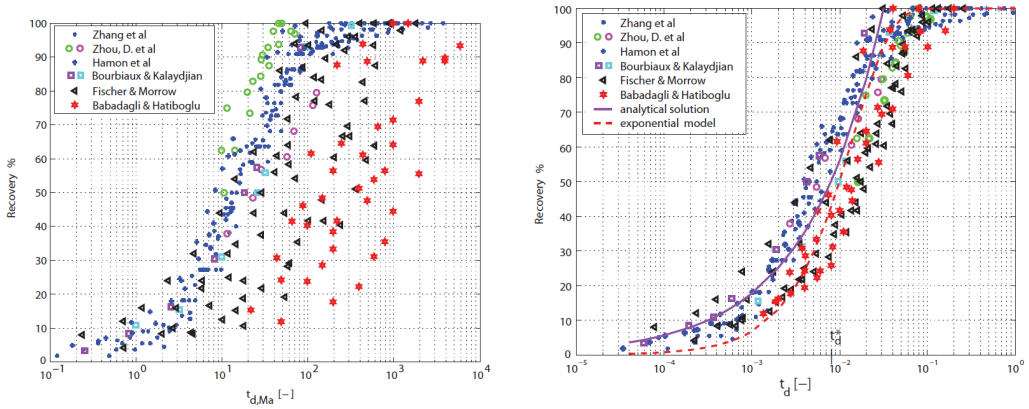

(a) (b)

Figure 1.5: Scaling of over 40 published imbibition studies using the scaling group after Ma et al. (1997) (a) and the general scaling group that is based on analytical solution of spontaneous imbibition after Schmid and Geiger (2012). General scaling group captures all physics and correlated experimental results fall into one master curve. Scaling with the Ma scaling group does not result in collapse of the experimental data into one curve and is therefore not applicable for arbitrary rock and fluid properties.

1.1.2.1 *Dual-Porosity Model*

The Dual-Porosity (DP) model is the origin of the MC models. It was first introduced for single phase flow by Barenblatt et al. (1960) and Warren and Root (1963) and later extended to two phase flow by Mattax and Kyte (1962). Since then, many authors contributed to the improvement of the model (e.g., Kazemi et al., 1976; Gilman and Kazemi, 1983; Quandalle and Sabathier, 1989; Lu et al., 2008) by introducing new transfer functions for two- and three-phase systems. By using a transfer function, the rock matrix is only 'virtual', by being modelled as source/sink term that adds/removes fluids from the fractures. Fluid flow is only simulated in the fractures. These transfer functions include new shape factors to account for fracture spacing and new transfer rate coefficients based on the calculation of fluid potentials in the matrix blocks. The standard DP model assumes uniform rock and fluid properties within one simulation grid cell, which means all matrix blocks within a grid cell have the same size and the same petrophysical properties. However, shape factor and matrix properties can vary from grid cell to grid cell.

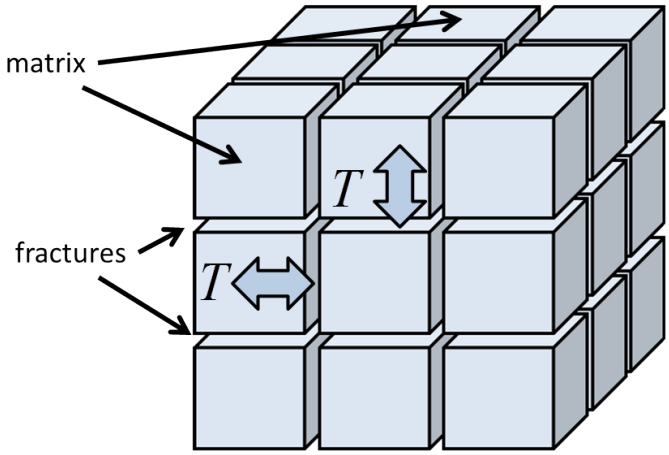

Figure 1.6: Conceptual representation of one grid cell represented by a Dual-Porosity (DP) model. The DP model assumes uniformly distributed matrix blocks. Fracture - matrix fluid exchange is computed via a transfer function T.

1.1.2.2 *Dual-Porosity-Dual-Permeability Model*

The Dual-Porosity-Dual-Permeability (DPDP) model represents both the fracture-matrix fluid exchange and also the interaction between two adjacent matrix blocks in case of capillary continuity between them (Hill and Thomas, 1985; Fung, 1991). In addition to the DP model, this model therefore includes a second grid which simulates fluid flow in the rock matrix. As a consequence, the DPDP model requires much more computational time than DP models (Gilman and Kazemi, 1988). However, the matrix-matrix transfer is important for modelling gravity drainage processes. Neglecting capillary continuity and reimbibition processes would lead to significant over-predictions of recoveries (Fung, 1991).

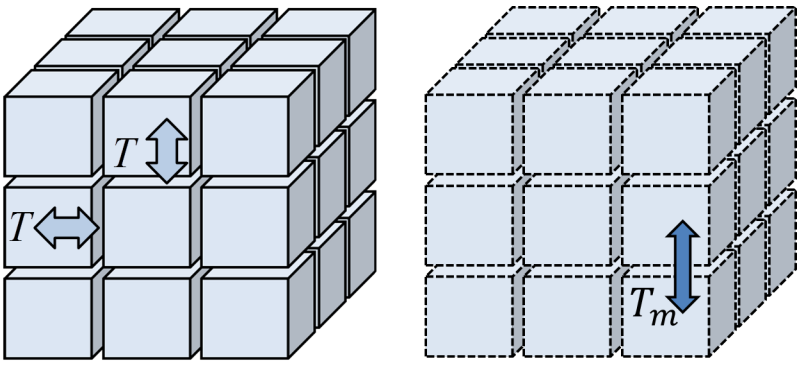

Figure 1.7: Conceptual representation of one grid cell represented by a Dual-Porosity-Dual-Permeability (DPDP) model. The DPDP model assumes uniformly distributed matrix blocks. Fracture - matrix fluid exchange is computed via a transfer function T. Matrix - matrix fluid transfer is computed on a virtual grid via a transfer function T_m.

1.1.2.3 *Multiple Interacting Continua Model*

The Multiple Interacting Continua (MINC) model resolves pressure and saturation gradients in the rock matrix blocks by discretising the matrix block using concentric shells. Each shell can have its individual saturation and/or pressure value and hence steep gradients in (S, p) can be observed, which is important early on in the field life (Saidi, 1983; Pruess and Narasimhan, 1985; Gilman, 1986; Beckner et al., 1991). Flow across the shells is simulated using the SP model. Fluid transfer between fracture and the outer matrix shell is again modelled with a transfer function as in the DP model. The idea of the MINC approach was later extended to the Multiple Sub-Region (MSR) model for Discrete Fracture Network (DFN) upscaling (e.g., Gong and Durlofsky, 2006; Karimi-Fard et al., 2006; Hui et al., 2007, 2008, 2013) (see Section 1.1.4).

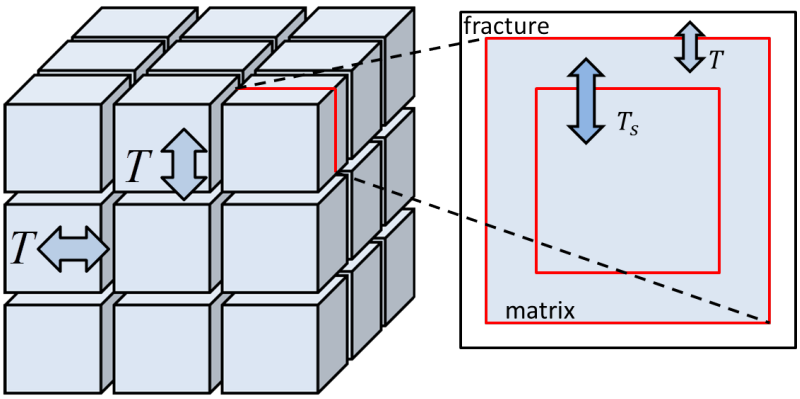

Figure 1.8: Conceptual representation of one grid cell represented by a Multiple Interacting Continua (MINC) model. The MINC model assumes uniformly distributed matrix blocks which are discretised into concentric shells. Fracture - outer shell fluid exchange is computed via a transfer function T. Flow across the shells within the matrix block is simulated using the SP model (T_S).

1.1.2.4 *Multi-Rate Dual-Porosity Model*

The Multi-Rate Dual-Porosity (MRDP) model incorporates the effect of small-scale heterogeneities (e.g., matrix block sizes, permeability, porosity, wettability) which are present below the size of a typical reservoir simulation grid cell and nevertheless can impact the recovery. These small scale heterogeneities lead to different rates at which the fracture and matrix exchange fluid. To resolve this multi-rate behaviour a distribution of transfer rates, rather than one averaged transfer rate, is applied. Haggerty and Gorelick (1995) pioneered the MRDP

model by developing a Multiple Rate Mass Transfer (MRMT) model for single-phase solute transport with mobile and immobile domains. The advantage of the MRMT model was demonstrated by performing tracer tests in fractured dolomite formations. The different transfer rates between the mobile fractures and immobile matrix typically cannot be averaged in a straightforward manner. Furthermore, predicted breakthrough curves can differ by orders of magnitude for observed areas if only a single-rate model is assumed (Fig. 1.10) (Haggerty et al., 2001). The MRDP model was introduced in the petroleum literature for multi-phase flow simulations by Di Donato et al. (2007) and more recently by Geiger et al. (2013) and Maier et al. (2014) (see Chapter 4).

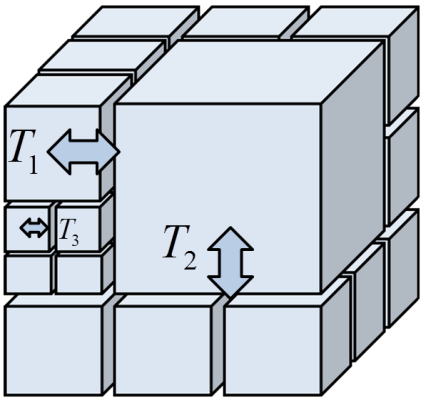

Figure 1.9: Conceptual representation of one grid cell represented by a Multi-Rate Dual-Porosity (MRDP) model. The MRDP model captures sub-grid heterogeneities by not assuming uniform properties. Multiple transfer functions for fracture-matrix fluid exchange computation, representing for example different shape factors, can be present in a single grid cell.

1.1.3 *Discrete Fracture Models*

The Discrete Fracture (DF) models represent the fractures and faults explicitly as geometrical bodies which is the main difference to the SP and the MC model. Darcy flow is now computed in the fractures in a SP manner. This means that each fracture has a permeability and porosity that is consistent with its aperture. DF models can be divided into two groups, Discrete Fracture Network (DFN) model and the Discrete Fracture and Matrix (DFM) model. Typically a DFN is generated using observation data such as well logs, well tests, seismic data, and outcrop analogues (e.g., Sabathier et al., 1998; Dershowitz et al., 2000; Berkowitz, 2002; Gauthier et al., 2002; Narr et al., 2006; Bourbiaux, 2010). DFNs can hence be

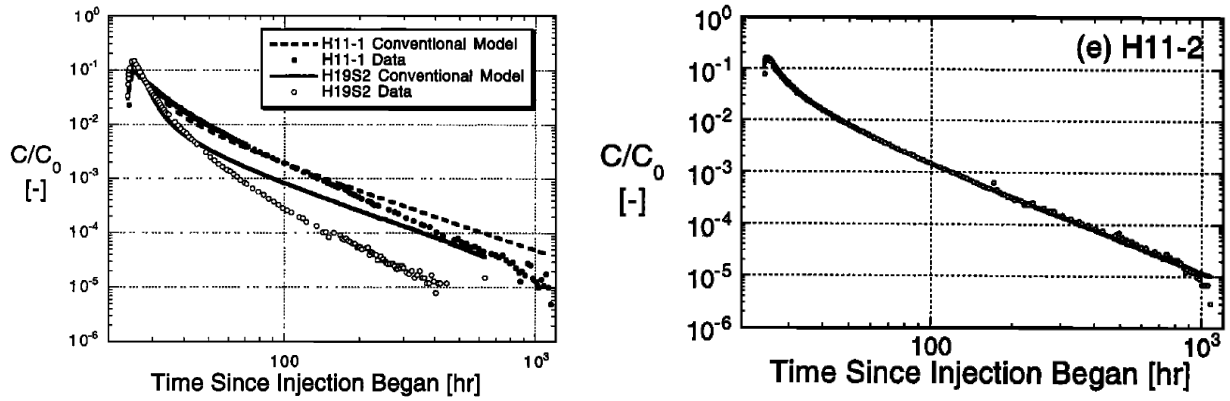

(a) (b)

Figure 1.10: Recovery curves from single-well injection-withdrawal tests conducted in a fractured dolomite simulated with the conventional Dual-Porosity (DP) model (a) and with the Multiple Rate Mass Transfer (MRMT) model (b). The multi-rate diffusion model predicts the recovery curves exceptionally well whereas the DP model could not match the available data (Haggerty et al., 2001).

used to compute effective permeabilities for the fractures in SP or DP simulations or can be used in DFM simulations without upscaling where flow is simulated explicitly in both, fractures and matrix. This will be discussed in the following sections.

1.1.3.1 *Discrete Fracture Network Model*

The DFN model computes fluid flow in the fractures only, i.e. the surrounding rock matrix is not accounted for explicitly. Only the fractures are discretised usually using a 2D Finite Element (FE) mesh in a 3D space. The DFN model is suitable for modelling fractured reservoirs with high connectivity and very low rock matrix permeability. Another application of DFN models is the geometrical or the flow based upscaling of fracture properties for further reservoir simulation using SP or MC models (Dershowitz et al., 2000).

1.1.3.2 *Discrete Fracture and Matrix Model*

The DFM model computes fluid flow directly and simultaneously in fractures, faults, and rock matrix. Fractures and faults can be discretised as volumetric elements or as lower dimensional elements, i.e. 2D surfaces in 3D geometries or 1D lines in 2D geometries. The matrix is discretised by volumetric finite elements. Therefore, the DFM model is the most accurate approach to represent

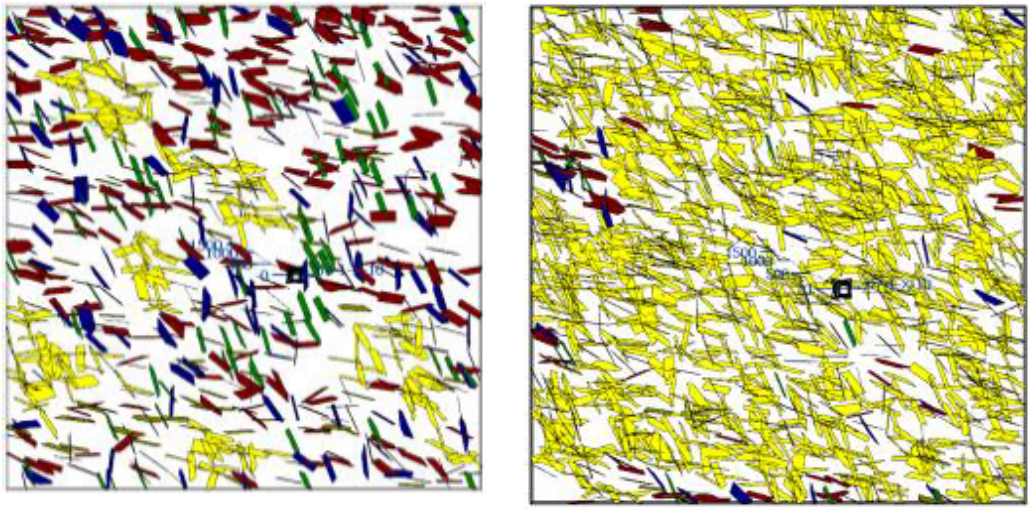

(a) (b)

Figure 1.11: Two Discrete Fracture Network (DFN) representations with different fracture densities: P_{32} = 0.05 (a) and P_{32} = 0.10 (b) (Ahmed Elfeel et al., 2014). Connected fracture clusters are shown in yellow. In the well connected DFN (b) the fluid flow will preferentially occur in the fractures whereas in the DFN with poorly connected clusters of fractures (a) flow has to bypass through the rock matrix.

NFR as an upscaling of the fractures is not required. Fractures may have any orientation and any connectivity in the DFM approach. For example, in contrast to the DFM approach, flow through a NFR containing poorly connected clusters of fractures cannot be simulated with the DFN approach because flow has to bypass through the rock matrix (Fig. 1.11 a). However, fluid flow calculation in the DFM approach typically requires a Finite Element Method (FEM) and/or Finite Volume Method (FVM) (e.g., Durlofsky, 1999; Huber and Helmig, 1999; Monteagudo and Firoozabadi, 2007b; Paluszny et al., 2007; Matthai et al., 2007; Geiger et al., 2009b; Schmid et al., 2013; Reichenberger et al., 2006; Hoteit and Firoozabadi, 2008b,c; Nick and Matthai, 2011). These are more computationally intensive than the simple Finite Difference Method (FDM) (see Chapter 2). Overall, the DFM is computationally the most costly approach, because fractures are resolved in the model which leads to high flow rates in the fractures and small time step in the simulation model (see Chapter 2).

1.1.4 *Discrete Fracture Network Upscaling*

As previously mentioned, the SP and MC models require average upscaled grid properties (i.e. fracture porosity, fracture permeability and shape factor representing the matrix blocks size) for a flow computation. These properties can be obtained by upscaling the DFN. One obtains the upscaled fracture porosity for each grid cell by multiplying the fracture apertures a_f with fracture intensity P_{32} as (Dershowitz et al., 2000)

$$\phi_f = P_{32} a_f. \tag{1.1}$$

There are two types of fracture permeability upscaling methods, the geometrically based upscaling of Oda (Oda, 1985) and the flow-based upscaling method. The latter requires DFN or even DFM flow simulations.

1.1.4.1 *Oda's Upscaling Method*

For a specific simulation grid cell for which an effective fracture permeability should be computed from the DFN model, a fracture tensor F_{ij}, which expresses flow along a fractures unit normal η, can be calculated by summing over the individual fractures f in the grid cell with known area A_f and transmissivity T_f:

$$F_{ij} = \frac{1}{V} \sum_{f=1}^{N} A_f T_f \eta_{if} \eta_{jf}. \tag{1.2}$$

At this, N is the number of fractures, η is the unit normal to a fracture representing its direction and orientation, and V is the total fractures pore volume. Rotating F_{ij} into the planes of the permeability tensor by multiplication with the dirac δ_{ij} allows the approximation of the fracture permeability (Dershowitz et al., 2000):

$$K_{ij} = \frac{1}{12} \left(F_{ff} \delta_{ij} - F_{ij} \right). \tag{1.3}$$

As all parameters for evaluation of equation 1.2 in the DFN are known, Oda's method does not require flow simulations. However, the geometrically based

upscaling method focusses primarily on fracture area and does not take into account the connectivity of the DFN. A poorly connected DFN but with high intensity P_{32} would therefore give high permeability values, even if the fractures do not form a fully percolating cluster (Fig. 1.11).

1.1.4.2 *Flow-Based Upscaling*

For flow-based upscaling of fracture permeabilities from a DFN, boundary conditions (e.g. fixed pressure and no flow boundary) are assigned to the edges of a grid cell in the DFN model. A single-phase flow simulation is carried out to obtain the pressure field and the total throughput q through the fractures in this grid cell. Using Darcy's law and solving for permeability results in the upscaled effective permeability K_{eff} as

$$K_{eff} = \frac{q\mu L}{\Delta p}, \tag{1.4}$$

for each grid cell containing fractures from the DFN. Note that this approach is equally applicable to a DFM model (Matthai and Belayneh, 2004). In this case, the effective permeability will represent the permeability not only of fractures but also of the matrix. Again, in case of a poorly connected fracture network where flow does not percolate through the fractures, the influence of the surrounding matrix is important and the permeability using DFM simulations will give values that can differ substantially from DFN based upscaling (Ahmed Elfeel et al., 2014). In general, computing effective fracture permeabilities from DFNs is associated with a high degree of uncertainty, that translates itself into a history matching workflow (Ahmed Elfeel et al., 2013).

1.1.4.3 *Upscaling Using Multiple Sub-Region Method*

The DFM method can also be employed for upscaling in the MINC approach using the MSR model (e.g., Gong and Durlofsky, 2006; Karimi-Fard et al., 2006; Hui et al., 2007, 2008, 2013). After computing the pressure field in a fine-grid DFM model, one chooses the pressure contour lines to divide the DFM in subregions - into the shells of the MINC model. The transmissivity between two shells is then determined using their local pressure values (Fig. 1.12).

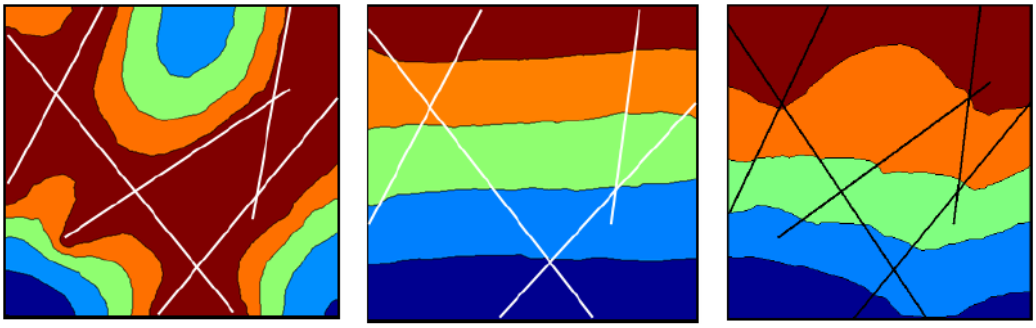

Figure 1.12: Iso-pressure curves at pseudo-steady state for different boundary conditions. Left: Flow driven by fluid injection through fractures only. No fluid flows out of the block through the matrix and gravity effects are neglected. Middle: Flow driven by fluid injection through the matrix on top boundary and fracture injection rate is set to zero. Hence, gravitational effects in absence of fractures are considered here. Right: Total flow into the matrix at the top boundary and fracture injection rate are equal. This model accounts for gravitational effects and flow through fractures as well. Different colours represent different sub-regions which define the coarse grid (shells in MINC model) for the Multiple Sub-Region (MSR) method (Gong and Durlofsky, 2006).

1.1.4.4 *Limitations*

The SP model is typically used in standard Finite Difference (FD) simulators. Since fractures can intersect each other at non-orthogonal angles, the FD grid needs to be deformed which leads to inaccuracies of the flux calculations (Aavatsmark, 2002; Lie et al., 2012). Upscaling of flow functions like relative permeability curves in a SP approach is still an open research area, although Matthai and Nick (2009) presented first attempts to approach this problem, but have not been able to demonstrate a universal solution.

The variety of the MC models gives a good portfolio for flow simulation approaches for NFR. The most advanced methods are the MINC and the MRDP model as they do not use a single average transfer function but rather a set of transfer functions for each grid cell. This allows the reservoir engineer to approximate the multi-rate behaviour observed in the fracture-matrix transfer (MRDP) and to capture the spatial distribution of saturation and pressure within the rock matrix (MINC). However, both methods have in common that they are only applicable if the underlying fracture network is well connected such that the MC model is

valid, i.e. flow is dominated by the fractures.

Finally, the DFM allows the reservoir engineer to represent fractures and other complex geological structures explicitly and is therefore the most accurate approach for NFR modelling. Its disadvantage is the high computational cost which renders full field simulations computationally intractable. Also, the generation of unstructured finite element grids that contain all fractures is extremely challenging and time consuming, which prevents probabilistic and stochastic approaches to quantify uncertainty.

1.2 OBJECTIVES AND STRUCTURE OF THE THESIS

The DFM model can represent all fractures as well as the rock matrix explicitly. The advantage of this model is an improved approximation of the flow behaviour. However, this comes at the cost of extra computational time. Using the DFM approach for intensely fractured reservoirs with well connected fracture networks becomes computationally intractable. But these reservoirs akin to DP systems as flow is dominated by the fractures. DP model enables flow simulations at low computational cost but lacks in accuracy if fractures are poorly connected. In addition, average rock and fluid properties are assigned to each grid cell with a typical size of 100 $m \times 100\ m \times 10\ m$. The DP approach assumes that the entire matrix is uniform in terms of rock properties (e.g., permeability, porosity, wettability) and fluid distribution. In reality, the rock matrix can be highly heterogeneous and fluid saturations vary locally. Another disadvantage of the DP model is that transfer functions require tuning to represent the actual rate of fracture-matrix transfer, if this is at all possible (Abushaikha and Gosselin, 2008).

The aim of this thesis is therefore to improve the simulation of NFR by combining and enhancing the DFM model and the DP model to extend a research-grade reservoir simulator Complex Systems Modelling Platform (CSMP++) (Matthai et al., 2007) which profits from the respective advantages of both, the DFM and the DP approach. Specifically, the objectives of this thesis are

- To improve the performance of the DFM approach by implementing an implicit time stepping scheme for the saturation equation. Implicit schemes allow for larger time steps than explicit time stepping but might differ from the converged solution significantly if the time step is too large. A safeguard algorithm is needed to ensure the global convergence of the implicit solver.

- To improve the DP transfer function which describes the fracture-matrix fluid exchange by implementing a recently developed analytical solution for spontaneous imbibition. This analytical solution leads to a general scaling group for arbitrary rock and fluid properties and can be readily incorporated into a DP model. This improvement should facilitate more accurate predictions of the fracture-matrix transfer because it models spontaneous imbibition using an exact analytical solution. Likewise, gravitational displacement is modelled using an exact analytical solution for this process.

- To implement the so called MRDP model. This model represents sub-grid rock matrix heterogeneities such as the block size, permeability, porosity or other petro-physical properties through a set of transfer functions. Each transfer function models the rate of fluid exchange between fractures and the corresponding sub-domain of the matrix. This facilitates the modelling of the multi-rate behaviour of fluid transfer between the flowing fractures and stagnant matrix inherent to fractured porous media. In the MRDP approach, the aforementioned general scaling group is used.

- To combine the DFM and the MRDP approach in order to obtain a DFM-MRDP simulator which represents large scale fractures and faults explicitly with the DFM approach and models small-scale fractures using the MRDP approach. This simulator will benefit from both approaches: it provides a similar accuracy as the DFM model, requires less computational cost, fracture-matrix transfer is modelled using analytical rather than empirical expressions, and the multi-rate behaviour of fracture-matrix transfer is preserved.

This thesis is divided into three parts: The first part encompasses the first objective - the implementation of the implicit time stepping scheme for the DFM

model. The second part concerns the implementation of the MRDP model and its improvement using analytical solutions to model fracture-matrix transfer. This refers to the second and the third objectives. Finally, the third part is focused on the development of the DFM-MRDP simulator and its applications. This addresses the last objective.

In total this thesis contains 6 chapters.

- Chapter 1 is the current chapter. It provides a brief overview about the modelling of fractured reservoirs and states the objectives of the thesis.
- Chapter 2 introduces the governing two-phase flow equations and their numerical solution using the Implicit Pressure Implicit Saturation (IMPIS) approach on Finite Element - Finite Volume (FEFV) mesh in a DFM model. For the implicit solution of the saturation equation, a Newton iterative method enhanced with a line search backtracking algorithm has been implemented. The accuracy and performance of the IMPIS method is compared to a reference solution obtained by the Implicit Pressure Explicit Saturation (IMPES) method, which is physically stable only for small time steps.
- Chapter 3 introduces the DP approach to simulate NFR, using transfer functions based on analytical solutions for spontaneous imbibition and gravity drainage. The accuracy of these transfer functions is shown by comparison to laboratory experiments. Also, different shape factor formulations and their effect on oil recovery prediction are studied using numerical simulations. This chapter is based on Maier et al. (2013, 2014).
- Chapter 4 extends the DP model from Chapter 3 to the MRDP model. The effect of a heterogeneous rock matrix on oil recovery predictions is studied by varying the matrix permeability and matrix block sizes. The MRDP model results are compared to fine grid simulations. This chapter is based on Maier et al. (2014).
- Chapter 5 presents the development of the DFM-MRDP simulator by combining the models introduced in Chapter 2, Chapter 3 and Chapter 4. The

effect of multi-scale heterogeneity of rock properties is studied by performing simulations on models including large fractures above the simulation grid cell size and small scale fractures below the grid cell size. This chapter is based on Maier et al. (2013) and Maier and Geiger (2013).

- Chapter 6 gives a summary of the key outcomes of the thesis and provides the concluding remarks followed by recommendations for future work.

2

DISCRETE FRACTURE AND MATRIX APPROACH

2.1 INTRODUCTION

The challenge when modelling Naturally Fractured Reservoirs (NFR) is that faults, fracture corridors and fractures are commonly inclined and intersect each other at non-orthogonal angles. Modelling these features with standard corner-point grids is possible but at the expense of inaccurate numerical solutions arising from the two-point flux approximation that is inherent to commercial simulators which are based on finite difference methods (e.g., Aavatsmark, 2002; Lie et al., 2012). A possibility to reduce numerical errors in NFR simulations are multipoint flux approximations (e.g., Wheeler and Yotov, 2006; Sandve et al., 2012). Another possibility is to use unstructured Finite Element (FE) grids, for example a tetrahedral grid (Fig. 2.1) (e.g., Jackson et al., 2013; Crutchley et al., 2013; Milliotte and Matthai, 2014) or a mixture of different FE types (Fig. 2.2) (Paluszny et al., 2007; Matthai et al., 2007) to represent complexly shaped geological structures.

Using unstructured FE grids allows the modelling of NFR using the so-called Discrete Fracture and Matrix (DFM) approach. In the DFM approach, fluid flow is computed directly and simultaneously in fractures, faults, and matrix. Fractures and faults can be discretised as volumetric elements or as lower dimensional elements, i.e. 2D surfaces in 3D geometries or 1D lines in 2D geometries (Fig. 2.2) (Kim and Deo, 2000; Juanes et al., 2002; Paluszny et al., 2007; Matthai et al., 2007).

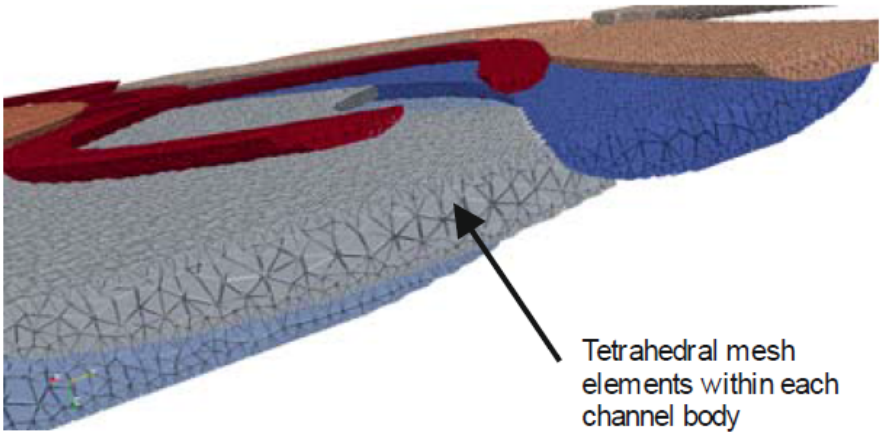

(a)

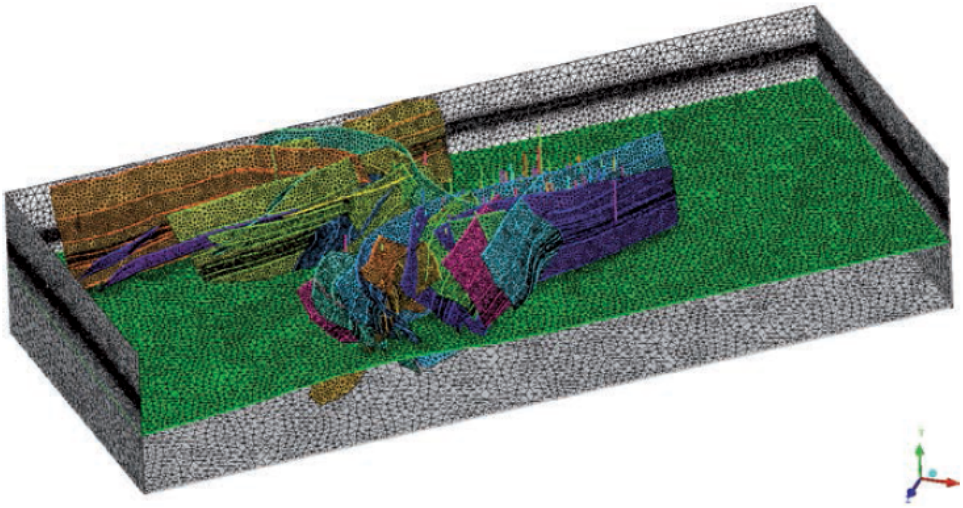

(b)

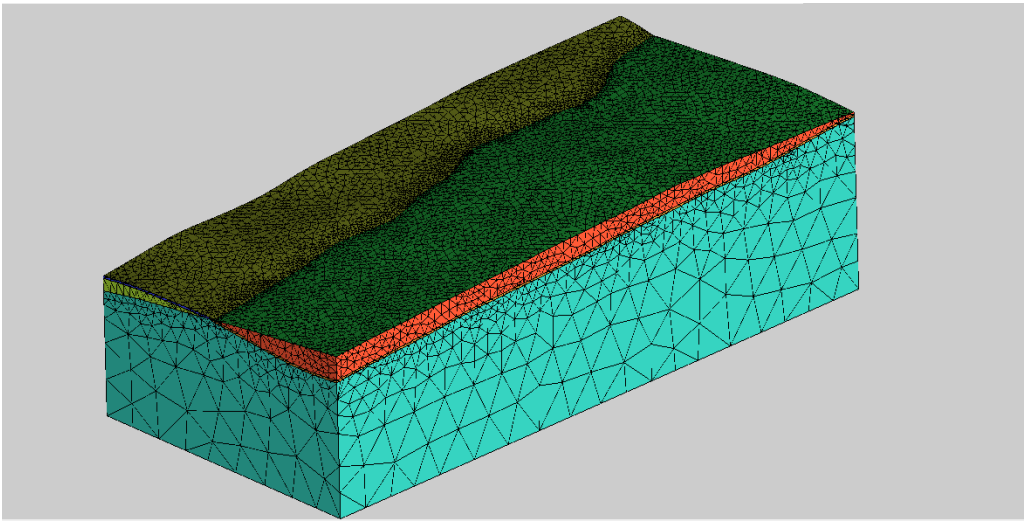

(c)

Figure 2.1: Example of geological structures represented by tetrahedral FE grids: (a) A schematic 3D model of channelised sandbodies in mudstone background (Jackson et al., 2013), (b) a hydrocarbon reservoir located in the Vienna Basin, Austria, containing stratigraphic layers and faults (Milliotte and Matthai, 2014) and (c) a model of the South Hydrate Ridge, a gas bearing sequence of sediments offshore Oregon, USA, with several overlapping horizons obtained from seismic data (Crutchley et al., 2013).

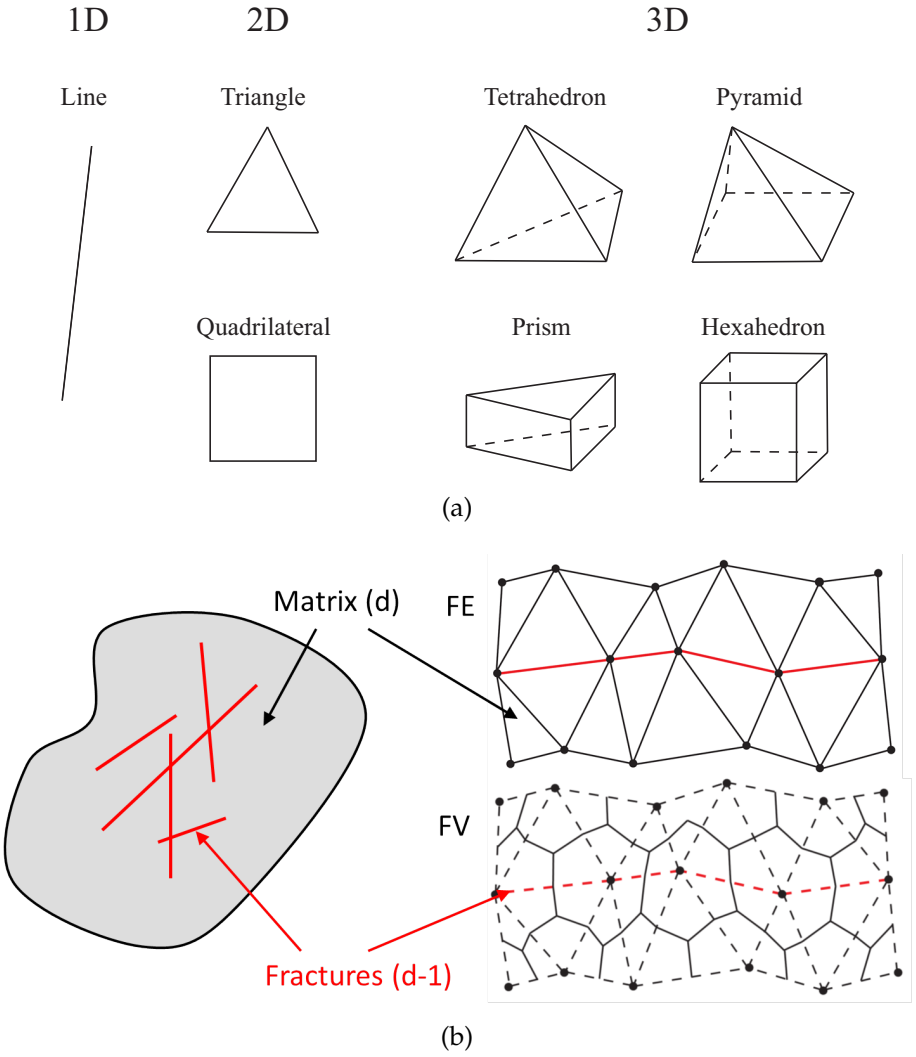

Figure 2.2: Seven different FE types which can be used to describe complex structures in Naturally Fractured Reservoirs (NFR) (a) and a simple 2D geometry and FE mesh with a complementary FV grid (b). 1D line elements are used to represent fractures as d-1 features in a 2D model. 1D line elements are also used to represent wells in general. Triangles and quadrilaterals are used to represent the rock matrix in a 2D model and fractures as d-1 features in a 3D model. In a 3D model, the rock matrix can be represented by tetrahedra, pyramids, prisms and hexahedra.

A number of subsurface flow problems can be simulated using the DFM approach including but not limited to multi-phase multi-component Black-Oil simulations (Geiger et al., 2009b), two-phase flow and simultaneous transport and adsorption of viscosifying species (Schmid et al., 2013), capillary trapping of CO_2 in fractured reservoirs (Annewandter et al., 2013), infiltration of Non-Aqueous Phase Liquids (NAPL) and remediation of groundwater systems (Monteagudo and Firoozabadi, 2004; Graf and Therrien, 2007; Hoteit and Firoozabadi, 2008a), and others.

In this thesis immiscible, incompressible and isothermal two-phase flow in the DFM simulations is considered for simplicity. This can be modelled with following governing equations

$$\phi \frac{\partial \rho_\alpha S_\alpha}{\partial t} + \nabla \cdot (\rho_\alpha v_\alpha) - \rho_\alpha q_\alpha = 0, \tag{2.1}$$

where S is the saturation of the phase $\alpha = wetting, non-wetting$ and requires $S_w + S_{nw} = 1$, ϕ is the porosity and ρ_α the fluid density of phase α. q_α denotes the source and sink term.
Fluid velocities v_α can be obtained from Darcy's law

$$v_\alpha = -\lambda_\alpha K \left(\nabla p_\alpha - \rho_\alpha g\right), \tag{2.2}$$

using the phase mobilities $\lambda_\alpha = k_{r\alpha}/\mu_\alpha$, i.e.,the fraction of relative permeabilities $k_{r\alpha}$ and fluid viscosities μ_α and the permeability K. p_α is the fluid pressure and g is the gravitational acceleration.

After defining capillary pressure as $P_c = p_{nw} - p_w$ and summing up Eqs. 2.1 and 2.2, the total velocity $v_t = v_w + v_{nw}$ can be obtained as

$$v_t = -K \left(\lambda_t \nabla p_w + \lambda_{nw} \nabla P_c - \lambda_w \rho_w g - \lambda_{nw} \rho_{nw} g\right), \tag{2.3}$$

where $\lambda_t = (\lambda_w + \lambda_{nw})$ is the total mobility. Eq.2.3 is referred to as the pressure equation.

The velocity for the non-wetting phase can now be rewritten in terms of the total velocity as

$$v_{nw} = f_{nw} v_t - \bar{\lambda} K \left(\nabla Pc + \rho_w g - \rho_{nw} g \right). \tag{2.4}$$

Here, $f_{nw} = \lambda_{nw}/\lambda_t$ is the fractional flow for the non-wetting phase and

$$\bar{\lambda} = \frac{\lambda_w \lambda_o}{\lambda_t} \tag{2.5}$$

is the fraction of the product of phase mobilities with the total mobility.

Since fluids are assumed to be incompressible and

$$\frac{\partial S_{nw}}{\partial t} = -\frac{\partial S_w}{\partial t}, \tag{2.6}$$

Eq. 2.1 for the non-wetting phase can be rewritten as

$$\phi \frac{\partial S_w}{\partial t} - \nabla \cdot v_{nw} + q_{nw} = 0. \tag{2.7}$$

Inserting Eq. 2.4 into Eq. 2.7 yields the so-called saturation equation in fractional flow form

$$\phi \frac{\partial S_w}{\partial t} + \nabla \cdot \left(f_w v_t + \bar{\lambda} \left(\nabla P_c - \Delta \rho g \right) \right) - q_w = 0, \tag{2.8}$$

with $\Delta \rho = \rho_{nw} - \rho_w$.

The two-phase equations are of a mixed hyperbolic-parabolic type (Huber and Helmig, 1999). The pressure equation (Eq. 2.3) is an elliptic Partial Differential Equation (PDE) and is well suited to be solved by a Finite Element Method (FEM). However, the saturation equation (Eq. 2.8) can change its type from parabolic to hyperbolic if the capillary pressure gradient becomes small $\frac{dP_c}{dS_w} \cong 0$ (Helmig, 1997). In hyperbolic PDEs, the information (e.g., the saturation front) travels with a finite speed. For parabolic PDEs, however, a small local change of the initial value can instantaneously affect the full computational domain. Hence, the two processes described by Eqs. 2.3 and 2.8 operate on two different time scales and decoupling of the system is justified. To assure mass conservation, the Fi-

nite Volume Method (FVM) should be used for solving equation 2.8. This results in a Finite Element - Finite Volume (FEFV) method. Many FEFV schemes have been developed in the DFM context in recent years (e.g., Durlofsky, 1999; Huber and Helmig, 1999; Monteagudo and Firoozabadi, 2007b; Paluszny et al., 2007; Matthai et al., 2007; Geiger et al., 2009b; Schmid et al., 2013; Reichenberger et al., 2006; Hoteit and Firoozabadi, 2008b,c; Nick and Matthai, 2011). Their main differences lie in the calculation of fluxes. For example, Durlofsky (1999) and Huber and Helmig (1999) use a Mixed FE approach where the velocity and pressure are computed simultaneously, while Matthai et al. (2007), Geiger et al. (2009b) or Schmid et al. (2013) use a classical Galerkin FE method to compute the pressure field. The velocity field is then determined via a post processing step. Other differences are the use of higher order flux approximations (e.g., Geiger et al., 2009b; Schmid et al., 2013) or the calculation of capillary forces at the fracture - matrix interface (e.g., Niessner et al., 2005; Reichenberger et al., 2006; Monteagudo and Firoozabadi, 2007b; Hoteit and Firoozabadi, 2008b,c; Nick and Matthai, 2011).

One commonality of all methods is that they are typically based on a so-called Implicit Pressure Explicit Saturation (IMPES) method. In the IMPES approach, the pressure equation is solved implicitly in time followed by the explicit solution in time of the advection (i.e. saturation) equation (Chen, 2007). The implicit solution of the pressure equation allows for bigger time steps Δt_{PresEq}, which avoids the time step restrictions due to its parabolic nature. However, the time step for the explicit solution of the saturation equation Δt_{SatEq} is restricted by the so-called Courant-Friedrich-Lewy (CFL) condition. To ensure the stability of an explicit method, the following condition must hold

$$\Delta t_{max} = \left(\frac{L_{FV}}{v_{t,max}} \right), \ \forall FV, \tag{2.9}$$

where L_{FV} is the length of a finite volume sector in the direction of the maximum pore velocity in the finite volume $v_{t,max}$. The CFL condition ensures that the saturation front is not transversing more than one finite volume within one time step. Due to the non-linear flux function of the multi-phase flow (Fig. 2.4d) the time step must be further constrained to guarantee the stability of the explicit solution after each velocity values update, i.e. after each solution of the pressure

equation. The discretization time step for the saturation equation is therefore chosen as

$$\Delta t_{SatEq} = c\Delta t_{max},\ c \in (0,1). \tag{2.10}$$

In case the resulting time step Δt_{SatEq} is larger than the time step used for the implicit solution of the pressure equation Δt_{PresEq}, it is set to $\Delta t_{SatEq} = \Delta t_{PresEq}$. If $\Delta t_{SatEq} < \Delta t_{PresEq}$, the saturation equation is solved repeatedly n times with

$$n = \frac{\Delta t_{PresEq}}{\Delta t_{SatEq}}. \tag{2.11}$$

This means that for one pressure equation computation there will be several forward step computations of the saturation equation with smaller time steps. The mass conservation might be violated if the time steps Δt_{PresEq} and Δt_{SatEq} differ significantly, as the pressure field is calculated using the saturation values from the previous time step and vice versa. Doster et al. (2013) proposed a relaxed volume approach that counteracts the violation of mass conservation and reduces the error due to operator splitting by adding an additional source term to the pressure equation based on the volume mismatch after the transport calculation. However, the time step for the pressure equation can still not be chosen arbitrary large due to the physical coupling of the non-linear system (Eq. 2.1) and no estimate of the possible time step is available yet. Thus, the time step for the pressure equation strongly depends on the specific problem and has to be evaluated empirically. This is a general problem for all operator splitting techniques.

The IMPES approach is problematic for NFR, where the velocity might vary locally and globally by many orders of magnitude. Typically, the largest velocities are found in the fractures where the FVs are smallest, which leads to prohibitively small time steps Δt_{SatEq} and high computational costs (Fig.2.3). One possibility to solve this problem is to divide the computational domain into sub-domains and use parallel computing such that flow and transport are calculated separately in each sub-domain of the NFR (Geiger et al., 2009a).

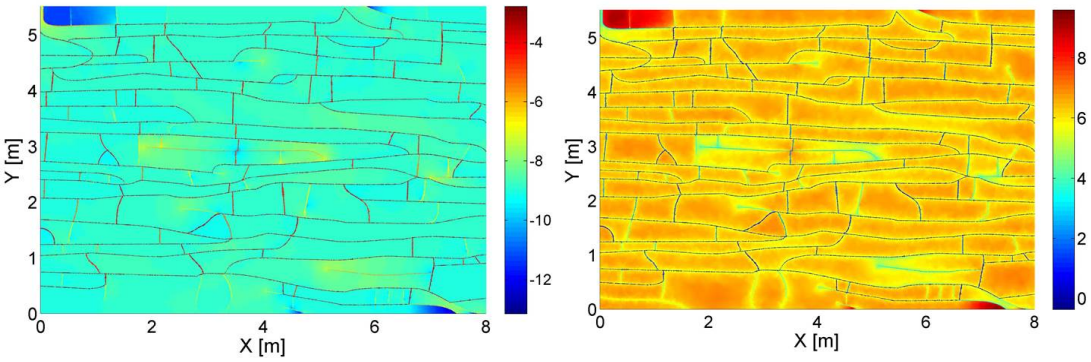

(a) (b)

Figure 2.3: Magnitude of the velocity field in $log_{10}\ m^2/s$ (a) and the corresponding CFL time step Δt_{max} (Eq. 2.9) distribution in $log_{10}\ s$ (b) for a simulation of a fractured limestone outcrop in Bristol Channel, UK (Belayneh, 2004; Geiger et al., 2009a). Note that the fractures can be easily identified as the area with the highest velocity and smallest time step. The matrix permeability is 0.1 Darcy whereas the fractures have a permeability of 1000 Darcy. The velocity values as well as the CFL time step vary over six orders of magnitude. The smallest permissible time step Δt_{max} given by the CFL condition is located in the finite elements representing the fractures because of the small FEs and high velocity values.

Another solution is to use implicit methods that are not subject to the CFL condition and allow for larger time steps. Implicit methods are unconditionally stable for convex (shock), concave (rarefaction wave) or linear (contact discontinuity) flux functions. However, most multi-phase flow problems in reservoir simulation are described by an S-shaped flux function (Fig. 2.4):

$$v = F(S)\,, \quad S = F(v)\,. \tag{2.12}$$

Here, the velocity field is a non-linear function of the saturation and the saturation is a non-linear function of the velocity field. This coupling requires non-linear iterations. A classical non-linear iterative method is the Newton method. However, it does not converge for large time steps if the flux function is S-shaped (Aziz and Settari, 1979; Jenny et al., 2009; Younis et al., 2010). In this case a combination of the Newton method with global convergence strategies is necessary.

In this chapter, a DFM approach is presented that has been successfully implemented and was modified in the Complex Systems Modelling Platform (CSMP++) (Matthai et al., 2007). I use an Implicit Pressure Implicit Saturation (IMPIS) scheme (Chen, 2007) for solving the decoupled two-phase equations, i.e. the pressure

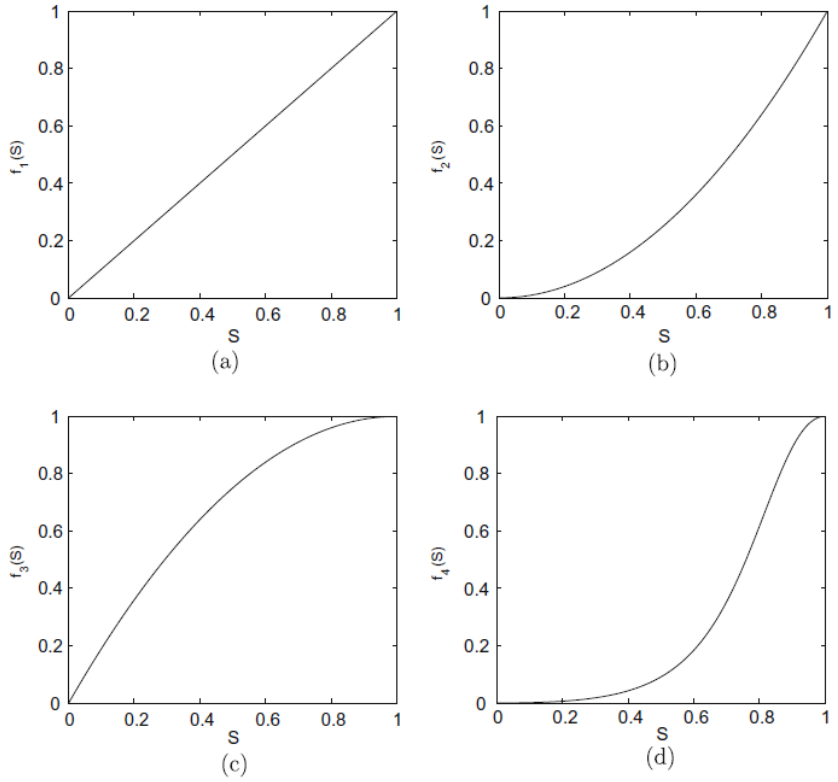

Figure 2.4: Linear (a), convex (b), concave (c) and S-shaped (d) flux functions representing shocks, rarefaction waves, contact discontinuities and multi-phase flow, respectively (Jenny et al., 2009).

equation (Eq. 2.3) as well as the saturation equation (Eq. 2.8) are solved implicitly in time. For the former, the FEM is used. For the latter, the FVM is applied together with a Newton iterative solver that was enhanced with a line search backtracking algorithm.

Afterwards the implicit solver for the saturation equation is benchmarked solving a standard Buckley-Leverett problem. Then a two-phase flow simulation on a simple quarter five spot model and two simulations on a complex fracture geometry are presented in order to compare the IMPES and IMPIS approaches, both in terms of accuracy and speed.

2.2 NUMERICAL FORMULATION

The computational domain Ω comprising the NFR is divided into two contiguous sub-domains, the matrix domain Ω_m and the fracture domain Ω_f. Ω_m is discretised in space using tetrahedral elements in 3D and triangular elements for 2D

models. High aspect ratio structures like fractures and geological boundaries can be discretised by d-1 elements, i.e. as 2D planes in 3D and 1D line elements in 2D models. Wells are always modelled as 1D lines. If the fractures are represented as d-1 elements, the geological thickness, i.e. the fracture aperture a_f, needs to be accounted for when integrating the pressure and saturation equations:

$$\int_\Omega X d\Omega = \int_{\Omega_m} X d\Omega_m + a_f \int_{\Omega_f} X d\Omega_f, \tag{2.13}$$

where X is the unknown variable p_α or S_α.

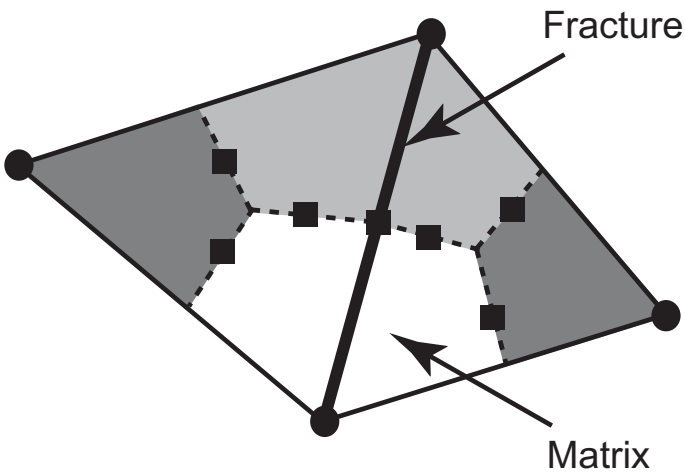

Figure 2.5: Two 2D finite elements (solid lines) with corresponding finite volume boundaries (dashed lines). The circles are nodes of the finite elements, the squares are representing the integration points at finite volume facets across which the flux is calculated between two neighbouring FVs. The white and grey areas represent the sectors of the finite volumes, i.e. all sectors around one node combine to form one finite volume (Fig. 2.2). The bold line in the centre represents the 1D fracture (Geiger et al., 2009b).

The discretisation of Ω comprises both, the finite element grid and the complementary finite volume grid that is calculated through a barycentric tessellation (Paluszny et al., 2007). The barycentre of each element is connected with the midpoints of its edges and divides the element into sectors associated with the neighbouring nodes (Fig. 2.5). All sectors around one node therefore combine to form a finite volume. The permeability and porosity values (K, ϕ) are assigned to the elements and are element-wise constant. Other material properties such as (ρ, μ) and also the state variables (p, S) are assigned to the FV and constant across each FV. They can be interpolated to the integration points (Fig. 2.5) to approximate k_r and P_c when calculating the flux between adjacent FVs. The generic

algorithm to compute equation 2.1 using the FEFV method with implicit time stepping and time step Δt is:

- Obtain pressure values $p_w^{t+\Delta t}$ using fluid saturations S_α^t
- Compute fluid phase $v_\alpha^{t+\Delta t}$ and total velocity $v_t^{t+\Delta t}$ using $p^{t+\Delta t}$ and S^t
- Obtain saturation values $S^{t+\Delta t}$ using $v_t^{t+\Delta t}$

Each step is discussed in detail below.

2.2.1 *Solving the Pressure Equation*

The elliptic pressure equation (Eq. 2.3) is solved using a standard Galerkin FEM. The finite elements span a finite element space Ψ in Ω containing fractures and matrix (Eq. 2.13) of continuous linear polynomial functions $\{\psi_i\}_{i=1}^m \subset \Psi$ with the basis functions

$$\psi_i\left(x_j\right) = \begin{cases} 1, & i = j \\ 0, & otherwise \end{cases}. \tag{2.14}$$

where $x_j \in N = \{x_i\}_{i=1}^m$ is the coordinate vector of Lagrange point j. The pressure equation can now be written in its weak form after applying the Galerkin projection onto Ψ as

$$\begin{aligned} \int_\Omega \lambda_t K \nabla p_w \nabla \psi_i dx = &- \int_\Omega \lambda_n K \nabla P_c \nabla \psi_i dx \\ &- \int_\Omega \nabla \cdot \left(\left(\rho_n \lambda_n + \rho_w \lambda_w\right) g\right) \psi_i dx \\ &+ \int_\Omega q \psi_i dx. \qquad\qquad i = 1 \ldots m \end{aligned} \tag{2.15}$$

The pressure at point x can then be interpolated with the basis functions as

$$p_w\left(x\right) = \Sigma_{i=1}^m p_w\left(x_i\right) \psi_i\left(x\right). \tag{2.16}$$

The resulting linear system of equation $\mathbf{Ap} = \mathbf{b}$ with $A \in \mathbb{R}^{m \times m}$ and $b \in \mathbb{R}^m$

$$\begin{aligned} \mathbf{p\_i} &= p_w(x_i), \\ \mathbf{A\_ij} &= \int \lambda_t \nabla \psi_i K \nabla \psi_j dx, \\ \mathbf{b\_i} &= -\int \lambda_n K \nabla P_c \nabla \psi_i dx - \int \nabla \cdot \left(\left(\rho_w \lambda_w + \rho_n \lambda_n \right) g \right) \psi_i dx \\ &\quad + \int q \psi_i dx. \end{aligned} \tag{2.17}$$

can now be solved using an algebraic multi-grid solver (Stueben et al., 2007). Algebraic multi-grid solvers are computationally efficient because the required Central Processing Unit (CPU) time scales linearly with the size of $\mathbf{A}$.

2.2.2 *Computing the Velocity Field*

Once the pressure field was computed, the velocity field can be calculated for each finite element in a post processing step using Darcy's law

$$v_\alpha = -K \lambda_\alpha \left(\nabla p_\alpha - \rho_\alpha g \right). \tag{2.18}$$

For each finite element velocity is obtained by element-wise differentiation of the pressure field

$$v_{\alpha,j} = \sum_{i,j}^{n,d} -K_{ij} \lambda_\alpha \left(p_{\alpha,i} \nabla \psi_{ij} - \rho_\alpha g \right), \tag{2.19}$$

where i and j are are indices over the n nodes of a FE and d is its dimension. $\nabla \psi$ is a $d \times n$ matrix holding the derivatives of ψ_i. The velocity values are therefore element-wise constant but locally continuous across two adjacent finite volume boundaries.

2.2.3 *Solving the Saturation Equation*

This velocity field, which is continuous across two FVs, enables the solution of the saturation equation (Eq. 2.8) using the mass conservative FVM after applying the Gaussian divergence theorem

$$\int_{FV} \nabla \cdot X dx = \int_{\Gamma_{FV}} X\eta \; d\Gamma, \tag{2.20}$$

where X is the saturation equation (Eq.2.8) and η the outward pointing unit normal. Note that the saturation equation (Eq. 2.8) can be split further into an advection and diffusion equation using Strang operator splitting (Strang, 1968) where the former only contains the viscous and gravitational forces and the latter only the capillary forces. This splitting facilitates a numerical solution using FVM for the advection part and FEM, in analogy to section 2.2.1, for the diffusive part (e.g., Geiger et al., 2004, 2006; Schmid et al., 2013; Annewandter et al., 2013).

Equation (Eq.2.20) is discretised implicitly in time using the iterative Newton method for each FV as

$$F'\left(S_\alpha^{t+\Delta t}\right) \Delta S_{NW} = -F\left(S_\alpha^{t+\Delta t}\right), \tag{2.21}$$

on the residual function

$$\begin{aligned} F\left(S_\alpha^{t+\Delta t}\right) = &\int_{FV} \phi \frac{\partial S_\alpha}{\partial t} \; dFV \\ &+ \int_{\Gamma_{FV}} f_w\left(S_\alpha^{t+\Delta t}\right) v_t \eta - \bar{\lambda}\left(S_\alpha^{t+\Delta t}\right)\left(\nabla P_c\left(S_\alpha^{t+\Delta t}\right) + \Delta\rho g\right)\eta \; d\Gamma \\ &- q. \end{aligned} \tag{2.22}$$

The integral over the finite volume for the first term can be approximated as

$$\int_{FV} \phi \frac{\partial S_\alpha}{\partial t} dFV \approx \left(S_\alpha^{t+\Delta t} - S_\alpha^t\right) \frac{\phi V}{\Delta t}. \tag{2.23}$$

Here ϕV is the pore volume of the finite volume.

$$F'\left(S_\alpha^{t+\Delta t}\right) = \frac{dF\left(S_\alpha^{t+\Delta t}\right)}{dS_\alpha} \tag{2.24}$$

is the corresponding Jacobian that needs to be evaluated in each FV. For the computation of the flux terms across the FV boundary Γ_{FV}, upstream and downstream nodes are identified at each finite volume facet (Fig. 2.5) depending on the velocity field orientation ($v_t\eta > 0$ or $v_t\eta < 0$). Fractional flow f_w, mobilities λ_α and capillary pressure P_c are then evaluated using the properties $k_{r\alpha}$, μ_α and the saturation values S_α at the upstream node. In case of capillary dominated or counter-current flow one should consider to take into account the direction of phase velocities (Doster et al., 2013). This results in a method that is first order accurate in space and hence leads to dispersed saturation fronts. One can obtain a second order method if the properties are interpolated directly to the finite volume facets. However, it might result in non-physical values if the gradients between two finite volumes are steep. Application of a so-called flux limiter scheme would then be necessary (Matthai et al., 2007).

Assembling equation 2.21 for each FV leads again to a vector matrix system $\mathbf{As} = \mathbf{b}$ that can be solved with algebraic multi-grid solver (Stueben et al., 2007). The saturation values at the next time step for each FV can be computed as

$$S_\alpha^{t+\Delta t} = S_\alpha^t + \Delta S_{NW}. \tag{2.25}$$

The standard Newton algorithm strongly depends on the initial guess for $S_\alpha^{t+\Delta t}$ and can deploy its locally quadratic convergence only if a good solution approximation is available. Especially in NFR, such an estimate is hard to obtain and a combination with global convergence strategies is necessary (Monteagudo and Firoozabadi, 2007a).

Such a strategy includes the line search backtracking algorithm (Eq. 2.27) (Nocedal and Wright, 1999), which is performed during each Newton iteration step. It chooses a smaller step towards the solution until the convergence criteria is satisfied.

$$S_{init}^{t+\Delta t,n+1} = S^{t+\Delta t,n} + \Delta S_{NW} 2^{-m}, \tag{2.26}$$

where n refers to the n-th Newton iteration and m to the m-th line search iteration starting with $m = 0$. $S_{init}^{t+\Delta t,n+1}$ is the initial guess for the next Newton step. For the first calculation of the iteration, the initial guess is the initial saturation distribution in the reservoir. Because of the non-linearity of the saturation equation and/or the S-shaped flux function, reducing the saturation step can sometimes lead to higher residual after a line search step. In this case, a safeguard step is introduced such that the saturation from the previous line search step is used as the initial guess for the next Newton iteration as it was closer to the solution:

$$S_{init}^{t+\Delta t,n+1} = S^{t+\Delta t,n} + \Delta S_{NW} 2^{-(m-1)}, \tag{2.27}$$

if

$$||F\left(S^{t+\Delta t,n} + \Delta S_{NW} 2^{-m}\right)||_2 > ||F\left(S^{t+\Delta t,n} + \Delta S_{NW} 2^{-(m-1)}\right)||_2, \tag{2.28}$$

for $m > 1$. If the initial guess is close to the solution, the convergence criteria is already reached for $m = 0$, which would be a standard Newton step. In summary, the combination of the Newton algorithm and the line search backtracking method benefits from both strategies and a good convergence can be expected with $n_{max} = 5$ and $m_{max} = 5$ (see A.1.1).

The overall algorithm that combines the FEM and FVM results in a standard IMPIS method for unstructured grids. It is independent from the CFL condition, but it is still limited in the choice of the time-step size due to the strong physical coupling of the pressure (Eq. 2.3) and the saturation equation (Eq. 2.8). However, in comparison to an IMPES method, an acceleration of the two-phase flow simulation is achieved, as shown in the following section.

2.3 SIMULATION RESULTS

First the implicit solver of the saturation equation described above is benchmarked using the analytical solution of the Buckley-Leverett problem in one-dimensional space (Buckley and Leverett, 1942). Afterwards, one two-phase flow

simulation on a 2D quarter five spot model is presented with an impermeable barrier in the model centre and two two-phase flow simulations on a highly fractured 2D geometry where the fluids have varying viscosity ratios. The fractured geometry was mapped in a fractured limestone outcrop in the Bristol Channel, UK (Belayneh, 2004). The fractures are highly conductive such that the velocity in the matrix and fractures differs significantly, causing small time steps for the IMPES method due to the CFL condition (Fig. 2.3). The two phases are assumed to be oil and water. For simplicity, the gravitational forces were neglected with $\rho_o = \rho_w = 1000\ kg/m^3$. Neglecting gravitational forces at the Bristol Channel geometry is reasonable because the fractures are bed-bound and the model geometry is plane (map view). Likewise capillary forces are neglected for simplicity as they could always be modelled using an additional FEM step as discussed before (see remark in Section 2.2.3).

These simulations enable to compare the performance of the IMPES and IMPIS methods in terms of accuracy and speed. Both methods use volumetric FE grids and the FEFV approach is applied as discussed previously. For better comparison of the performance of the IMPES and the IMPIS method, the pressure equation is solved only once at the beginning of each simulation. The resulting velocity field remains then constant during the whole simulation. Although the pressure field would differ during a reservoir simulation, this approach was chosen to study the error of the implicit solver for the saturation equation avoiding interference of the error due to operator splitting.

2.3.1 *Buckley-Leverett Problem*

The Buckley-Leverett problem describes incompressible two-phase flow in porous media where the capillary and gravitational forces are neglected. This process can be modelled as

$$\phi \frac{\partial S_w}{\partial t} + v \frac{\partial f(S_w)}{\partial x} = 0. \tag{2.29}$$

The advantage of the Buckley-Leverett problem is that it has a simple analytical solution using the Welge tangent method (Welge, 1952) and hence provides a well-known problem for validating numerical methods. To compare the accuracy of the implicit solution of the saturation equation described above to the explicit solution, a one-dimensional homogeneous domain is considered with rock and fluid properties listed in Table 2.1. The domain is initially filled by 100 % oil with a viscosity of $\mu_o = 5.0 \times 10^{-3}\ Pa \cdot s$. The invading fluid from the left boundary is considered to be water with a viscosity of $\mu_w = 1.0 \times 10^{-3}\ Pa \cdot s$. The standard Brooks-Corey relative permeabilities curves were used with the same Brooks Corey exponent for both fluid phases and a capillary entry pressure that is almost zero. The spatial discretization of the domain is $\Delta x = 0.5\ m$.

low velocity case			
$L\ [m]$	100	$\phi\ [/]$	0.25
$K\ [mD]$	10.0	$\mu_w\ [Pa \cdot s]$	1.0×10^{-3}
$\Delta p\ [Pa]$	2.0×10^{7}	$\mu_o\ [Pa \cdot s]$	5.0×10^{-3}
$Brooks - Corey\ exponent\ [/]$	2.0	$S_{wmc}\ [/]$	0.0
$Entry\ pressure\ [Pa]$	1.0×10^{-20}	$S_{or}\ [/]$	0.0
high velocity case			
$L\ [m]$	1000	$\phi\ [/]$	0.25
$K\ [mD]$	10000.0	$\mu_w\ [Pa \cdot s]$	1.0×10^{-3}
$\Delta p\ [Pa]$	2.0×10^{7}	$\mu_o\ [Pa \cdot s]$	5.0×10^{-3}
$Brooks - Corey\ exponent\ [/]$	2.0	$S_{wmc}\ [/]$	0.0
$Entry\ pressure\ [Pa]$	1.0×10^{-20}	$S_{or}\ [/]$	0.0

Table 2.1: Fluid and rock properties for the Buckley-Leverett problem simulations.

Two cases are studied. The first case considers a domain with a length of $L = 100\ m$ and permeability of $K = 10\ mD$. This results in low pore velocity of $v = 1.6 \times 10^{-4}\ m/s$ which is held constant during the simulation. The CFL time step for saturation equation is then $\Delta t_{max} = 55803\ sec$. Fig. 2.6 shows the analytical solution of the water front propagation after 100 days compared to simulation results obtained with explicit time stepping (a) and implicit time stepping (b) for three different CFL time step multipliers. Here, CFL 1 corresponds to the original time step $\Delta t_{SatEq} = \Delta t_{max}$ and CFL 50 corresponds to $\Delta t_{SatEq} = 50\Delta t_{max}$. As expected, the first order explicit solution matches the analytical solution well when the time step is smaller or equal to the CFL time step, but it does not give

a reasonable solution if $\Delta t_{SatEq} > \Delta t_{max}$ because the CFL condition is violated here. On the other hand, the implicit solver converges to the analytical solution for time steps larger than the CFL time step, although the resulting water front is dispersed. The dispersion of the water front increases with increasing time step due to numerical dispersion, which is characteristic to implicit methods.

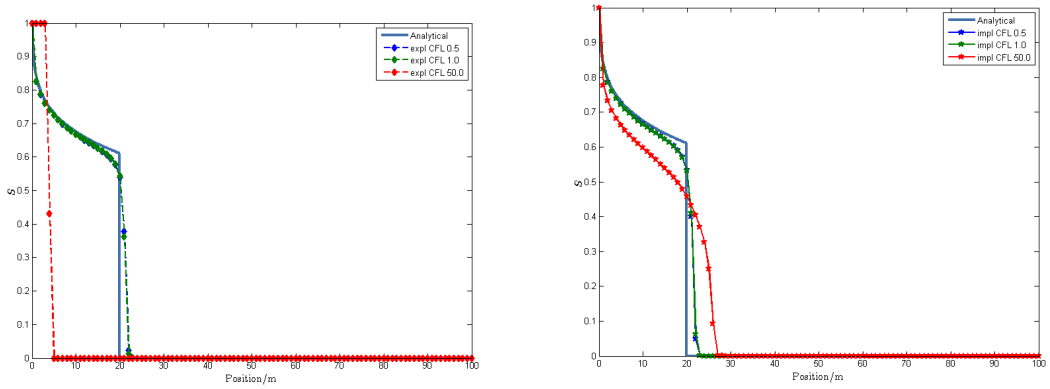

(a) (b)

Figure 2.6: Comparison of saturation profiles for the low velocity case for a model time of 100 days. The analytical solution is compared to saturation profiles obtained by the explicit method (a) and the implicit method (b) using different CFL time step multipliers. CFL 1.0 corresponds to the time step which satisfies the CFL condition, where CFL 0.5 is half of this time step. CFL 50 corresponds to an overstepping factor of 50. The explicit solution matches the analytical solution well for CFL multiplier ≤ 1, but it does not give a reasonable saturation profile for higher multipliers. The implicit solution converges for higher CFL multipliers, although it yields diffusive water fronts with increasing time step.

The L_2 relative error

$$\left\| \frac{S_{ana}(x) - S_{num}(x)}{S_{num}(x)} \right\|_2, x \in [0, L] \tag{2.30}$$

for different CFL time step multipliers where a convergence to the analytical solution is achieved is shown in Fig. 2.7. The implicit solver converges for all CFL time step multipliers ≤ 60, where the L_2 relative error increases with increasing time step due to the numerical dispersion and reaches 50% for CFL multiplier = 50. The computational time for all simulations using an explicit or implicit method was 1 *sec*. Therefore, for a low velocity case, the explicit solver would have the advantage of lower relative error compared to the implicit solver using

small time steps.

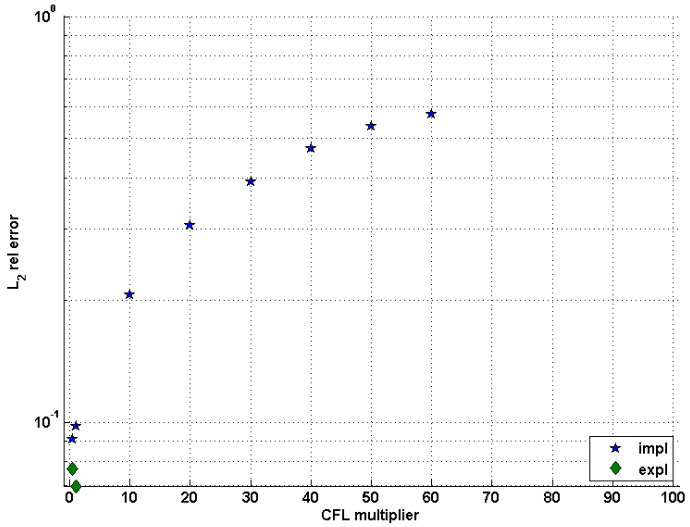

Figure 2.7: Relative error of the explicit and the implicit method for different CFL multipliers for the low velocity case in log_{10} scale. The explicit methods yields the smallest error, but is constrained by the CFL condition. The implicit solver converges to the analytical solution as the overstepping multipliers decreases and the error increases with increasing time step due to numerical dispersion.

The domain for the second case is $L = 1000\ m$ long and has a 1000 times higher permeability of $K = 10\ D$, which yields higher fluid velocity of $v = 1.6 \times 10^{-4}\ m/s$. The CFL time step for saturation equation decreases to $\Delta t_{max} = 558\ sec$. Fig. 2.8 shows the water saturation profile after 25 days obtained with the analytical solution of the Buckley-Leverett problem and the numerical solution using the explicit method (a) and the implicit method (b). Here again, the explicit solver matches the analytical solution, but yields a reasonable saturation profile only for CFL multiplier ≤ 1. In contrast to the low velocity case, the numerical dispersion using the implicit method is less prominent for all CFL multipliers and its increase with increasing time step is significantly lower.

The lower numerical dispersion results in a relative error below 12% for all CFL multipliers, where a convergence of the implicit solver to the analytical solution is achieved (Fig. 2.9). The numerical error is reduced to 10% for CFL multiplier of 50, compared to 50% for the low velocity case. A slight improvement in the CPU time with higher CFL multipliers, i.e. larger simulation time steps, can be

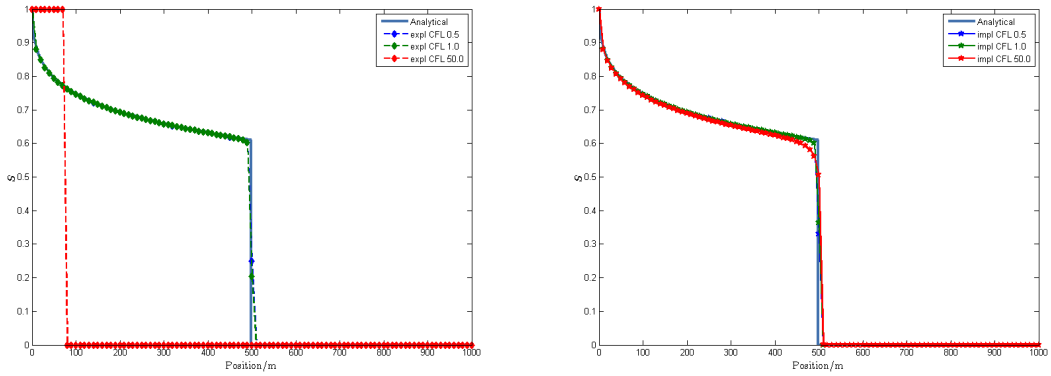

(a) (b)

Figure 2.8: Water saturation profiles for the high velocity case for a model time of 25 days. The analytical solution is compared to saturation profiles obtained by the explicit method (a) and the implicit method (b) using different CFL time step multipliers. CFL 1.0 corresponds to the time step which satisfies the CFL condition, where CFL 0.5 is half of this time step. CFL 50 corresponds to an overstepping factor of 50. Compared to the low velocity case, the numerical dispersion is significantly lower for both methods, the explicit and the implicit method for solving the saturation equation.

observed (see Table 2.2) but this improvement comes at the expense of numerical accuracy. The numerical error resulting from the IMPES method is again notably lower.

CFL multiplier	0.5	1	10	20	30	40	50	60
explicit	6 *sec*	3 *sec*	-	-	-	-	-	-
implicit	18 *sec*	10 *sec*	3 *sec*	3 *sec*	2 *sec*	2 *sec*	2 *sec*	2 *sec*

Table 2.2: CPU time for the high velocity case simulations for a model time of 25 days. The IMPES method is faster than the IMPIS method for CFL multiplier ≤ 1, but CPU time for the IMPIS decreases for larger time steps (CFL multiplier ≥ 30) at expense of accuracy (see Fig. 2.9).

The simple Buckley-Leverett problem shows that the IMPIS method has the advantage of slightly faster solution for the saturation equation although the numerical error is higher than the one obtained by the IMPES method. Nevertheless, the numerical error decreases with higher fluid velocities and smaller CFL time steps. In case of flow simulations in NFR, the velocities will vary greatly due to highly heterogeneous permeability field. In the fractures, the combination of high fluid velocities and small cells will dominate the determination of the CFL time step, which will cause the IMPES method to become inefficient. In contrast,

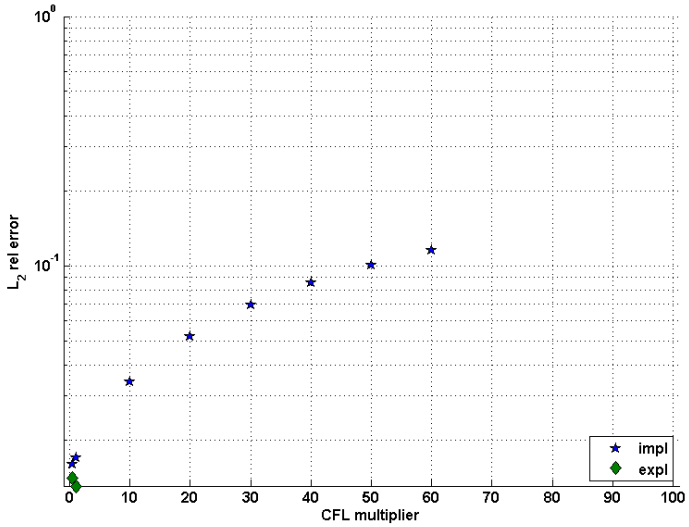

Figure 2.9: Relative error of the explicit and the implicit method for different CFL multipliers for the high velocity case in log_{10} scale. The relative error is half an order of magnitude smaller compared to the low velocity case. Here, the relative error for the implicit method increases at a slower rate with increasing time steps. The explicit method yields the lowest error when the CFL condition is satisfied, i.e. for a CFL timestep multiplier ≤ 1.

the IMPIS method benefits from the ability of overstepping the CFL condition and hence is computationally more efficient. As the CFL time step is controlled by the region with high fluid velocities, the overstepping the CFL condition in the regions where fluid velocities are low, e.g. the rock matrix, will be small if present at all. For example, the overstepping in the high velocity case above using a CFL multiplier of 50 leads to a global time step of $\Delta t = 27900$ *sec*, which corresponds to a CFL multiplier of 0.5 in the low velocity case.

2.3.2 *Quarter Five Spot Model*

The quarter five spot model has dimensions of 200 $m \times 80$ m and is composed of 2352 finite elements and 1256 nodes, i.e. finite volumes (Fig. 2.10). The impermeable barrier in the centre has a low permeability of 1.0×10^{-3} mD whereas the surrounding matrix has a permeability of $K_m = 1$ D. The model was initially saturated with 90% oil and 10% water. The standard Brooks Corey model was used for computing relative permeabilities curves. The two fluids have the same viscosity $\mu_w = \mu_o = 1.0 \times 10^{-3}$ $Pa \cdot s$, hence, viscosity ratio equals 1.0. Similar to the Buckley-Leverett problem, the capillary diffusion effects were neglected

here by setting the capillary diffusion constant to a value nearly zero (Table 2.3). The pressure at the injector located at the lower left model corner was fixed at 2.0×10^6 Pa. The producer was located at upper right model corner. Its pressure is fixed at 0.0 Pa. This corresponds to a pressure gradient of 9.3×10^3 Pa/m along the line connecting the corners. The pressure equation was solved once at the beginning of the simulation and the resulting velocity field was held constant during the whole simulation. This ensures a constant CFL time step (Eq. 2.9) during the simulation such that the explicit and the implicit solutions of the saturation equation are directly comparable to each other. The time step for the IMPES method is then $\Delta t_{IMPES} = \Delta t_{CFL} = 1.374 \times 10^3$ sec. For the implicit solver, the time step was set to $\Delta t_{IMPIS} = \Delta t_{CFL} * 50 = 6.87 \times 10^4$ sec, an overstepping factor of 50.

Figure 2.11 shows the simulation results obtained with IMPES and IMPIS methods after 32 days (a), 72 days (b) and 95 days (c). Water flows radially from the lower left corner towards the producer until the impermeable barrier is reached, where the water front has to circumvent the barrier.

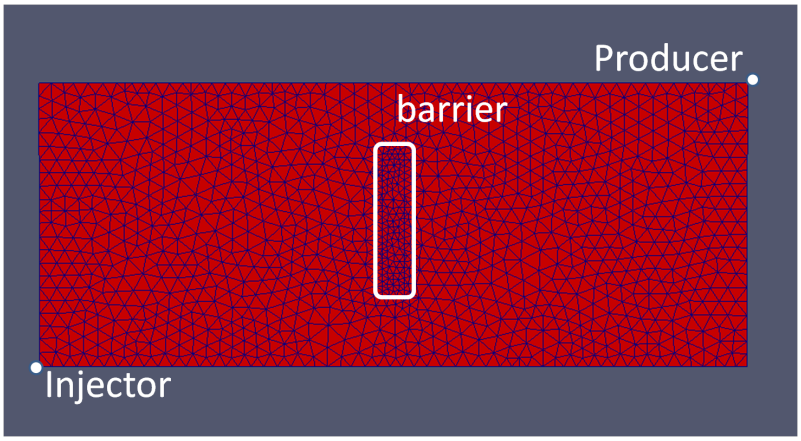

Figure 2.10: A 2D unstructured mesh for the quarter five spot simulations with an injector in the lower left and an producer in the upper right model corner. The dimensions are 200 $m \times 80$ m. An impermeable barrier is located in the model centre. The mesh contains 2352 finite elements. The complementary FV grid consists of 1256 finite volumes. The rock and fluid properties for the simulation are listed in Table 2.3.

The water fronts obtained with the IMPIS scheme are at the same position as the ones computed by the IMPES method at all times but are smeared due to numerical dispersion inherent to implicit time stepping. This behaviour can be ob-

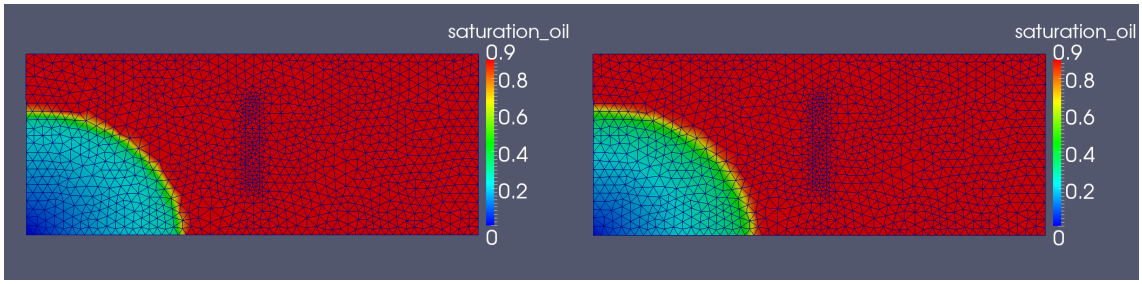

(a)

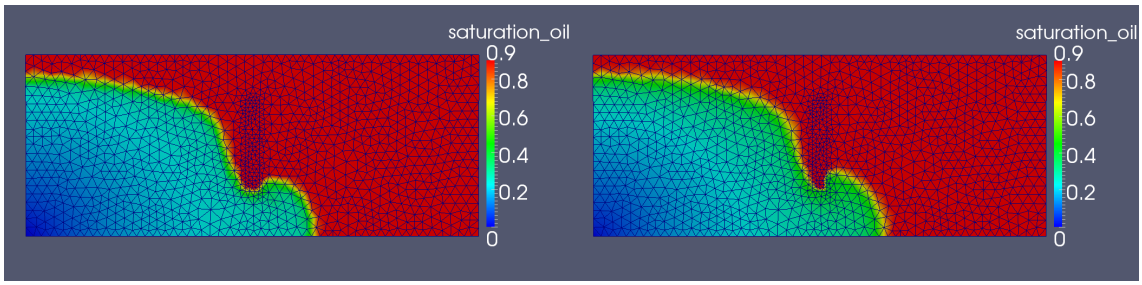

(b)

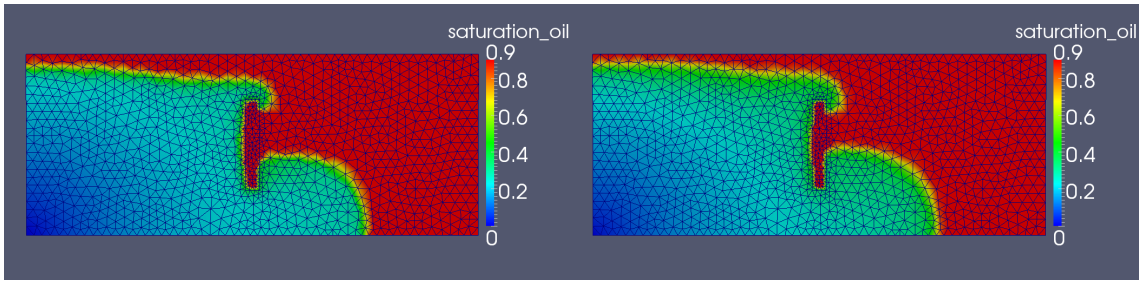

(c)

Figure 2.11: Water distribution in a quarter five spot model with an impermeable barrier (see Fig. 2.10) after 32 days (a), 72 days (b) and 95 days (c) comparing the IMPES (left) and IMPIS scheme (right). The water fronts are located at the same position although the fronts obtained with the IMPIS method are slightly more diffuse because of the numerical dispersion inherent to implicit time stepping schemes.

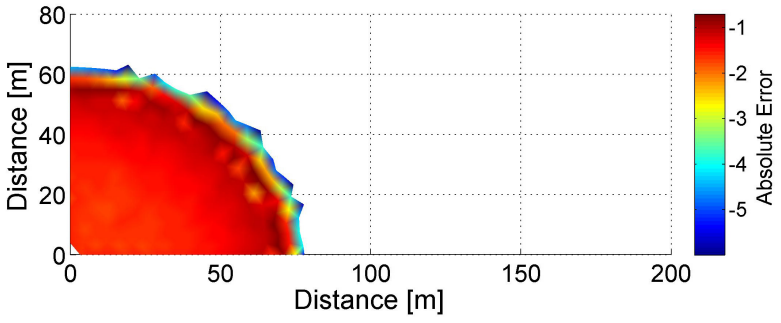

(a)

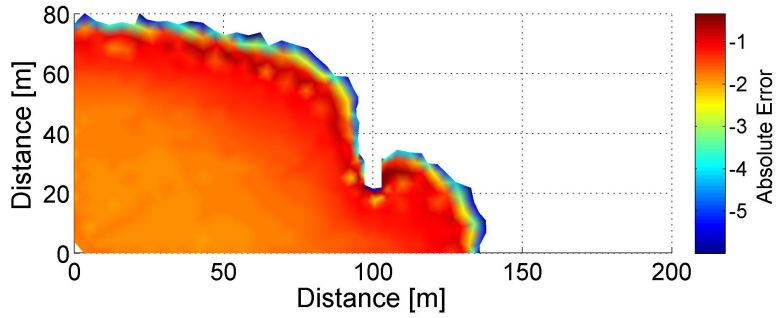

(b)

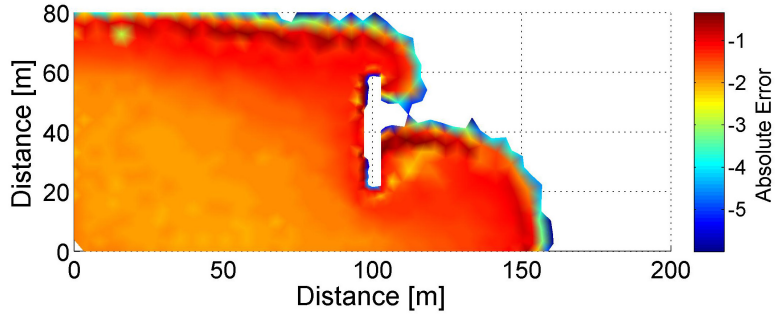

(c)

Figure 2.12: Absolute error defined as $|S_{w,IMPES} - S_{w,IMPIS}|$ for the IMPIS method after 32 days (a), 72 days (b) and 95 days (c). Note that the colour bar is in log_{10} scale. The highest discrepancy to the IMPES reference solution occurs immediately at the water front and is caused by numerical dispersion.

Parameter		Value	Unit
matrix permeability	K_m	1000	mD
matrix porosity	ϕ_m	0.25	$[-]$
fracture permeability	K_f	1.0×10^{-3}	mD
fracture porosity	ϕ_f	0.25	$[-]$
diffusivity	D	1.0×10^{-25}	$[m^2/sec]$
density water	ρ_w	1000	kg/m^3
density oil	ρ_o	1000	kg/m^3
initial water saturation	S_{wi}	0.1	$[-]$
initial oil saturation	S_{oi}	0.9	$[-]$
residual water saturation	S_{wr}	0.0	$[-]$
residual oil saturation	S_{or}	0.0	$[-]$
Brooks Corey exponent	λ_{BC}	3.0	$[-]$
viscosity water	μ_w	1.0×10^{-3}	$Pa \cdot s$
viscosity oil	μ_o	1.0×10^{-3}	$Pa \cdot s$

Table 2.3: Rock and fluid properties for the quarter five spot simulations (Fig. 2.10).

served in Fig. 2.12 which shows the difference in saturations between the IMPES and IMPIS approaches. Taking the explicit solution as a reference, the absolute error for the IMPIS approach is calculated as

$$error = |S_{w,IMPES} - S_{w,IMPIS}|. \tag{2.31}$$

The highest difference in the saturation values can be observed immediately at the water front where the error reaches values of nearly 10%. However, behind the front, the error reduces to 1% and less. This is a satisfying result considering that with the IMPIS method, the CPU time was around ten times less compared to the IMPES approach (Tab. 2.4).

Simulation	IMPES	IMPIS	speed-up factor
Quarter Five Spot	258 *sec*	27 *sec*	9.56

Table 2.4: CPU time for the quarter five spot two-phase flow simulation for a model time of 95 days. The IMPIS method is approximately ten times faster than the IMPES method with comparable accuracy of the simulation result (Fig. 2.11).

2.3.3 *Bristol Channel Model*

To analyse the performance of IMPES and IMPIS methods using the DFM approach, two-phase flow in a model of a fractured limestone outcrop in the Bristol Channel (Belayneh, 2004) (Fig. 2.13) was simulated. The model dimensions are $8\ m \times 5\ m$. The corresponding finite element mesh (Fig. 2.13 c) consists of 302061 elements and 151399 nodes. The rock matrix has a permeability of 100 mD and the fractures are 100 times more permeable. A horizontal injector was located at the left model boundary. Its pressure was fixed at $1.248 \times 10^7\ Pa$. A horizontal producer was located at the right model boundary and its pressure was fixed at $1.234 \times 10^7\ Pa$. For the first simulation, a viscosity ratio of 1 was considered ($\mu_w = \mu_o = 1.0 \times 10^{-3}\ Pa \cdot s$), for the second the viscosity of oil was increased to $\mu_o = 5.0 \times 10^{-3}\ Pa \cdot s$ such that $\mu_w/\mu_o = 0.2$ (Table 2.5). As in the previous cases, capillary diffusion was neglected and the velocity field was held constant throughout the simulation after the initial solution of the pressure equation.

For the first simulation with the viscosity ratio of 1.0, the time step given by CFL condition is $\Delta t_{IMPES} = 2.77\ sec$. This small time step was to be expected as the elements representing the fractures are small but their velocity is high because the permeability is 100 times higher in the fractures than the rock matrix. Again, the time step for the implicit solver of the advection equation is chosen by multiplying it with a overstepping factor of 50 as $\Delta t_{IMPIS} = 138.40\ sec$.

Figure 2.14 shows the water fronts after 0.5 day (a) and 1 day (b) of flow simulation for the viscosity ratio of 1.0. Water propagates quickly through the high permeable fractures and enters the rock matrix only at a later stage. The highest absolute error for the IMPIS scheme compared to the IMPES method again occurs immediately at the water front in the fractures (Fig. 2.15). The region of highest absolute error increases during the simulation as numerical dispersion increases with time, but the error remains at $1\% - 3\%$ compared to the IMPES scheme, which is still acceptable. The speed-up factor for the IMPES scheme is 27.22 (Tab. 2.6). This speed-up is remarkable considering that a simulation can now be performed within a single day with the IMPIS method compared to a

(a)

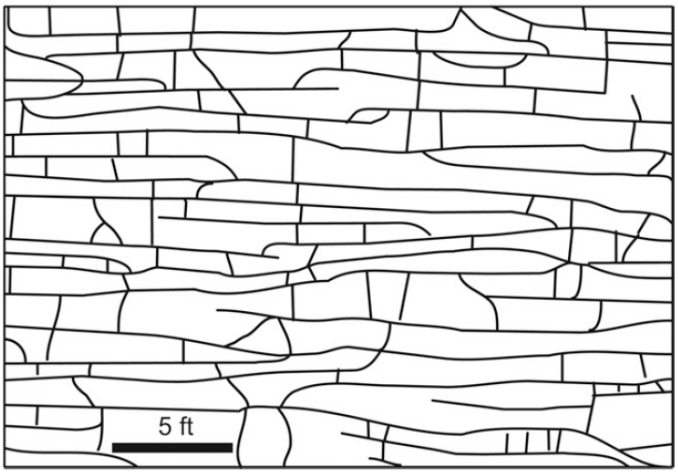

(b)

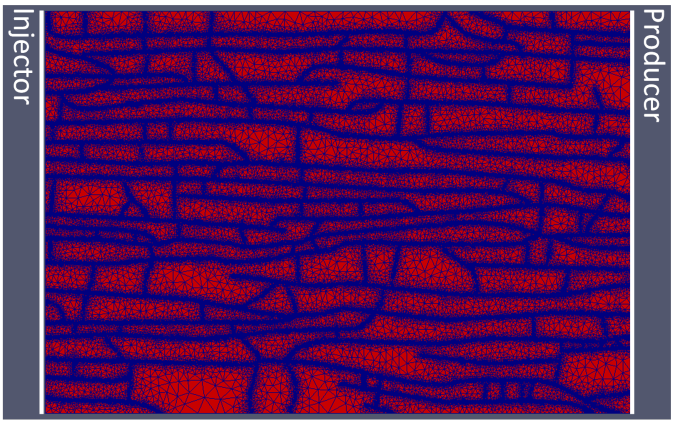

(c)

Figure 2.13: A photograph of a fractured limestone outcrop in the Bristol Channel, UK (a), its geometrical representation (map view) (b) and the corresponding unstructured finite element mesh (c) (Geiger et al., 2009b). The properties for the simulations are listed in Table 2.5. A horizontal injector and a producer operating at fixed pressure were placed on the left hand side boundary and the right hand side boundary, respectively. The mesh contains 302061 finite elements and 151399 finite volumes. Note that many small elements are needed to discretise the fractures which have an aperture of approximately 1 mm. The small FEs will affect the time step for the IMPES method via the CFL condition.

Parameter		Value	Unit
matrix permeability	K_m	100	mD
matrix porosity	ϕ_m	0.2	$[-]$
fracture permeability	K_f	10	D
fracture porosity	ϕ_f	1.0	$[-]$
diffusivity	D	1.0×10^{-25}	$[m^2/sec]$
density water	ρ_w	1000	kg/m^3
density oil	ρ_o	1000	kg/m^3
initial water saturation	S_{wi}	0.3	$[-]$
initial oil saturation	S_{oi}	0.7	$[-]$
residual water saturation	S_{wr}	0.0	$[-]$
residual oil saturation	S_{or}	0.0	$[-]$
Brooks Corey exponent	λ_{BC}	3.0	$[-]$
Simulation 1			
viscosity water	μ_w	1.0×10^{-3}	$Pa \cdot s$
viscosity oil	μ_o	1.0×10^{-3}	$Pa \cdot s$
Simulation 2			
viscosity water	μ_w	1.0×10^{-3}	$Pa \cdot s$
viscosity oil	μ_o	5.0×10^{-3}	$Pa \cdot s$

Table 2.5: Rock and fluid properties used for two-phase flow simulations in the Bristol Channel model (Fig. 2.13).

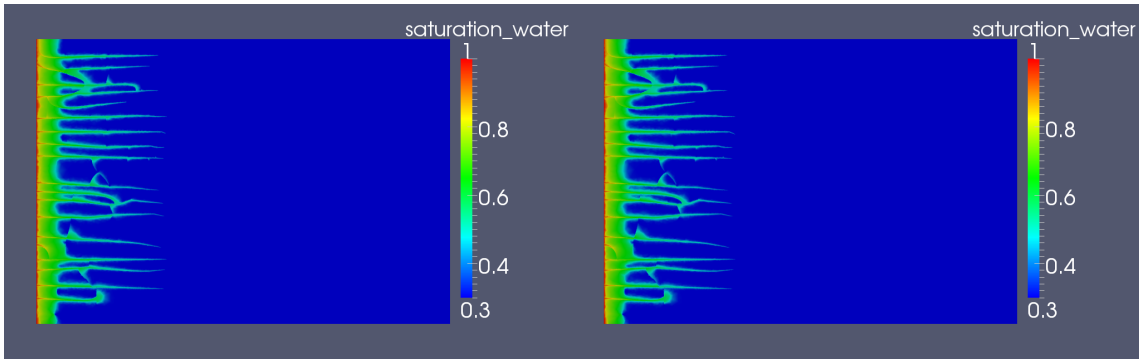

(a)

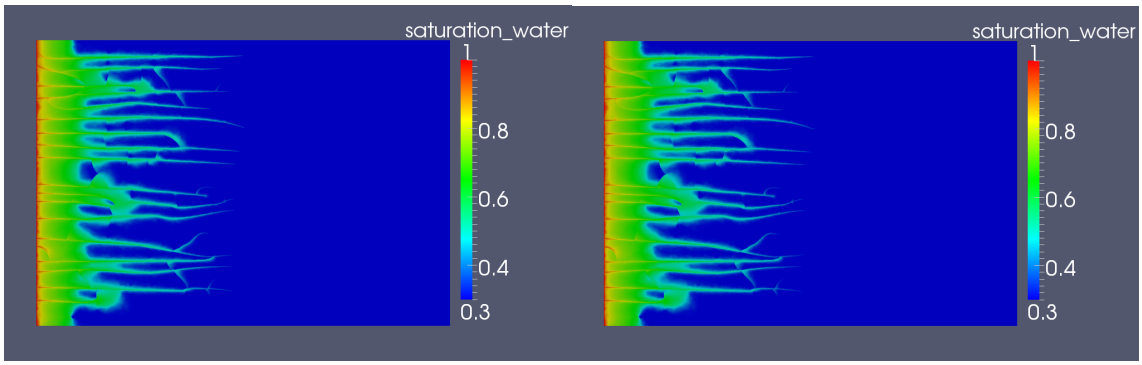

(b)

Figure 2.14: Water distribution for the first two-phase flow simulation in the Bristol Channel model with a viscosity ratio of 1.0 after 0.5 day (a) and 1 day (b) using the IMPES method (left) and the IMPIS method (right). The water fronts are located at the same position. The difference between the two time stepping schemes is visually not observable.

month with the IMPES scheme.

Figure 2.16 shows the water fronts after 0.5 day (a) and 1 day (b) of flow simulation for the viscosity ratio of 0.2. Compared to the previous Bristol Channel simulation, the water front propagates notably slower because of the increased oil viscosity. Note that this slower propagation of the water front compared to the case with a viscosity ratio of 1.0 is due to the boundary conditions in this simulation where pressures are kept constant at injector and producer. This behaviour is also observed in the IMPES time step that satisfies the CFL condition, which is now $\Delta t_{IMPES} = 12.43\ sec$, i.e. four times higher than in the previous simulation. The time step for the IMPIS method was chosen accordingly as $\Delta t_{IMPIS} = 621.5\ sec$ (factor 50).

The absolute error for the IMPIS scheme compared to the IMPES reference solution is nearly zero across the whole domain (Fig. 2.17). The CPU time for both schemes decreased. It decreased by a factor of 4.4 in the IMPES method and by a factor of 2.3 in the IMPIS method. Therefore, the speed-up factor of the IMPIS method was only 14.64 (Tab. 2.6).

Simulation	IMPES	IMPIS	speed-up factor
$\mu_w/\mu_o = 1.0$	458044 *sec*	16827 *sec*	27.22
$\mu_w/\mu_o = 0.2$	104725 *sec*	7154 *sec*	14.64

Table 2.6: CPU time for two-phase flow simulation in the Bristol Channel model for a model time of 1 day. The IMPIS method is around 27 times faster than the IMPES method for a viscosity ratio of 1.0 and 14 times faster for a viscosity ratio of 0.2. In both cases, IMPES and IMPIS method have comparable accuracy.

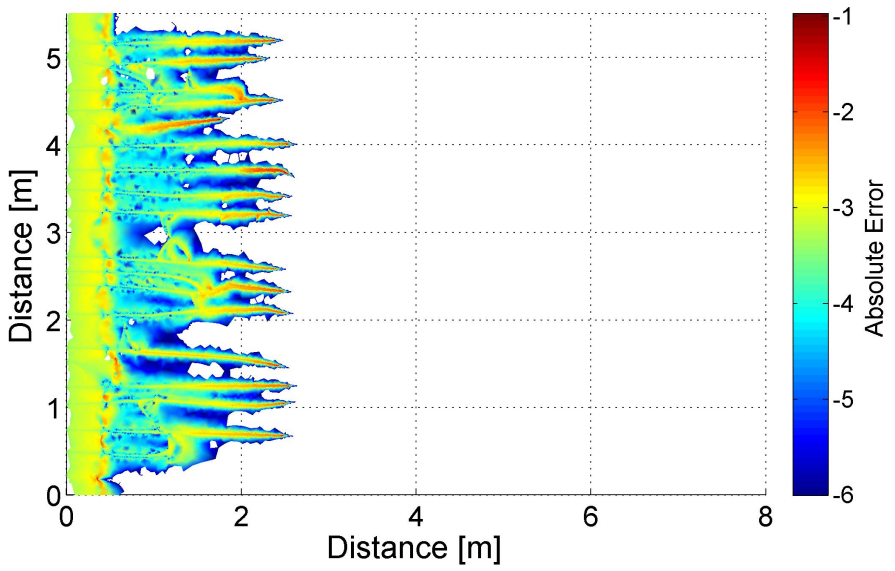

(a)

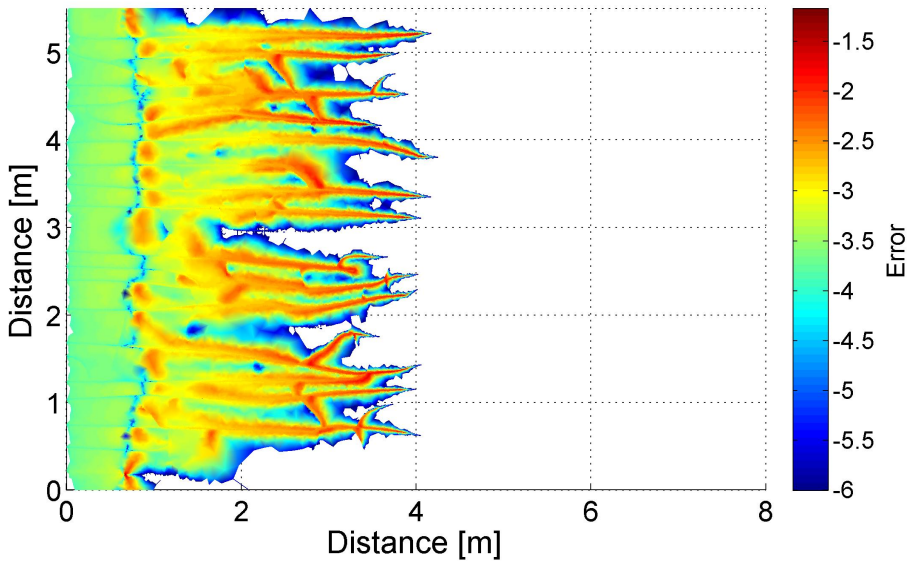

(b)

Figure 2.15: Absolute error defined as $|S_{w,IMPES} - S_{w,IMPIS}|$ for the two-phase flow simulation using the IMPIS method after 0.5 day (a) and 1 day (c) in the Bristol Channel model with a viscosity ratio of 1.0. Note that the colour bar is in log_{10} scale. The highest discrepancy to the IMPES reference solution occurs immediately at the water front in the fractures and is caused by numerical dispersion, inherent to implicit time stepping schemes. The maximum absolute error is 3%.

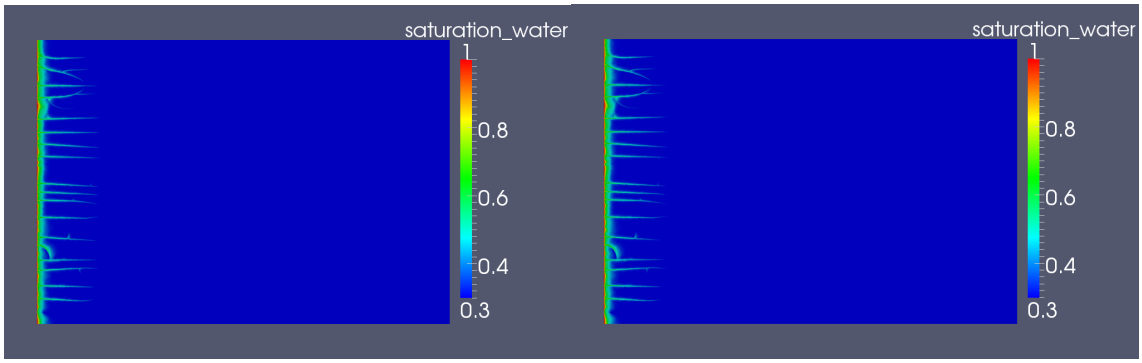

(a)

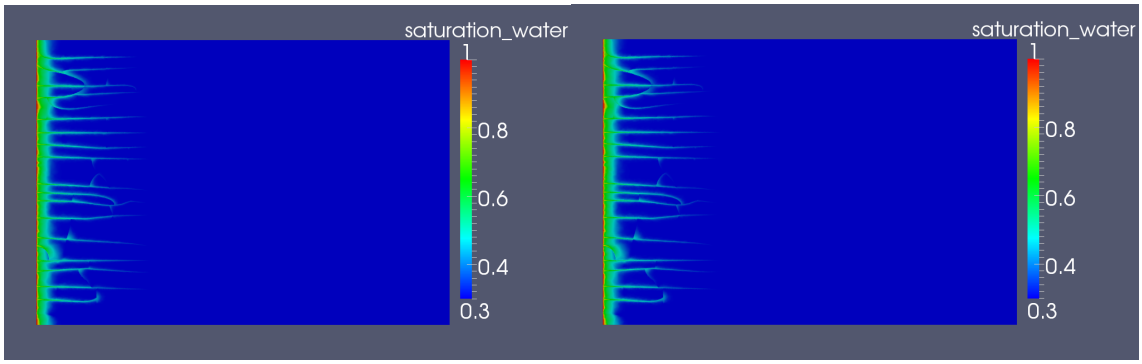

(b)

Figure 2.16: Water distribution for the second two-phase flow simulation in the Bristol Channel model with viscosity ratio of 0.2 after 0.5 day (a) and 1 day (b) using the IMPES method (left) and the IMPIS method (right). The water fronts are located at the same position. The difference between the two time stepping schemes is visually not observable.

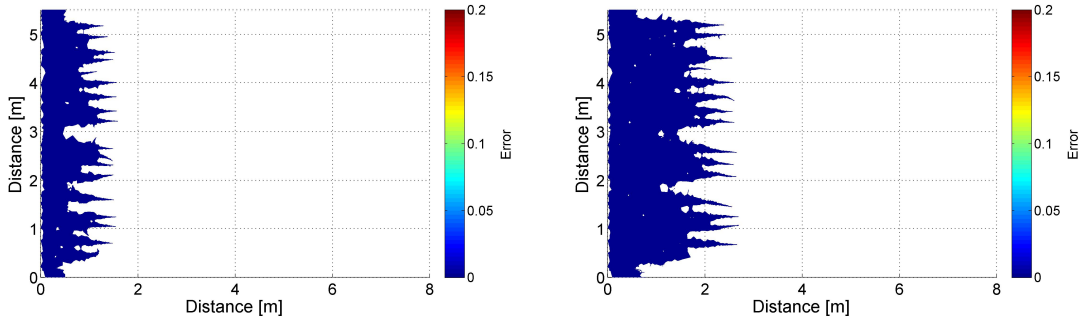

(a) (b)

Figure 2.17: Absolute error defined as $|S_{w,IMPES} - S_{w,IMPIS}|$ for the two-phase flow simulation using the IMPIS method after 0.5 day (a) and 1 day (c) in the Bristol Channel model with a viscosity ratio of 0.2. Note that the colour bar is in log_{10} scale. The error for IMPIS compared to the IMPES reference solution is nearly zero across the entire model.

2.4 SUMMARY

In this chapter, the DFM approach for modelling NFR was presented. It represents the fractures as well as the matrix explicitly using a hybrid finite element finite volume grid, i.e. a grid where different types of elements with different dimensions are combined. Assuming incompressible, immiscible and isothermal two-phase flow, the governing equations are solved sequentially, that is they have been decoupled into a pressure and a saturation equation. The solution for the pressure field is obtained by applying a standard Galerkin FEM scheme with implicit time stepping. The saturation equation is solved on a complementary FV grid using implicit time stepping and an iterative Newton method. The Newton method was enhanced with a line search backtracking algorithm as a global convergence safeguard.

It was demonstrated that the resulting Implicit Pressure - Implicit Saturation (IMPIS) has similar accuracy compared to the classical IMPES scheme which served as a reference solution when applied to heterogeneous media. The absolute error was between 1% and 10%. The largest error always occurred at close proximity to the saturation fronts. The error was negligible away from the front. This is because of the numerical dispersion inherent to implicit schemes. A speed-up factor of at least ten was achieved for the presented examples. However, the speed up factor depends on the particular problem at hand and no general statements can be given for a arbitrary models of a NFR. But it is expected that the IMPIS scheme will be increasingly more efficient compared to the IMPES scheme when the contrast in fluid velocities, and hence range of permissible time-steps in the model, increases.

Although the IMPIS scheme is not restricted by the CFL time step, it is still not unconditionally stable. The geometry of flow barrier and flow conduits seem to affect the stability of the IMPIS scheme. For example, for the 2D simulations presented here, an overstepping factor of > 60 for the CFL condition led to divergence of the Newton method. Also, the strong physical coupling of the pressure and the saturation equation requires frequent updates of the velocity field, and

hence pressure values, such that the time step is physically limited. An automatic calculation of the largest possible time step for which the implicit solver is still stable could not be identified and is subject to future work. The numerical error induced by the operator splitting will be studied later in Chapter 5.

A fully implicit scheme for solving two-phase equations (Eq. 2.1) would be unconditionally stable for arbitrary time steps but requires a more challenging treatment of the non-linear system and results in a more complex global solution matrix, in particular if unstructured grids are used. Comparison of fully implicit approach and the IMPIS method was not conducted for this thesis and is also subject to future work.

3

GENERAL DUAL-POROSITY MODELLING FOR CAPILLARY AND GRAVITY DRIVEN FRACTURE-MATRIX FLUID EXCHANGE

3.1 INTRODUCTION

Naturally Fractured Reservoirs (NFR) can often be classified as multi-continua media, comprising a flowing, high-permeable fracture domain and an immobile, i.e. stagnant, low-permeable matrix domain. Viscous and gravitational forces dominate in the fracture (flowing) domain while matrix domain (which provides the main storage) is dominated by capillary and gravitational forces. In the previous chapter, the Discrete Fracture and Matrix (DFM) approach was introduced to model fluid flow in both, fractures and matrix, simultaneously. If the advective fluid flow in the matrix is negligibly small, flow calculations can be restricted to the fractures only. The computational domain is then explicitly parted into the flowing fracture domain and the stagnant matrix domain, which is the so-called Dual-Porosity (DP) approach (Fig. 3.1).

Fractures-matrix fluid exchange is then modelled via the transfer function T, which contributes an additional source term for the flowing domain. Equation 2.8 therefore changes to

$$\phi \frac{\partial S_w}{\partial t} + \nabla \cdot \left(f_w v_t - \bar{\lambda} \left(\nabla P_c + \Delta \rho g \right) \right) - q = T. \tag{3.1}$$

The transfer function $T = f\left(L_c, \beta\right)$ depends on the matrix block sizes, that is the characteristic length of the matrix block L_c (i.e. $\sigma = L_c^{-2}$ is the shape factor), and the transfer rate coefficient β, which describes the speed of the fluid exchange

between fractures and the matrix due to rock and fluid properties.

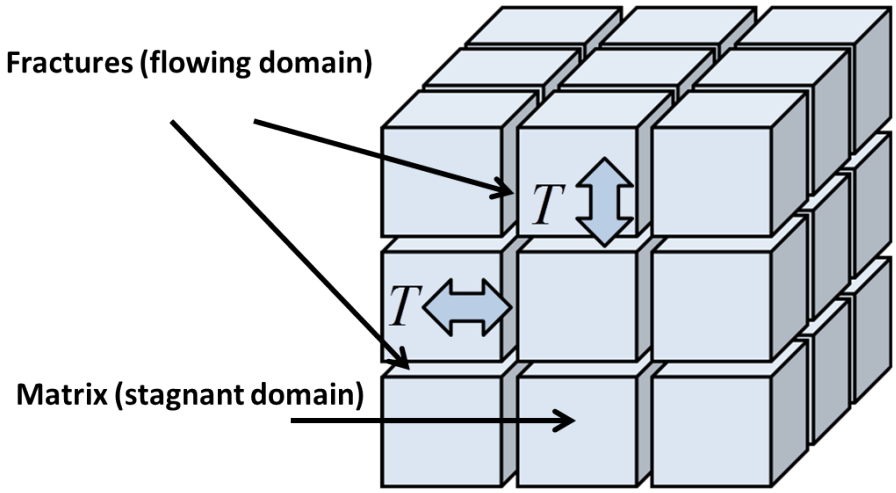

Figure 3.1: Conceptual representation of one simultaion grid block in Naturally Fractured Reservoirs (NFR) represented by a Dual-Porosity (DP) model. The DP model assumes uniformly distributed matrix blocks. Fracture - matrix fluid exchange is computed via a transfer function T.

The concept of the DP model was first introduced for single phase flow by Barenblatt et al. (1960); Warren and Root (1963) and later extended to two phase flow by Mattax and Kyte (1962). Since then, many more authors contributed to the improvement of the model (e.g., Kazemi et al., 1976; Gilman and Kazemi, 1983; Quandalle and Sabathier, 1989; Lu et al., 2008) by introducing new transfer functions for two and three-phase systems. These transfer functions include new shape factors to account for fracture spacing and new transfer rate coefficients based on calculation of fluid potentials in the matrix blocks to account more accurately for the two types of displacement of fluids in the rock matrix: Vertical displacement due to gravitational forces and all-directional displacement caused by capillary forces.

The ratio of capillary to gravitational forces

$$r = \frac{L}{L-H} = \frac{\Delta\rho g L}{\sigma J^*}\sqrt{\frac{K_m}{\phi_m}} \tag{3.2}$$

indicates which process is dominating in the rock matrix (Di Donato et al., 2006). Here, L is the height of the matrix block, H the amount of capillary rise of the wetting fluid in presence of a non wetting fluid, σ is the interfacial tension and

J^* refers to the entry pressure of the dimensionless Leverett J-function.

If the fluids have significantly different densities, i.e. $\Delta\rho >> 0$, and/or high matrix blocks are present in the geological formation such that L is large, then the capillary rise H is smaller than the height of the matrix block and one obtains $r >> 1$. In this case, the non-wetting fluid enters the matrix blocks from the top and replaces the wetting fluid due to gravitational forces downwards until the capillary-gravity equilibrium is reached. The gravitational drainage process takes place until the non-wetting fluid fills the upper sub-volume $(L - H)\, V_m$ of the matrix volume V_m.

On the other hand, if the capillary rise H is equal to or larger than the matrix block height L and hence $r \leq 1$, the transfer of the fluid between fracture and matrix is controlled by capillary forces and the main driving force for fluid exchange between fractures and matrix is spontaneous counter-current imbibition (e.g., Mattax and Kyte, 1962; Bourbiaux and Kalaydjian, 1990; Tavassoli et al., 2005; Hatiboglu and Babadagli, 2007). Spontaneous counter-current imbibition is induced by the difference of capillary pressure between the rock matrix and the fracture, causing the wetting fluid to imbibe the porous medium and expel the non-wetting fluid until the capillary equilibrium is reached, that is when the capillary pressure in the matrix becomes zero.

While the fluid exchange between fractures and matrix due to gravitational forces can be obtained by the analytical Buckley-Leverett solution for stable downward displacement of fluids in a two-phase system (Hagoort, 1980), the characterisation of fluid exchange between fractures and matrix due to spontaneous counter-current imbibition was based, until recently, on empirical models. Therefore, many empirical so-called scaling groups were developed to quantify and upscale the key parameters of the imbibition process. The principal idea of a scaling group is to non-dimensionalise the time of recovery during the spontaneous counter-current imbibition. Using a scaling group, hence, enables to simulate fracture matrix transfer in a DP model. The transfer can be quantified directly if the matrix is heterogeneous as different transfer functions can be estimated for the different scaling group. However, since these scaling groups were

derived empirically, they were restricted to particular rock and fluid properties and yielded poor predictions of fluid recovery if the rock-fluid system differed. As a consequence, using scaling groups in transfer function of DP models can lead to inaccurate recovery predictions if the scaling group is inadequate for the chosen rock-fluid system.

Schmid and Geiger (2012, 2013) derived a scaling group based on an analytical solution of spontaneous counter-current imbibition by McWhorter and Sunada (1990). This scaling group does not imply any restrictive assumptions other than that the two-phase Darcy's law is valid. It is hence applicable to arbitrary rock and fluid properties and can be used straightforwardly in a DP model.

This chapter is structured as follows. In the next two sections, the transfer functions for spontaneous counter-current imbibition and for gravity drainage modelling are introduced. The former is based on the general scaling group for spontaneous imbibition and the later on the two-phase Buckley-Leverett solution. Then the transfer functions are validated for one-dimensional fluid exchange comparing the simulation results to published laboratory experiments on Berea sandstone cores and artificial consolidated porous media. Finally, recent shape factors and their ability to capture three-dimensional imbibition processes are reviewed.

3.2 DUAL POROSITY TRANSFER FUNCTION FOR SPONTANEOUS IMBIBITION

3.2.1 *Analytical Solution for Spontaneous Counter-Current Imbibition*

Schmid and Geiger (2012, 2013) derived a general scaling group for spontaneous counter-current imbibition assuming that capillary forces dominate, i.e. if fluid densities are similar and/or the matrix blocks are not high such that gravitational forces could be neglected here. The detailed derivation is discussed in Schmid et al. (2011) and Schmid and Geiger (2012, 2013). For brevity, only the

salient features are discussed here. The mass balance for incompressible and immiscible two-phase flow is given by

$$\phi \frac{\partial S_\alpha}{\partial t} = -\nabla q_\alpha \tag{3.3}$$

where ϕ is the porosity, S is the saturation of phase α and q refers to the volumetric flow rate of phase α:

$$q_\alpha = -K \frac{k_{r\alpha}}{\mu_\alpha} \nabla p_\alpha. \tag{3.4}$$

Combining Eqs. 3.3 and 3.4, capillary-driven diffusion of saturation in the rock matrix can be modelled as

$$\phi \frac{\partial S_{wm}}{\partial t} = \nabla \left(D\left(S_{wm}\right) \nabla S_{wm} \right). \tag{3.5}$$

$D\left(S_{wm}\right)$ denotes the capillary dispersion coefficient of the fluid phases

$$D\left(S_{wm}\right) = -K \lambda_{nw} f\left(S_{wm}\right) \frac{dp_c}{dS_{wm}}, \tag{3.6}$$

where p_c is the capillary pressure. K refers to the matrix permeability while $\lambda_{nw} f\left(S_{wm}\right)$ is the the mobility of the non-wetting fluid times fractional flow. McWhorter and Sunada (1990) derived a solution for equation 3.6 assuming specific boundary conditions

$$\begin{aligned} S_{wm}\left(x = 0, t\right) &= 1 - S_{nwr} \\ S_{wm}\left(x, t = 0\right) = S_{wm}\left(\infty, t = 0\right) &= S_{wmc}, \end{aligned} \tag{3.7}$$

with the residual non-wetting saturation S_{wnr} and the connate wetting fluid saturation S_{wmc}. Schmid et al. (2011) showed that their solution is not specific but a general solution for spontaneous counter-current imbibition: The cumulative volume of water imbibed from the fracture into the matrix at a time t can be calculated as

$$Q_w\left(t\right) = 2At^{1/2} \tag{3.8}$$

with A being a parameter that is uniquely defined for any fluid and rock parameters (McWhorter and Sunada, 1990; Schmid et al., 2011)

$$A = \sqrt{\frac{\phi}{2} \int_{S_{wmc}}^{S_{wf}^{max}} \frac{(S_w - S_{wmc})\, D\,(S_w)}{F\,(S_w)} dS_w}. \tag{3.9}$$

$F(S_w)$ is the non-linear fractional flow function for the counter-current imbibition and can be seen as an analogue to the fractional flow function $f(S_w)$ in the Buckley-Leverett solution (Buckley and Leverett, 1942), but here includes capillarity

$$F\,(S_w) = 1 - \frac{\left[\int_{S_w}^{S_{wf}^{max}} \frac{(\beta - S_w) D(\beta)}{F(\beta)} d\beta\right]}{\left[\int_{S_{wmc}}^{S_{wf}^{max}} \frac{(\beta - S_{wmc}) D(\beta)}{F(\beta)} d\beta\right]}. \tag{3.10}$$

S_{wmc} is the initial or connate saturation of the wetting fluid in the matrix, where S_{wf}^{max} is the wetting phase saturation in the adjacent fracture.

The parameter A can be computed using an iterative Newton method as showed by Fucik et al. (2007). An alternative approach to calculate A was introduced by Bjørnara and Mathias (2013) using a Chebyshev spectral collocation method.

The cumulative volume of water imbibed, together with the corresponding characteristic length L_c provides the universal scaling group for arbitrary petrophysical and fluid properties:

$$t_D = \left(\frac{Q_w\,(t)}{\phi L_c}\right)^2 = t\left(\frac{2A}{\phi L_c}\right)^2 \tag{3.11}$$

The transfer rate coefficient β, which is needed for our dual-porosity model, is now given as

$$\beta^{SI} = \left(\frac{2A}{\phi L_c}\right)^2. \tag{3.12}$$

All parameters in Eq. 3.12 can be measured in the laboratory or estimated using pore-network modelling (Blunt, 2001; Blunt et al., 2002, 2013). Importantly,

because the transfer function is based on an exact analytical solution, data from laboratory experiments can be upscaled directly to the field scale, leaving the characteristic length L_c (or the shape factor $\sigma = L_c^{-2}$) as the only unknown because the fracture properties at reservoir conditions are difficult to establish.

3.2.2 *Spontaneous Imbibition Transfer Function*

The exact analytical solution is valid until time

$$t^* = \left(\frac{\phi L_c}{2AF'(S_w)} \right)^2, \tag{3.13}$$

that is the time when the imbibition front reaches the nearest no-flow boundary. Nonetheless, a good approximation of the recovery beyond that point can be obtained from the exponential model of Aronofsky et al. (1958),

$$\frac{R}{R_\infty} = \left(1 - e^{\gamma \beta^{SI} t} \right) = \frac{S_{wm} - S_{wmc}}{1 - S_{nwr} - S_{wmc}}, \tag{3.14}$$

where R is the recovery of the non wetting phase, R_∞ the ultimate recovery and β^{SI} is the transfer rate coefficient (Eq. 3.12). γ is a fitting parameter and can be determined by fitting R to experimental data. Schmid and Geiger (2013) showed that setting $\gamma \approx 70$ already covers spontaneous imbibition simulations for over 40 laboratory experiments. Using Eq. 3.14, I follow Di Donato et al. (2007) and derive the transfer function T^{SI} for spontaneous counter-current imbibition for a matrix block surrounded by fractures

$$T^{SI} = \begin{cases} \gamma \beta^{SI} \phi_m \left(1 - S_{nwr} - S_{wm} \right), & S_{wf} > 0 \\ 0, & S_{wf} = 0 \end{cases}. \tag{3.15}$$

Here, S_{wf} is the wetting fluid saturation in the fractures. If the surface area of the matrix block is not in contact with the wetting fluid, spontaneous imbibition cannot occur and the transfer is zero.

Note that Eq. 3.15 describes a first order mass transfer, which assumes uniform or averaged saturation in the matrix, i.e. a linear saturation gradient. For

modelling the spatial distribution of the wetting fluid saturation, higher order rate models should be considered (see e.g. Haggerty and Gorelick, 1995; Geiger et al., 2013; Tecklenburg et al., 2013).

3.3 DUAL POROSITY TRANSFER FUNCTION FOR GRAVITY DRAINAGE

The transfer function describing the gravity drainage process is based on the Buckley-Leverett solution for stable downward displacement of the wetting fluid (e.g. oil) due to injection of a non-wetting fluid (e.g. gas). Assuming that the gas is incompressible, an assumption that is valid if the average pressure in the reservoir is at least an order of magnitude higher than the pressure drop during the field life, the two-phase Darcy flow for vertical displacement can be written as (Di Donato et al., 2006)

$$\phi \frac{\partial S_w}{\partial t} + \frac{\partial q_w}{\partial z}, \tag{3.16}$$

with q_w being the wetting phase flow rate

$$q_w = \frac{\lambda_w}{\lambda_t} q_t + \frac{K \lambda_w \lambda_{nw}}{\lambda_t} \frac{\partial p_c}{\partial z} + \frac{K \lambda_w \lambda_{nw} \left(\rho_w - \rho_{nw}\right) g}{\lambda_t}. \tag{3.17}$$

Here $q_t = q_w + q_{nw}$ is the total flow rate, $p_c = p_{nw} - p_w$ is the capillary pressure and $\lambda_t = \lambda_w + \lambda_{nw}$ is the total mobility.

Hagoort (1980) suggested that capillary forces during a gravitational drainage process are negligible such that the capillary term can be omitted. He also assumed that the non-wetting phase mobility is much higher than the wetting phase mobility and the mobility ratio terms in Eq. 3.17 can be neglected as well. He then non-dimensionalised Eq. 3.16 by introducing the reduced porosity

$$\phi^* = \phi \left(1 - S_{wr} - S_{im}\right), \tag{3.18}$$

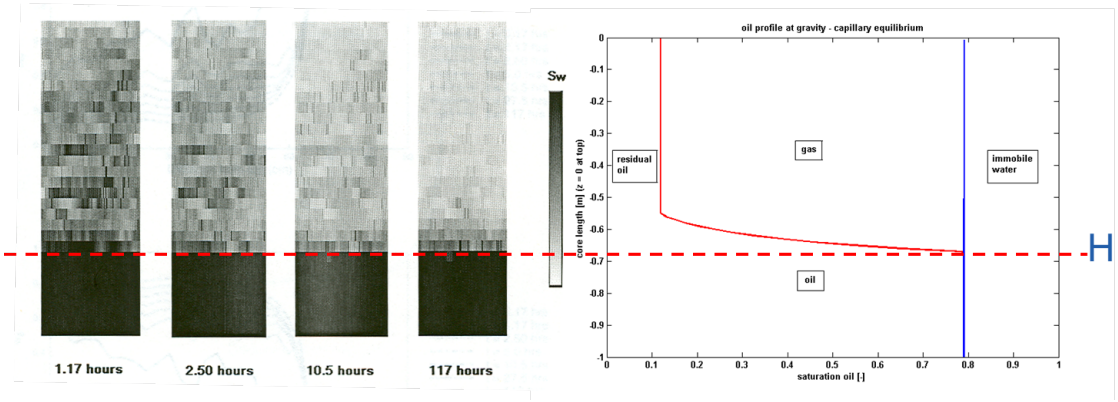

Figure 3.2: Left: X-ray CT scans from a gravity drainage experiment obtained by Sahni (1998). The gas enters the core that is initially saturated with oil and immobile, connate water at the top. Oil drains freely under gravity until the capillary gravity equilibrium is reached. Right: Oil saturation profile at capillary gravity equilibrium. The height of the gas reached its final position at the capillary rise H.

the effective wetting phase saturation

$$S_w^* = \frac{S_w - S_{wr}}{1 - S_{im} - S_{wr}}, \tag{3.19}$$

the dimensionless distance

$$z_D = \frac{z}{L}, \tag{3.20}$$

and the dimensionless time

$$t_D = \frac{K\Delta\rho g}{\mu_w \phi^* L} t. \tag{3.21}$$

Now the Buckley Leverett solution can be readily applied to the reduced equation

$$\frac{\partial S_w^*}{\partial t_D} + k'_{rw} \frac{\partial S_w^*}{\partial z_D}. \tag{3.22}$$

With the wetting fluid saturation profile obtained from the Buckley-Leverett analysis, the average recovery at late time can then be calculated as (Hagoort, 1980; Di Donato et al., 2006):

$$\frac{R}{R_\infty} = 1 - \frac{\left(\beta^{GD} t\right)^{-\frac{1}{a-1}}}{S_{nw}^*}, \tag{3.23}$$

where S^*_{nw} is the maximum possible non-wetting fluid saturation

$$S^*_{nw} = R_\infty = (1 - S_{im})\, L - \int_0^L P^{-1}_{cwnw}\left(\Delta\rho g h\right) dh \tag{3.24}$$

in the matrix block. $P^{-1}_{cwnw}\left(\Delta\rho g h\right)$ is the saturation profile of the wetting fluid after reaching the capillary gravity equilibrium. β^{GD} is the transfer rate coefficient for gravity drainage

$$\beta^{GD} = \frac{a^a K_m k^{max}_{rwm} \Delta\rho g}{(a-1)^{a-1}\phi_m \mu_w L}. \tag{3.25}$$

Here, the characteristic length L is the height of the matrix block and the exponent a is defined such that

$$k_{rw} = k^{max}_{rwm}\left(S_{wm} - S_{wrm}\right)^a \tag{3.26}$$

holds for low wetting fluid saturations (Di Donato et al., 2007).

The gravity drainage transfer function T^{GD} can now be written as

$$T^{GD} = \begin{cases} \frac{\beta^{GD}\phi_m}{a-1}\left(S^*_{nw} - S_{nwm}\right)^a, & S_{nwf} > 0 \\ 0, & S_{nwf} = 0 \end{cases}. \tag{3.27}$$

3.4 SATURATION UPDATE IN THE FLOWING DOMAIN

The update of the saturations in the fracture domain at time step $n+1$ for the cell j can now be computed using operator splitting as

$$S^{n+1}_{fj} = S^{n+1,int}_{fj} - \frac{\phi_m}{\phi_f}\left(S^{n+1}_{mj} - S^n_{mj}\right), \tag{3.28}$$

where $S^{n+1,int}_{fj}$ is the interim fracture saturation after the advection computation in the flowing domain and ϕ_f is the fracture porosity. S^n_{mj} is the previous rock

matrix saturation in the virtual matrix cell j at time step n and S_{mj}^{n+1} is the new saturation at time $n+1$ calculated as

$$S_{mj}^{n+1} = S_{wmj}^{n+1} = S_{wj}^{*} - \left(S_{wj}^{*} - S_{wmj}^{n}\right) e^{-\gamma \beta^{SI} \Delta t}, \tag{3.29}$$

applying the transfer function T^{SI} (Eq. 3.15) when $r \leq 1$, or in case of gravity driven fluid exchange ($r > 1$) using T^{GD} (Eq. 3.27)

$$S_{mj}^{n+1} = S_{nwmj}^{n+1} = S_{nwj}^{*} - \left(\left(S_{nwj}^{*} - S_{nwmj}^{n}\right)^{1-a} + \beta^{GD} \Delta t\right)^{-\frac{1}{a-1}}. \tag{3.30}$$

Here β^{SI} and β^{GD} are the transfer rate coefficients for spontaneous imbibition (Eq. 3.12) and gravitational drainage (Eq. 3.25), respectively.

To ensure that not more fluid enters the matrix blocks than initially available in the fracture domain, for all cells j with $S_{fj}^{n+1,int} < 0$ the saturations in the rock matrix sub-domain are recalculated as

$$S_{mj}^{n+1} = S_{mj}^{n} + \frac{\phi_f}{\phi_m} S_{fj}^{n+1,int}, \tag{3.31}$$

and fracture saturation is then set to zero ($S_{fj}^{n+1} = 0$).

3.5 VALIDATION WITH EXPERIMENTS

I am now presenting a suite of DP simulations to validate the previously introduced transfer functions for fracture-matrix fluid exchange due to capillary T^{SI} and gravitational forces T^{GD}. These DP simulations are compared with published data from laboratory experiments (Zhang et al., 1996; Babadagli and Hatiboglu, 2007; Pedrera et al., 2002). Further validations of the general scaling group for spontaneous counter-current imbibition for water-wet and mixed-wet rocks can be found in Schmid and Geiger (2012, 2013).

3.5.1 *Spontaneous Counter-Current Imbibition*

The laboratory experiments were performed on Berea sandstone cores, which were epoxy sealed, leaving one side open for imbibition Fig. 3.3a. The samples were saturated with hydrocarbons or air as the non-wetting phase. The cores were oriented horizontally when put in contact with the wetting fluid for imbibition. The size of the cores and their horizontal position allow me to neglect gravity effects. Table 3.1 gives the rock and fluid properties used in experiment 'BC13' and '17' of Zhang et al. (1996) and Babadagli and Hatiboglu (2007), respectively. For one-dimensional DP simulations, relative permeability and capillary pressure curves derived from pore-network modelling (Valvatne and Blunt, 2004) were used. These relative permeability and capillary pressure curves showed good agreement with experimental data conducted by Oak (1990) on water-wet Berea cores (Fig. 3.3 (b) and (c)). Thus, having accurate relative permeability and capillary pressure curves can minimise errors related to the two-phase flow functions and hence the accuracy of the universal transfer coefficient β^{SI} (Eq. 3.12) can be tested more thoroughly.

As mentioned earlier, many empirical derived scaling groups for spontaneous imbibition exist to date (Morrow and Mason, 2001; Schmid and Geiger, 2012). To demonstrate the performance of the universal transfer rate β^{SI} (Eq. 3.12), it is compared to simulations with two well-known empirical formulations for the transfer rate coefficient β. These are the rate coefficient of Ma et al. (1997)

$$\beta_{Ma} = \sqrt{\frac{K}{\phi}} \frac{\sigma}{\sqrt{\mu_w \mu_{nw}}} \frac{1}{L_c^2} \tag{3.32}$$

and the rate coefficient of Zhou et al. (2002)

$$\beta_{Zhou} = \sqrt{\frac{K}{\phi}} \frac{\sigma}{L_c^2} \sqrt{\lambda_{rw}^* \lambda_{rnw}^*} \frac{1}{\sqrt{M^*} + \frac{1}{\sqrt{M^*}}}, \tag{3.33}$$

where σ is the interfacial tension. Ma et al. (1997) derived their empirical scaling group, and hence β, by analysing and comparing the experimental data provided by Mattax and Kyte (1962), Hamon and Vidal (1986) and Zhang et al. (1996). The

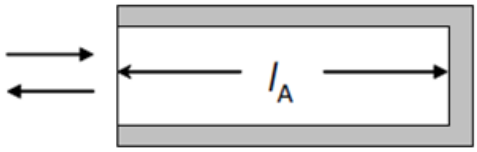

(a)

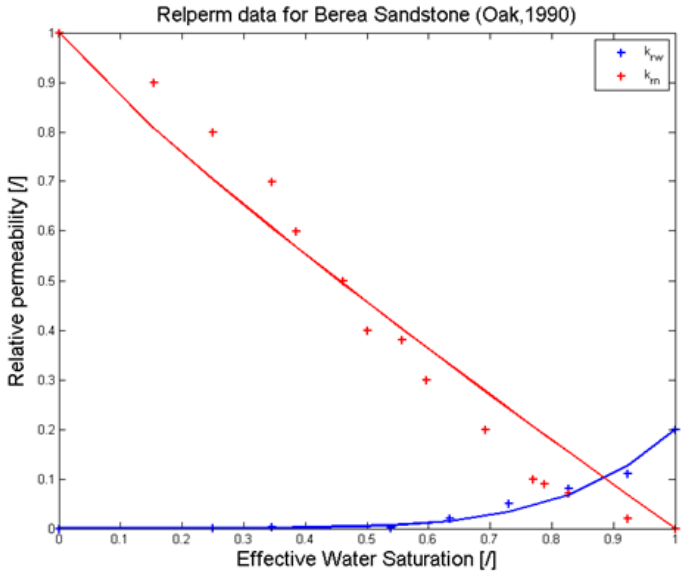

(b)

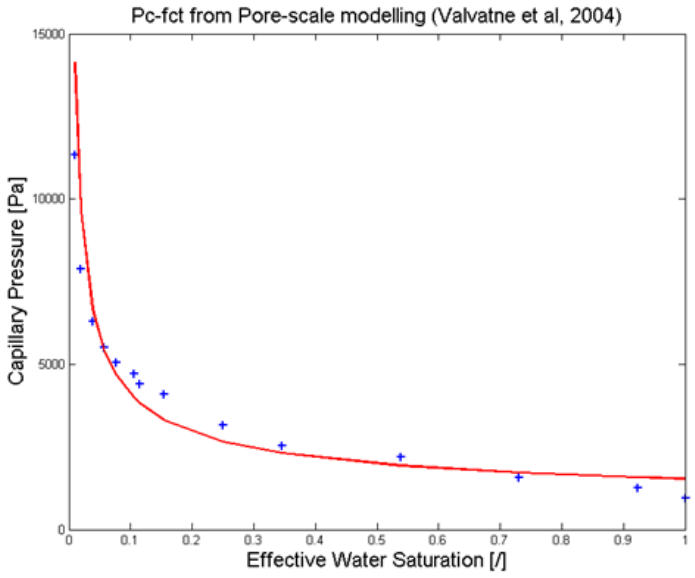

(c)

Figure 3.3: Spontaneous counter-current imbibition experiments on Berea sandstones. (a) Cores were epoxy sealed such that only one end was open for imbibition, grey area shows the seal (s. Tab 3.1 for core dimensions). The cores were saturated with Soltrol220 (Zhang et al., 1996) or air (Babadagli and Hatiboglu, 2007) as the non-wetting phase. They were placed horizontally when immersed into the wetting phase. The wetting phase was a synthetic reservoir brine or water, respectively. Relative permeability (b) and capillary pressure (c) curves for modelling imbibition were taken from Oak (1990) and Valvatne and Blunt (2004) for water-wet Berea core. Gravitational effects can be neglected in both experiments.

use of $\sqrt{\mu_w \mu_{nw}}$ is empirical and correlates well with recovery observed for oil-water systems, but fails to predict recovery in gas-water systems (Zhang et al., 1996). Later Zhou et al. (2002) suggested that the transfer rate not only depends on viscosities but rather on the phase mobilities and the total mobility of the system. They derived an empirical scaling group which, in addition to the group of Ma et al. (1997), depends on $\lambda^*_{r\alpha} = k^*_{r\alpha}/\mu_\alpha$, i.e. the characteristic mobility for the phases and the characteristic mobility ratio $M^* = \lambda^*_{rw}/\lambda^*_{rnw}$. For evaluation of λ^*_r and M^* the end-point relative permeabilities $k^*_{r\alpha}$ are used.

sample **BC13** (Zhang et al., 1996)			
L_c $[cm]$	4.998	μ_w $[Pa \cdot s]$	9.67×10^{-4}
K $[mD]$	503.6	μ_o $[Pa \cdot s]$	0.03782
ϕ $[/]$	0.209	ρ_w $[g/cm^3]$	1.012
σ $[mN/m]$	47.38	ρ_o $[g/cm^3]$	0.848
S_{wmi} $[/]$	0.0	S_{or} $[/]$	0.45
sample **17** (Babadagli and Hatiboglu, 2007)			
L_c $[cm]$	10.16	μ_w $[Pa \cdot s]$	0.001
K $[mD]$	500.0	μ_g $[Pa \cdot s]$	1.80×10^{-4}
ϕ $[/]$	0.21	ρ_w $[g/cm^3]$	1.0
σ $[mN/m]$	72.9	ρ_g $[g/cm^3]$	0.001
S_{wmi} $[/]$	0.0	S_{gr} $[/]$	0.37

Table 3.1: Overview of the parameters used to simulate the one dimensional counter-current imbibition experiments of Zhang et al. (1996) and Babadagli and Hatiboglu (2007), respectively.

Fig. 3.4 compares the relative recovery R/R_∞ of one dimensional DP simulations with the actual experimental data. The fracture was constantly filled with water, i.e. water saturation in the fracture cell was always held at $S_{wf} = 1$.

Simulations using β_{Ma} capture the early time behaviour in the first brine-oil experiment of Zhang et al. (1996) well. This is not surprising because this particular experiment was used when Ma et al. (1997) derived β_{Ma} empirically. On the other hand, β_{Ma} over-predicts the late time behaviour. It completely fails to predict the recovery in the water-air system in the second experiment of Babadagli and Hatiboglu (2007). In comparison to the laboratory results, the simulation

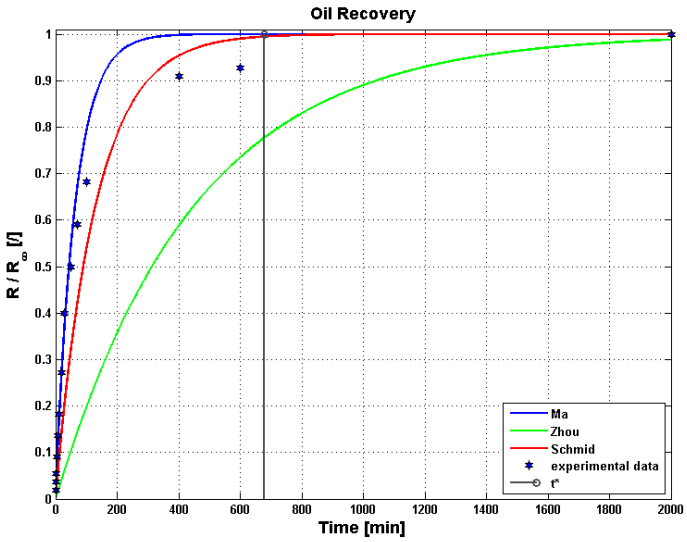

(a)

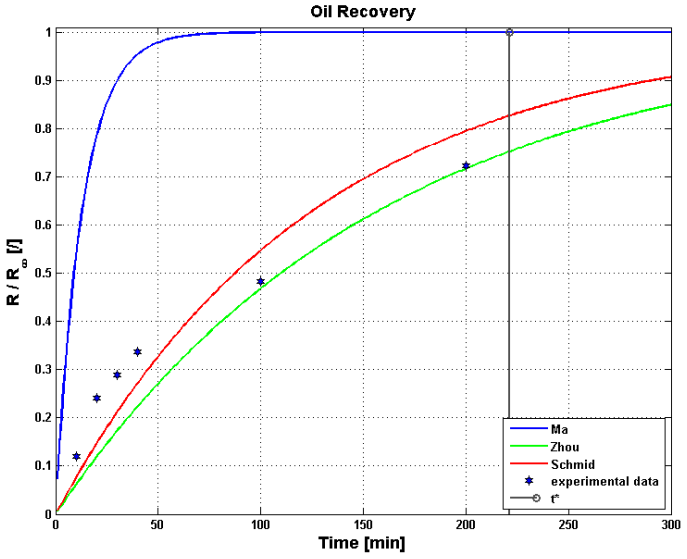

(b)

Figure 3.4: Simulation of counter-current imbibition using different transfer rate formulations and comparing with experimental results ($\star$) observed in the lab. Blue is the predicted relative hydrocarbon recovery using the Ma coefficient (Eq. 3.32), red denotes to the here presented β^{SI} (Eq. 3.12) and green is the recovery by using the Zhou transfer rate equation (Eq. 3.33). (a) Brine-oil system. Experimental data from the BC13 sample in Zhang et al. (1996). (b) Water-gas system. Spontaneous counter-current imbibition with core 17 published in Babadagli and Hatiboglu (2007). t* indicates the time until the analytical solution for spontaneous imbibition is valid (Eq. 3.13).

with β_{Ma} over-predicts the recovery by more than 60% at early time.

The simulations using β_{Zhou} under-predict the recovery in the brine-oil system. Hence β_{Zhou} is not suitable for this set of rock and fluid properties. In contrast to simulations with β_{Ma}, simulations with β_{Zhou} are able to model the late-time behaviour of the water-gas experiment more accurately because here the importance of the gas mobility dominates.

Conversely, simulations using the universal transfer rate coefficient β^{SI} of Schmid and Geiger (2012, 2013) show very good agreement with data of both experiments. This implies that once one has established the rock and fluid properties for the matrix blocks, either using Special Core Analysis (SCAL) or pore-network modelling, the transfer rate coefficient of Schmid and Geiger (2012, 2013) always yields the correct transfer rates for spontaneous counter-current imbibition and hence transfer function T^{SI} (Eq. 3.15), regardless of the fluid-rock system. In other words, with the new β_{SI} there is no longer the risk that the wrong transfer rate coefficient could be chosen for the given fluid and rock properties as this would result in predictions of fracture-matrix fluid transfer that can be orders of magnitude off.

3.5.2 *Gravity Drainage*

The gravity drainage transfer function T^{GD} (Eq. 3.27) is validated by simulating fracture-matrix transfer in a 1m long vertical oriented core. The core comprises a strongly water-wet artificial consolidated porous media. It was epoxy sealed but the top and bottom of the core were left open for injection and production (Fig. 3.5 (a)). Table 3.2 gives the rock and fluid properties used in the experiment. The core was initially saturated with CO_2 and subsequently flooded with brine. Afterwards, oil was injected until the brine reached its residual saturation S_{im}, which remained immobile during the later oil drainage. Finally, oil was drained due to gravity forces by injected air at the top. The relative permeability curves and the capillary pressure curve were calculated using data obtained from gamma-ray measurements (Pedrera et al., 2002). Fig. 3.5 (b) and Fig. 3.5 (c)

show fitted Brooks-Corey models for the oil relative permeability and the capillary pressure. These relative permeability and capillary pressure models were used for the calculation of the transfer rate coefficient β^{GD} (Eq. 3.25) when simulating oil drainage with the DP approach.

$L\ [cm]$	100	$\mu_o\ [Pa \cdot s]$	11.3×10^{-3}
$K\ [D]$	7.0	$\mu_g\ [Pa \cdot s]$	0.018×10^{-3}
$\phi\ [-]$	0.41	$\rho_o\ [kg/m^3]$	831
$\sigma\ [mN/m]$	21.5	$\rho_g\ [kg/m^3]$	1.29
$S_{wc}\ [/]$	0.21	$S_{or}\ [/]$	0.12

Table 3.2: Overview of the parameters used to simulate the gravity drainage process (Pedrera et al., 2002).

Fig. 5.10 compares the oil recovery from the DP simulations using T^{GD} (Eq. 3.27) with the experimental data. Excellent agreement is observed between the simulated recovery and the experimental results at both, early and late time, without requiring of tuning any parameters. This is a strong indication that the gravity drainage transfer function (Eq. 3.27) is well suited to simulate gravity-driven fluid exchange between flowing (fractures) and the stagnant (matrix) domain as long the assumptions of incompressible gas and neglected capillary forces remain valid.

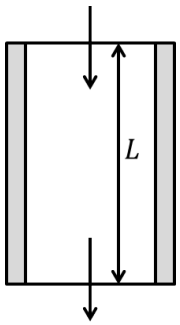

(a)

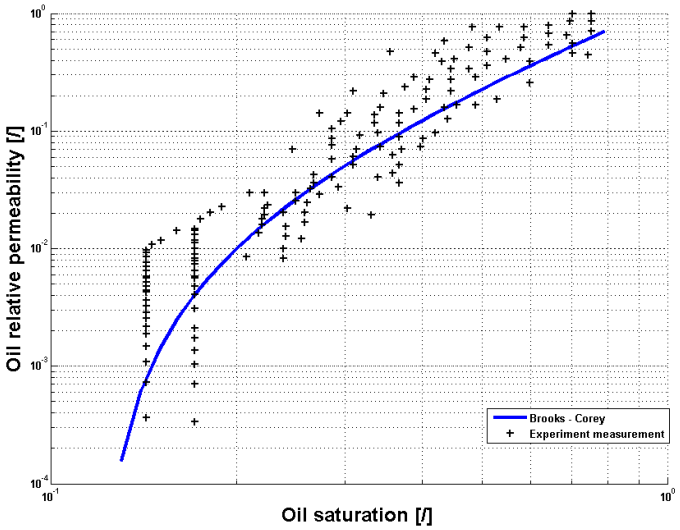

(b)

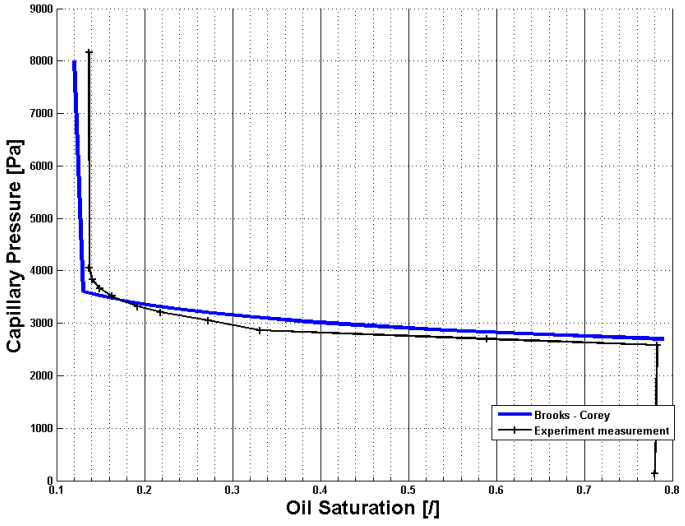

(c)

Figure 3.5: Gravity drainage experiment. The core comprising artificially consolidated porous media was placed vertically and saturated first by brine and afterwards by oil. The inlet at top and the outlet at bottom were opened for gravity drainage, grey area indicates the seal (s. Tab 3.2 for core dimensions) (a). Relative permeabilities (b) and capillary pressure (c) data (black stars) were measured during the experiment. These data were fitted using the Brooks-Corey model (blue line) to calculate the transfer rate coefficient for gravity drainage β^{GD}.

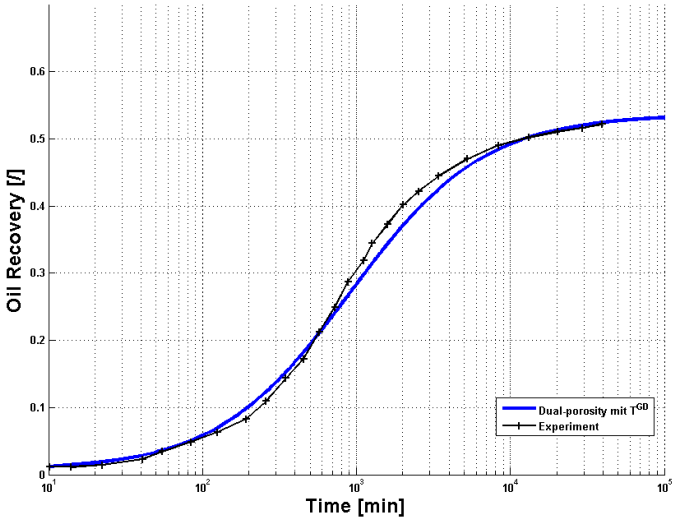

Figure 3.6: Comparison of a DP simulation for a gravity drainage process (blue) using the gravity transfer function T_k^{GD} with recovery curves obtained experimentally (black). Note that the gravity-dominated DP model does not require fitting or tuning parameters (Table 3.2).

3.6 MATRIX - FRACTURES SHAPE FACTORS

Another crucial parameter to quantify fracture matrix fluid exchange is the shape factor σ. The analytical solution for spontaneous imbibition described earlier was derived for one dimensional displacement where the shape factor corresponds to the inverse squared characteristic length of a matrix block $\sigma = L_c^{-2}$, i.e. the distance between inlet of the matrix block and the nearest no-flow boundary. If one side of a uniform matrix block is open to imbibition, L_c is the length of the matrix block. If two opposite ends of a uniform matrix block are open to imbibition, L_c is half the length of a matrix block as the imbibition fronts meet in the centre of the matrix block. In reality, however, it is more common that all faces of the matrix block are surrounded by fractures filled with a wetting fluid and thus imbibition can occur over all sides of the block. This leads to a quasi-radial propagation of the imbibition front in the matrix block rather than one-dimensional, piston-like displacement. To capture this multi-dimensional behaviour, many shape factors were introduced in the literature (Warren and Root, 1963; Kazemi et al., 1976; Coats, 1989; Lim and Aziz, 1995; Ma et al., 1999). To analyse how different shape factors affect the non-wetting fluid recovery for 3D matrix block with the transfer function T^{SI}, different fine-grid simulations

of spontaneous counter-current imbibition are presented here for the following conditions:

- one side of the matrix is open for imbibition (one-end-open, OEO),
- two opposite sides of the matrix are open for imbibition (two-ends-open, TEO),
- all faces of the matrix block are open for imbibition (all-faces-open, AFO).

Note that the gravity drainage process is a one-dimensional vertical displacement process and thus the characteristic length for transfer function T^{GD} is always the height of the matrix block L. No sensitivity analysis of the shape factors is necessary here.

The fine-grid single-porosity simulations solving the diffusion equation (Eq. 3.5) were performed using two different simulators, a commercially available reservoir simulator (FD simulator) and the research grade C++ simulation platform Complex Systems Modelling Platform (CSMP++) (Matthai et al., 2007). The former uses a finite difference discretization on structured grids for simulating two phase flow. To ensure that only the diffusion part of two-phase flow is considered, the gravity constant GRAVCONS was set to zero (see A.3). CSMP++ employs a finite element method on tetrahedral unstructured grids and solves the diffusion equation directly. For a better comparison of the fine-grid simulations results, grids with approximately $1,000,000$ elements were employed in both simulators. The fluid and matrix properties used for the simulations are listed in Table 3.3. The wetting fluid is assumed to be water and the non-wetting fluid is assumed to be oil. Fig. 3.7 shows the relative permeability and capillary pressure curves for a water-wet Berea sandstone core used for the simulation. The matrix block dimensions are $10 \times 10 \times 10$ metres. The fractures surrounding the matrix block are assumed to be constantly filled with water i.e. $S_{wf} = 1.0 - S_{nwr}$ during the entire simulation. This scenario corresponds to instantaneously filled fractures.

matrix permeability	K_m	10.0 mD
matrix porosity	ϕ_m	0.2
viscosity wetting	μ_w	5.0×10^{-4} $Pa \cdot s$
viscosity non-wetting	μ_{nw}	5.0×10^{-3} $Pa \cdot s$
interfacial tension	ITF	35.0 mN/m
initial saturation wetting	S_{wmc}	0.4
residual non-wetting	S_{nwr}	0.422

Table 3.3: Properties used in the counter-current imbibition simulations, taken from Behbahani et al. (2006).

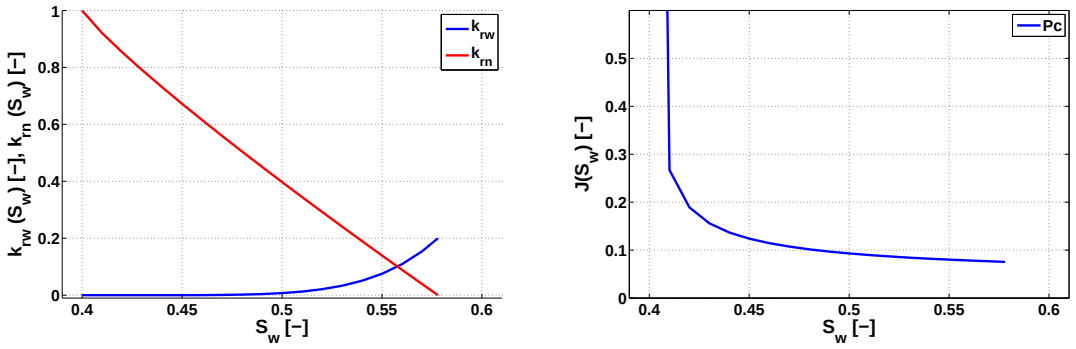

(a) (b)

Figure 3.7: Relative permeability curves for a Berea sandstone (Oak, 1990) (a) and pore network predicted dimensionless J-function (capillary pressure) from Valvatne and Blunt (2004) (b) used in the imbibition simulations.

3.6.1 *One-Dimensional Fluid Exchange Between Fractures and Rock Matrix (OEO and TEO case)*

First, the simulated water front propagation is compared in the rock matrix with the analytical solution. In contrast to laboratory experiments on cores, where some uncertainty in the measurements of data is omnipresent, the fine-grid simulators solve the diffusion equation with the same input data as for the analytical solution. Thus, for one dimensional flow, the fine-grid simulations should match the profiles until the no-flow boundary is reached. One dimensional flow is given if one side or two opposite sides of a matrix block are exposed to the wetting fluid while all remaining faces of the matrix block are sealed. In these cases, L_c is the length of the matrix block, i.e. $L_c = 10\ m$, respectively $L_c = 5\ m$ if two opposite ends are open. Figure 3.8 shows the profiles of the wetting fluid saturation for different times. Both fine-grid simulations match the analytical solution well. We note that the FD simulator predicts a slightly faster advance of

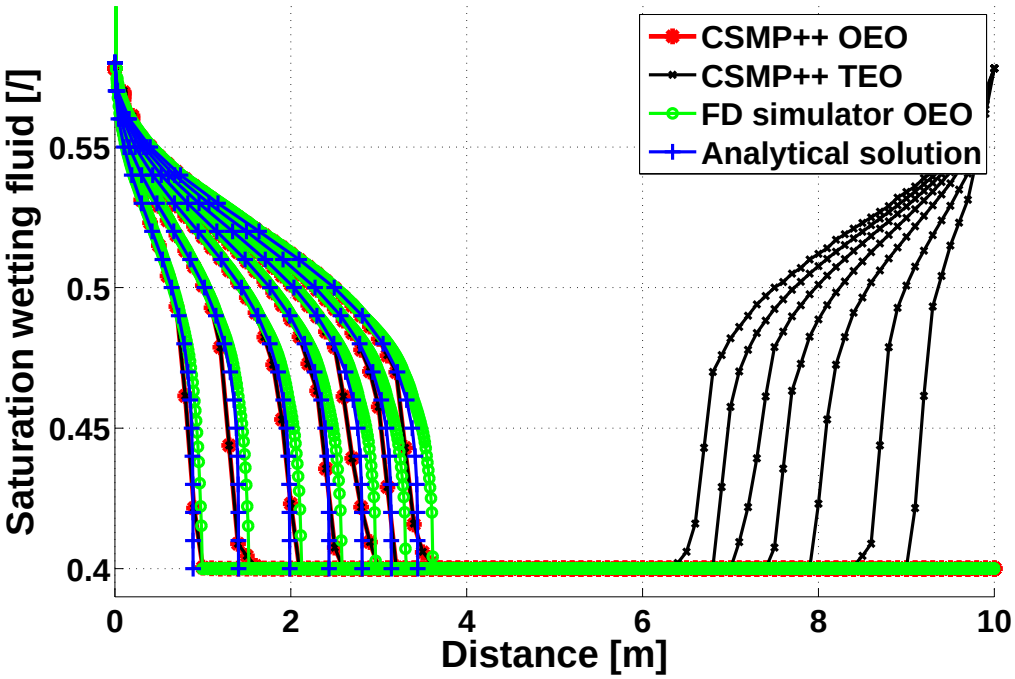

Figure 3.8: Imbibition fronts at different times for the one-dimensional flow experiment. Profiles obtained with CSMP++ for the one-end-open (OEO) case (red) and two-ends-open (TEO) case (black) match the position of the analytically computed front (blue) well. The position of fluid fronts obtained with the FD simulator (green) progress slightly faster at later times, but still agree well with the analytical solution.

the saturation fronts but still agrees well with the analytical solution.

Figure 3.9 shows the oil recovery as a function of dimensionless time $t_D = t\gamma\beta$. The results from fine-grid simulations match that of the analytical solution. In contrast, using the exponential DP model $\frac{R}{R_\infty} = 1 - e^{-\gamma\beta t}$ (Eq. 3.14) in conjunction with the universal transfer rate coefficient β (Eq. 3.12), causes poor agreement in the early time behaviour. However, recovery is matched at late time. This difference is due to initially steep saturation gradients within the matrix block, which leads to a recovery rate decline proportional to $1/\sqrt{t}$ at early time (Patzek et al., 2013). Later, after a so-called interference time, the recovery decays exponentially such that the Aronofsky formulation (Eq. 3.14) yields good agreement of recovery curves at late time. A possible remedy to describe the recovery for the entire imbibition process, would be a transfer function which uses second derivatives of the capillary potential to keep higher order terms as done by Zimmerman et al. (1996).

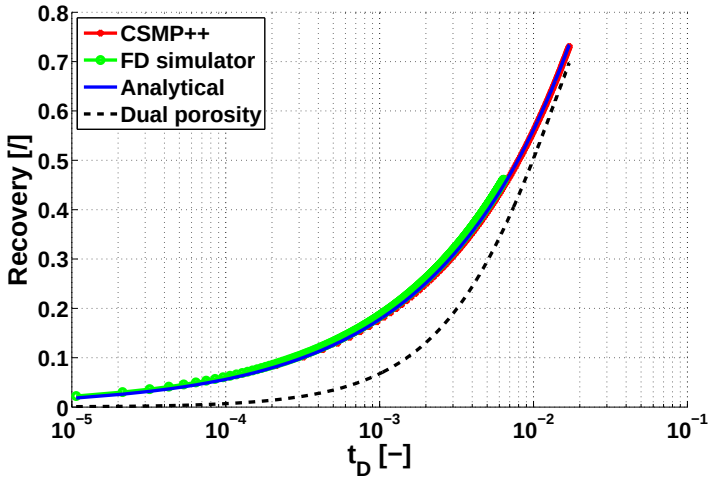

Figure 3.9: Oil recovery against dimensionless time for TEO experiment. The recovery obtained with CSMP++ (red) and the FD simulator (green) matches the analytical solution (blue). The DP approach (dashed) under-predicts the recovery at early time, but agrees with the analytical solution at late time.

3.6.2 *Three-Dimensional Fluid Exchange Between Fractures and Rock Matrix*

As mentioned earlier, the analytical solution is derived for one dimensional flow. However, in nature, the imbibition of a wetting fluid into the rock matrix will be three-dimensional, which must be modelled by the appropriate choice of a shape factor. This is the AFO case. One of the first shape factors for simulating fracture-matrix exchange in 3D was introduced by Kazemi et al. (1976) as

$$\sigma = L_c^{-2} = 4\left(\frac{1}{L_x^2} + \frac{1}{L_y^2} + \frac{1}{L_z^2}\right), \tag{3.34}$$

where L_i is the side length of the matrix block in i_{th} direction. In our case, we have $L_x = L_y = L_z = 10\ m$. This shape factor assumes a linear pressure gradient between the fractures and the matrix block centre, that is the shape factor depends only on the matrix geometry but the pressure gradient in the matrix block is not accounted for. This is analogous to the first order DP model (Eq. 3.15) where a linear saturation gradient is assumed. Later Kazemi et al. (1992) extended their formulation to

$$\sigma = L_c^{-2} = \pi^2\left(\frac{1}{L_x^2} + \frac{1}{L_y^2} + \frac{1}{L_z^2}\right), \tag{3.35}$$

which describes a pseudo-steady state pressure gradient in the matrix block. The same expression was independently derived for the case of isotropic matrix permeability by Lim and Aziz (1995), who also developed a shape factor using a cylindrical approximation of a matrix cube ($L_x = L_y = L_z = L$) to approximate the shape factor as

$$\sigma = L_c^{-2} = \frac{25.67}{L^2}. \tag{3.36}$$

Similar shape factors for uniform matrix cubes were derived by Coats (1989) as

$$\sigma = L_c^{-2} = \frac{24.0}{L^2} \tag{3.37}$$

and Thomas et al. (1983) as

$$\sigma = L_c^{-2} = \frac{25.0}{L^2}. \tag{3.38}$$

Note that Thomas et al. (1983) assumed a mobility ratio of approximately 1 in their derivation. Fig. 3.10 shows recovery profiles from 3D simulations of spontaneous imbibition for AFO. It compares the fine-grid simulation result to the predicted non-wetting fluid recovery using the transfer function with the different shape factors discussed in Eqs.(3.34), (3.35) and (3.36). Recall that the FD simulator predicted a slightly faster advance of the water front compared to the unstructured grid simulations (Fig. 3.8). The consequences are now more pronounced in 3D as there is a noticeable difference in predicted recovery at early time. The vertical line in Fig. 3.10 represents time t^* (Eq. 3.13) until which the analytical solution is valid. The recovery predicted by the exponential DP approach (Eq. 3.14) agrees well with the analytical solution until $t = t^*$ but also models the late time behaviour well. We observe that the analytical solution and the dual porosity model using Kazemi's original shape factor (Eq. 3.34) under-predict the recovery at all times. This difference is because of the assumption of a linear saturation gradient between the fracture and the matrix block centre, which artificially enlarges the volume of the matrix block and slows down the recovery. Better results, especially at early time, are obtained with the shape factors of Kazemi and Gilman (1993) and Lim and Aziz (1995) (Eqs. 3.35 and 3.36). In these cases, the analytical solution yields a perfect match with the single

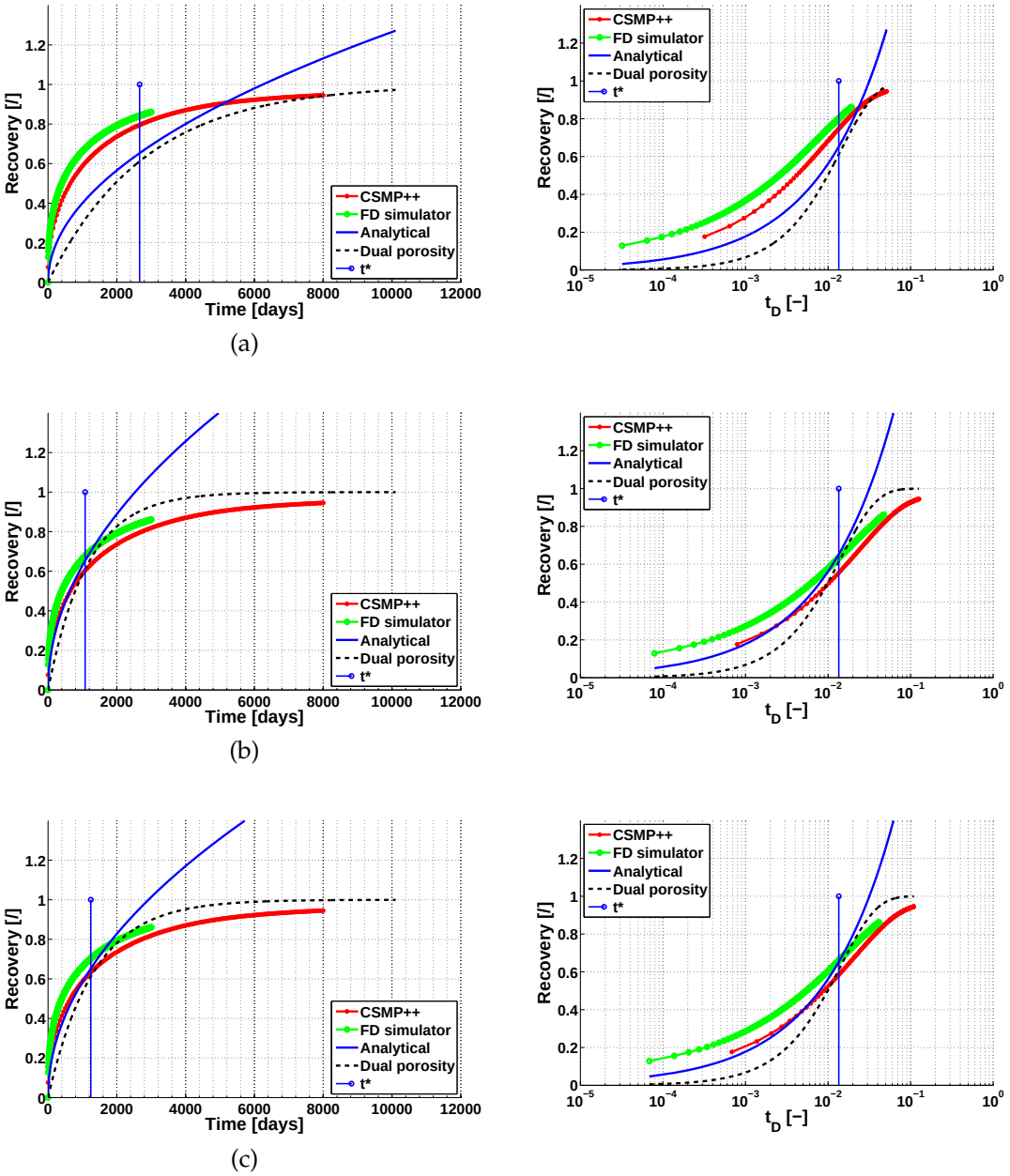

Figure 3.10: Non-wetting fluid recovery as a function of time (left) and dimensionless time (right) varying the shape factor σ for transfer rate coefficient computation. (a) σ after Kazemi et al. (1976), (b) σ after Kazemi and Gilman (1993) and (c) σ after Lim and Aziz (1995).

porosity simulations of CSMP++ at early time. The dual porosity simulations slightly under-predict recovery at early times and slightly over-predict the late time behaviour, but still give a reasonable approximation of the overall recovery.

3.7 SUMMARY

In this chapter, the general DP approach was presented. It models fluid exchange between fractures and matrix due to capillary and gravity forces using analytically derived transfer functions:

The transfer function for spontaneous counter-current imbibition, T^{SI} is based on the first analytical solution of spontaneous imbibition (Eq. 3.15).

The transfer function for gravity drainage, T^{GD} is based on the Buckley-Leverett solution for downward displacement of the non-wetting fluid in a column (Eq. 3.27).

Both transfer functions matched the laboratory experiments well and are sufficient for predicting one dimensional flow between fracture and matrix block. While the gravitational drainage process is always one dimensional, it is a vertical displacement from top to bottom, spontaneous counter-current imbibition process, usually is a three dimensional process. Typically all faces of a matrix block, surrounded by fractures, are in contact with the wetting fluid. This three dimensional displacement was modelled using different shape factors. The impact of these shape factors was analysed by comparing DP simulations with high-resolution Finite Difference Method (FDM) and Finite Element Method (FEM) simulations. These results showed that pseudo steady-state shape factors, which account for the quasi radial propagation of the saturation fronts due to the saturation gradients, are more suitable to predict the three-dimensional fracture-matrix mass transfer, especially at early time. Another approach to model the three dimensional spontaneous imbibition could be a derivation of the analytical solution for spontaneous imbibition (Section 3.2) in radial coordinates using the distance between the fracture-matrix exchange area and the centre of the matrix volume as the characteristic length. To what extend a transfer function

based on such analytical solution would model recovery from different matrix block shapes appropriately, is subject to future work.

4

MULTI-RATE DUAL-POROSITY MODELLING

4.1 INTRODUCTION

The classical Dual-Porosity (DP) approach introduced in the previous chapter (Ch. 3) assumes uniform rock and fluid properties (i.e. permeability, porosity, wettability) and uniform fracture spacing within one simulation grid cell. The rock matrix in the conventional DP model is hence often idealised as a series of sugar cubes (Fig. 4.1 b). Fluid exchange between fractures and matrix is described by one single transfer function T using properties, which are averaged over the grid cell. Therefore, the DP models are also called Single-Rate Dual-Porosity (SRDP) models. In the groundwater community SRDP models for vadose zone areas are referred to as mobile-immobile or multi-porosity models (Šimůnek et al., 2003; Gerke, 2006). However, considering that simulation grid cells are usually large, of the order of $100 \times 100 \times 10$ m, the matrix block sizes and the rock properties may vary significantly within one simulation grid block. For Single-Porosity (SP) models, the rock properties are upscaled to obtain average porosity and permeability values (Christie, 1996; Budd and Vacher, 2004). However, in DP models large (or less permeable) matrix blocks release oil at significantly slower rates compared to smaller (or more permeable) matrix blocks. This can lead to order of magnitude variations of transfer rates in a single grid cell. Neglecting this matrix heterogeneity by using a single average transfer function as discussed in Chpater 3, inevitably leads to a loss of information. It does not allow to capture the multi-rate behaviour of fracture-matrix transfer in fractured porous media that emerge if the matrix is heterogeneous. Accounting for heterogeneity of the rock matrix below the scale of a reservoir simulation grid

cell therefore, aims to represent fractured geological formations more realistically.

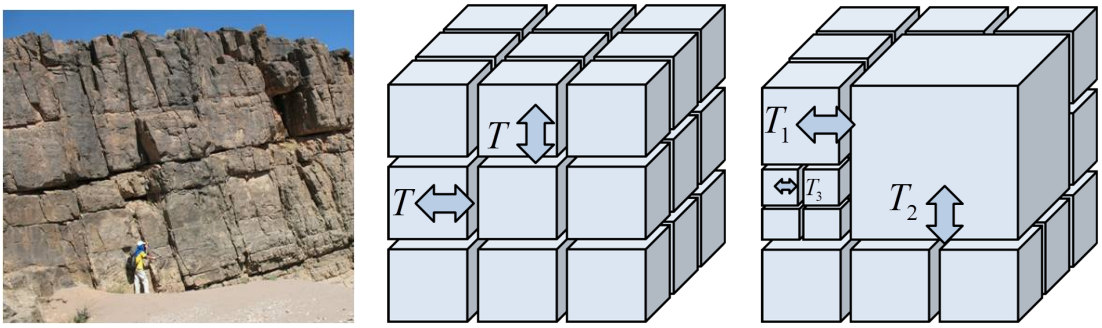

Figure 4.1: (a): Fractured carbonate formation in Morocco with different matrix block sizes (Image courtesy of Herman Boro, SGS Horizon). (b): Conceptual representation of fractured porous media represented by the standard SRDP model and a single transfer function. (c): More realistic MRDP model where multiple transfer functions, representing for example different shape factors, can be present in a single grid block.

A straight forward solution to solve this problem is to use an approach, which models the multiple rates of fluid exchange within one grid cell. This is the so-called Multi-Rate Dual-Porosity (MRDP) approach. Haggerty and Gorelick (1995) pioneered the MRDP model by developing a Multiple Rate Mass Transfer (MRMT) model for single-phase solute transport with mobile and immobile domains. The MRMT model uses a distribution of transfer rates between the mobile and immobile domain. The advantage of the MRMT model was demonstrated by modelling tracer tests in fractured dolomite formations. Haggerty et al. (2001) demonstrated that different transfer rates between the mobile fractures and immobile matrix often cannot be averaged in a straightforward manner and predicted breakthrough curves can differ by orders of magnitude for observed areas if only single rate is assumed (see Fig. 1.10). More recently, the concept of the MRMT model was introduced in the petroleum literature for multi-phase flow simulations (Di Donato et al., 2007). Using streamline simulations, Di Donato et al. (2007) showed that fundamentally different recovery predictions are obtained if more than one transfer function is used in a single simulation grid block (Fig. 4.2).

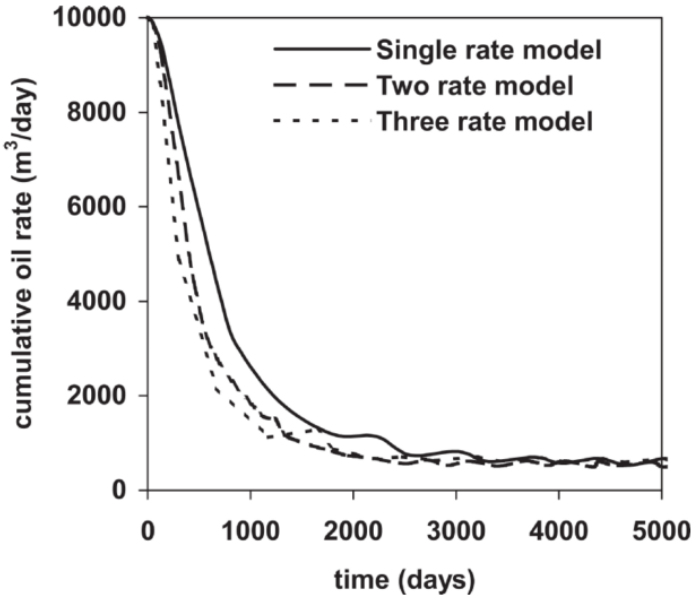

Figure 4.2: Cumulative oil rate predictions from imbibition simulations of the Liu7 oil field (China) using Single-Rate Dual-Porosity (SRDP) model and Multi-Rate Dual-Porosity (MRDP) model with $N = 2$ and $N = 3$ (Di Donato et al., 2007). Significantly different oil recoveries are obtained when employing more than one transfer function.

In this chapter, the numerical formulation of the MRDP model is introduced as proposed by the Di Donato et al. (2007). The multi-rate transfer function is based on the transfer functions presented in Chapter 3. Then the effect of including small-scale geological information is analysed on the overall recovery of the non-wetting fluid. The results of the standard SRDP approach are compared with fine-grid simulations and the MRDP model considering multiple scenarios where fracture spacing and matrix permeabilities differ.

4.2 MULTI-RATE DUAL-POROSITY TRANSFER FUNCTION

To capture the additional small-scale matrix heterogeneities, each simulation grid cell Ω is assumed to be composed of N rock matrix sub-domains Ω_k, each with its own set of parameters (Fig. 4.1c) as

$$\Omega = \bigcup \Omega_k \quad k = 1 \cdots N. \tag{4.1}$$

For the k_{th} sub-domain Ω_k, these are the matrix permeability K_{mk}, the matrix porosity ϕ_{mk}, the wettability defined by the relative permeabilities k_{rwk}, k_{rnwk}

and capillary prerssure P_{ck} curves, and the characteristic length L_{ck} of the rock matrix blocks. I reiterate that the rock matrix is assumed to be occupied by two immiscible and incompressible fluid phases, the wetting (S_{wm}) and the non-wetting phase (S_{nwm}). However, modelling the presence of a third phase is possible under the assumption that this fluid is immobile at all times such that $1.0 = S_{wm} + S_{nwm} + S_{im}$ with $S_{im} = const.$

Di Donato et al. (2007) defined the matrix sub-domain porosities correlating the pore volume of the sub-domain Ω_k to the overall bulk volume of the simulation grid cell Ω_b as

$$\phi_m^k = \frac{\Omega_k}{\Omega_b} \quad k = 1 \cdots N. \tag{4.2}$$

However, for the application of the transfer function based on the analytical solution for spontaneous imbibition T^{SI} (Eq. 3.15) actual porosities of the rock matrix are needed. Hence, the porosities of each rock matrix sub-domain are defined in the conventional way as

$$\phi_{mk} = \frac{\Omega_k}{\Omega_{bk}} \quad k = 1 \cdots N, \tag{4.3}$$

where Ω_{bk} is the bulk volume of the rock matrix sub-domain. They sum up to the overall matrix porosity in the simulation grid block as

$$\phi_m = \frac{\sum_{k=1}^{N} \Omega_k}{\Omega_b} = \frac{\sum_{k=1}^{N} \phi_{mk} \Omega_{bk}}{\Omega_b}. \tag{4.4}$$

The wetting phase saturation of the rock matrix in the simulation grid block is then defined as

$$\phi_m S_{wm} = \sum_{k=1}^{N} \frac{\phi_{mk} \Omega_{bk} S_{wmk}}{\Omega_b}, \tag{4.5}$$

and the multi-rate transfer function is consequently

$$T = \phi_m \frac{\partial S_{wm}}{\partial t} = \sum_{k=1}^{N} \frac{\phi_{mk} \Omega_{bk}}{\Omega_b} \frac{\partial S_{wmk}}{\partial t} = \sum_{k=1}^{N} T_k. \tag{4.6}$$

The fluid transfer from matrix sub-domains to adjacent fractures is modelled individually through the corresponding transfer function $T_k,\ k = 1 \dots N$ which can model either capillary driven fluid exchange (Eq. 3.15)

$$T_k = \frac{\Omega_{bk}}{\Omega_b} T_k^{SI} = \frac{\Omega_{bk}}{\Omega_b} \gamma_k \beta_k^{SI} \phi_{mk} \left(S_{wk}^* - S_{wmk} \right), \tag{4.7}$$

or gravity driven drainage of the non-wetting fluid (Eq. 3.27)

$$T_k = \frac{\Omega_{bk}}{\Omega_b} T_k^{GD} = \frac{\Omega_{bk}}{\Omega_b} \frac{\beta_k^{GD} \phi_{mk}}{a_k - 1} \left(S_{nwk}^* - S_{nwmk} \right)^{a_k}. \tag{4.8}$$

Here γ_k and a_k are fitting parameters (see Ch. 3) but it is noted that $\gamma_k \approx 70$ already provides an excellent value for a wide range of experiment data (Fig. 1.5). S_α^* is the maximum possible saturation of the wetting fluid phase $\alpha = w$

$$S_{wk}^* = \left(1.0 - S_{nwmr} - S_{im} \right), \tag{4.9}$$

or the non-wetting fluid $\alpha = nw$

$$S_{nwk}^* = \left(1 - S_{im} \right) L - \int_0^L P_c^{-1} \left(\Delta \rho g h \right) dh, \tag{4.10}$$

where S_{nwmr} is the residual non-wetting phase saturation and S_{im} is the third immobile phase. L refers to the height of the matrix blocks, P_c is the capillary pressure, $\Delta\rho$ is the density gradient and g the gravitational acceleration.

Each transfer term T_k hence models the rate at which a matrix sub-region k releases the fluid, based on the properties (e.g. permeability, wettability, shape factor) present in that sub-region. That means rather than using one transfer function T with averaged properties, T is the sum of the N transfer functions T_k (Di Donato et al., 2007).

The update of the saturations in the fracture domain at time step $n+1$ for the fracture cell j can now be computed as

$$S_{fj}^{n+1} = S_{fj}^{n+1,int} - \sum_{k=1}^{N} \frac{\phi_{mk} \Omega_{bk}}{\phi_f \Omega_b} \left(S_{mkj}^{n+1} - S_{mkj}^{n} \right), \tag{4.11}$$

where $S_{fj}^{n+1,int}$ is the interim fracture saturation after the advection computation in the fracture domain and ϕ_f is the fracture porosity. S_{mkj}^{n} refers to the previous rock matrix saturation of the sub-domain k in the virtual matrix cell j at time step n and the S_{mkj}^{n+1} is the new saturation at time $n+1$ calculated as

$$S_{mkj}^{n+1} = S_{wmkj}^{n+1} = S_{wkj}^{*} - \left(S_{wkj}^{*} - S_{wmkj}^{n}\right) e^{-\gamma_k \beta_k^{SI} \Delta t}, \tag{4.12}$$

applying the transfer function T_k^{SI} (Eq. 3.15), or in case of gravity driven fluid exchange using T_k^{GD} (Eq. 3.27)

$$S_{mkj}^{n+1} = S_{nwmkj}^{n+1} = S_{nwkj}^{*} - \left(\left(S_{nwkj}^{*} - S_{nwmkj}^{n}\right)^{1-a_k} + \beta_k^{GD} \Delta t\right)^{-\frac{1}{a_k - 1}}. \tag{4.13}$$

β_k^{SI} and β_k^{GD} are the transfer rate coefficients for spontaneous imbibition (Eq. 3.12) and gravitational drainage (Eq. 3.25), respectively.

To be consistent with mass balance, only as much fluid can enter the matrix domain as initially available in the fracture domain, the fluid in the fracture domain must be equally distributed between the N matrix sub-domains. To this end, the total amount of fluid that is taken up by the matrix sub-domains are calculated as

$$\Delta S_{mjT} = \frac{1}{\phi_f} \sum_{k=1}^{N} \frac{\phi_{mk} \Omega_{bk}}{\Omega_b} \left(S_{mkj}^{n+1} - S_{mkj}^{n}\right), \tag{4.14}$$

in order to obtain the fraction of required fluid volume in the matrix and present fluid volume in the fracture domain

$$F = \frac{\Delta S_{mjT}}{S_{fj}^{n+1,int}}, \tag{4.15}$$

for all cells where $S_{fj}^{n+1,int} \neq 0$. There is sufficient amount of fluid provided in the fracture domain when $F \leq 1$. Otherwise, when $F > 1$ the saturations in the rock matrix sub-domain are recalculated as follows:

$$S_{mkj}^{n+1} = S_{mkj}^{n} + \frac{\left(S_{mkj}^{n+1} - S_{mkj}^{n}\right)}{F}, \tag{4.16}$$

allocating equivalent portion of the available fluid to each sub-domain. The saturation in the fracture domain is now set to zero ($S_{fj}^{n+1} = 0$).

If $N = 1$, the model collapses to the standard SRDP approach. Assuming that the rock and fluid properties are not changing significantly over the lifetime of the field, the transfer rate coefficients β_k^{SI} and β_k^{GD} need to be computed only once in the beginning of the reservoir simulation. Those values are stored in the grid cells as additional parameters and allow us to update the matrix and fracture saturations using the respective transfer functions. In case the rock and fluid properties do greatly evolve over the lifetime of the reservoir due to, for example chemical processes that dissolve the rock matrix or change its wettability, the transfer rate coefficients must be recalculated with the new properties to maintain realistic predictions of fracture-matrix fluid exchange. Alteration of the rock and fluid properties usually does not occur abruptly such that a series of large time intervals can be chosen where the transfer rates are assumed to be constant. Therefore, the additional computational cost for the MRDP model mainly consists of the summation of the transfer functions T_k and the calculation of the saturation fraction F and is negligible for small N.

4.3 MULTI-RATE DUAL-POROSITY SIMULATIONS

In this section MRDP and SRDP simulations for six different matrix configurations are compared. The matrix is heterogeneous and this heterogeneity must be represented in a single grid cell in a dual-porosity simulation. To this end, the effect of heterogeneity in matrix block sizes and matrix permeabilities on recovery is studied. In the SRDP simulations, different means are used to average these heterogeneities. In the MRDP model, averaging is not necessary since, in contrast to SRDP model, each matrix sub-region has its own transfer function T_k (Eq. 4.7). The SRDP and MRDP results are compared to fine-grid simulations for validation purposes. The fine-grid simulations are performed solving the diffusion equation (Eq. 3.5) on different geometries (Fig. 4.3) using the Finite Element Method (FEM) of the Complex Systems Modelling Platform (CSMP++) suite. The

meshes for the fine-grid simulations consist of approximately 900.000 elements and 150.000 nodes.

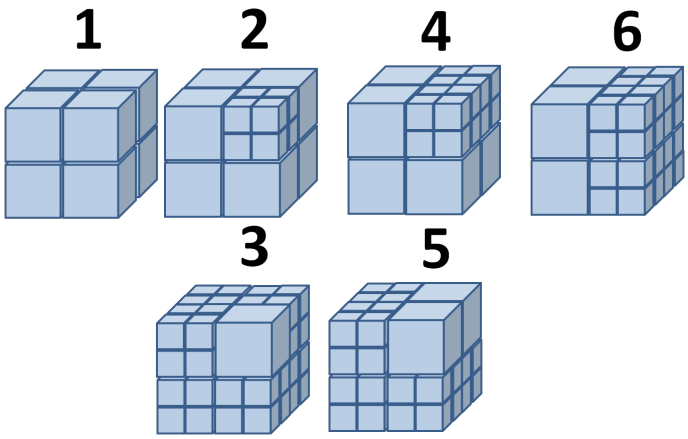

Figure 4.3: Different geometries of a $1m^3$ cube

4.3.1 *Different Matrix Block Size Distribution*

Figure 4.3 shows six different geometries of a $1m^3$ cube, which consists of two matrix block sizes with the side length of $l_1 = 0.5\ m$ and $l_2 = 0.25\ m$, respectively. For all but the first case, the volume of the cube is divided into two matrix sub domains $\Omega = \Omega_1 \cup \Omega_2$, where $\Omega_1 = \cup M_{l_1}$ contains all the blocks with side length l_1. $\Omega_2 = \cup M_{l_2}$ is composed of the smaller blocks. Case 1 has uniform matrix block sizes and the volume of the cubes is equally distributed between Ω_1 and Ω_2. For the characteristic length $L_c = 1/\sqrt{\sigma}$, $L_{c1} = 0.0919\ m$ is obtained for Ω_1 and $L_{c2} = 0.065\ m$ for Ω_2, respectively, when using the Kazemi and Gilman (1993) shape factor σ (Eq. 3.35). The averaged characteristic length L_c for the whole domain Ω is calculated using arithmetic, harmonic and geometric mean of L_{c1} and L_{c2}, weighted according to the volumes of Ω_1 and Ω_2 (Table 4.2). To demonstrate the effect of the matrix block size distribution only, the fluid and rock properties are assumed to be uniform (see Table 4.1 and Fig. 4.4 for more information).

I concentrate only on the spontaneous counter-current imbibition process and assume that all fractures are constantly filled with the wetting fluid $S_{wf} = 1.0 - S_{nwr} = 0.578$. In other words, there is no advection in the flowing domain and

matrix permeability	K_m	10.0 mD
matrix porosity	ϕ_m	0.2
viscosity wetting	μ_w	5.0×10^{-4} $Pa \cdot s$
viscosity non-wetting	μ_{nw}	5.0×10^{-3} $Pa \cdot s$
interfacial tension	ITF	35.0 mN/m
initial saturation wetting	S_{wmc}	0.4
residual non-wetting	S_{nwr}	0.422

Table 4.1: Properties used in the counter-current imbibition simulations, taken from Behbahani et al. (2006).

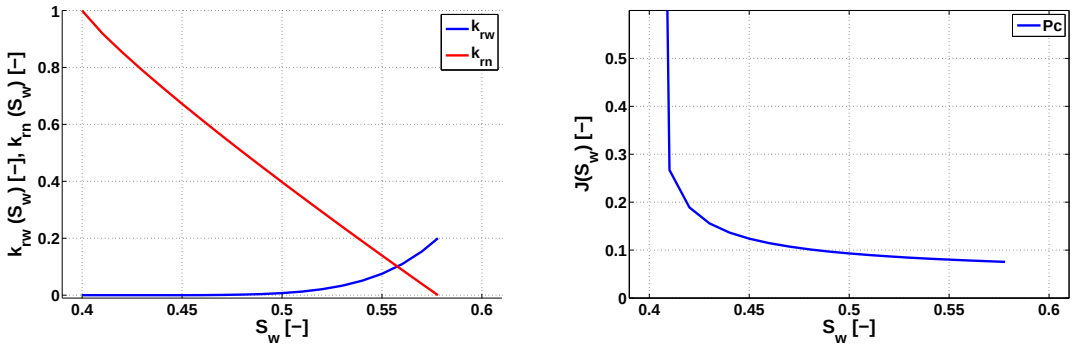

(a) (b)

Figure 4.4: Relative permeability curves for a Berea sandstone (Oak, 1990) (a) and pore network predicted dimensionless J-function (capillary pressure) from Valvatne and Blunt (2004) (b) used in the imbibition simulations.

gravitational forces are negligible due to the small height of the matrix blocks. The ratio of capillary and gravitational forces is $r < 1$ (Eq. 3.2). The transfer rate coefficients β_k^{SI} (Eq. 3.12) for the two sub-domains are then $\beta_{\Omega_1} = 5.12 \times 10^{-6}$ and $\beta_{\Omega_2} = 1.02 \times 10^{-5}$. The SRDP transfer rate coefficients $\beta_\Omega(L_c)$ using averaged characteristic lengths L_c for the six cases are given in Table 4.3. Case 1 consists of blocks of same size, thus one has $L_c = L_{c1} = L_{c2} = 0.0919$ m and consequentially $\beta_\Omega = \beta_{\Omega_1} = \beta_{\Omega_2} = 5.12 \times 10^{-6}$ sec^{-1}.

Figure 4.5 shows the SRDP and MRDP simulation results for all geometries, using the arithmetic mean to average the characteristic length L_c. The overall oil recovery accelerates when increasing the number of smaller matrix blocks because the fracture matrix surface area increases; fractures and matrix can exchange fluids more efficiently. Case 1 serves as a benchmark for the MRDP approach. Here the recovery curves coincide because one has $T_\Omega(\beta_\Omega) = T_{\Omega_1}(\beta_{\Omega_1}) + T_{\Omega_2}(\beta_{\Omega_2})$ for uniform matrix properties. In cases 2 to 6, the SRDP model predicts higher recov-

L_c $[m]$	1	2	3
arithmetic mean	0.0919	0.0775	0.0654
harmonic mean	0.0919	0.0753	0.0653
geometric mean	0.0919	0.0764	0.0654
L_c $[m]$	4	5	6
arithmetic mean	0.0723	0.0661	0.0680
harmonic mean	0.0706	0.0657	0.0672
geometric mean	0.0714	0.0659	0.0675

Table 4.2: Averaged characteristic lengths for the six models after Kazemi and Gilman (1993) weighted with the corresponding volumes of Ω_1 and Ω_2

β_Ω $[sec^{-1}]$	1	2	3
arithmetic mean	5.11×10^{-6}	7.19×10^{-6}	1.01×10^{-5}
harmonic mean	5.11×10^{-6}	7.62×10^{-6}	1.01×10^{-5}
geometric mean	5.11×10^{-6}	7.40×10^{-6}	1.01×10^{-5}
β_Ω $[sec^{-1}]$	4	5	6
arithmetic mean	8.26×10^{-6}	9.89×10^{-6}	9.34×10^{-6}
harmonic mean	8.67×10^{-6}	1.00×10^{-5}	9.57×10^{-6}
geometric mean	8.47×10^{-6}	9.95×10^{-6}	9.48×10^{-6}

Table 4.3: Averaged transfer rate coefficients β_Ω for the SRDP simulations using the averaged characteristic length L_c.

eries compared to the MRDP model. The difference between SRDP and MRDP simulations is quantified as

$$\Delta R = \left(R_{SR} - R_{MR}\right) / R_{MR}, \tag{4.17}$$

where R_{SR} is the recovery obtained with the SRDP simulations and R_{MR} the recovery predicted with the MRDP model. The largest difference is observed in cases 2, 4 and 6 where the smaller matrix blocks occupy less or the same volume as the bigger matrix blocks (Fig. 4.6). The smaller blocks release the non-wetting phase faster, but the amount of non-wetting fluid produced is limited by the volume $\Omega_2 < \Omega_1$. Through averaging, one assumes a sugar cube model with equidistant fracture spacing which is significantly smaller than the spacing of the dominant volume of Ω_1. In fact, the averaged characteristic length L_c is closer to L_{c2} than to L_{c1}. Hence, faster recovery is predicted with the conventional SRDP model. The difference in the SRDP and MRDP simulations is less if the mean L_c is closer to the characteristic length of the dominant matrix volume. This is the case in models 3 and 5, where $\Omega_2 > \Omega_1$ and $L_c \approx L_{c2}$. In general, using the arithmetic mean to average L_c yields results that are closest to the MRDP model, although the difference to the harmonic and geometric mean is not significant.

The three cases (2, 4 and 6) where the discrepancy between the SRDP and MRDP simulations is largest compared to the fine-grid single-porosity simulations show that the MRDP model yields significantly better predictions of the non-wetting fluid recovery (Fig. 4.7). The maximum relative error for MRDP simulations lies at 50% at intermediate time, in contrast to 75% using the SRDP approach and the arithmetic mean for L_c. Averaging L_c with the harmonic mean leads to an error above 80% for the SRDP model at intermediate time. As stated earlier in chapter 3, the pseudo-steady state shape factor (Eq. 3.35) yields better approximations of the early time behaviour where the relative error of the MRDP approach compared to fine-grid simulations is around 20%. Integrating the relative error over time and normalising with the error from the MRDP simulations shows that the error of the SRDP models, independently from the choice of the averaging process (arithmetic, harmonic or geometric mean), is around 25% higher than the error from the MRDP model (Fig. 4.8). To reduce the er-

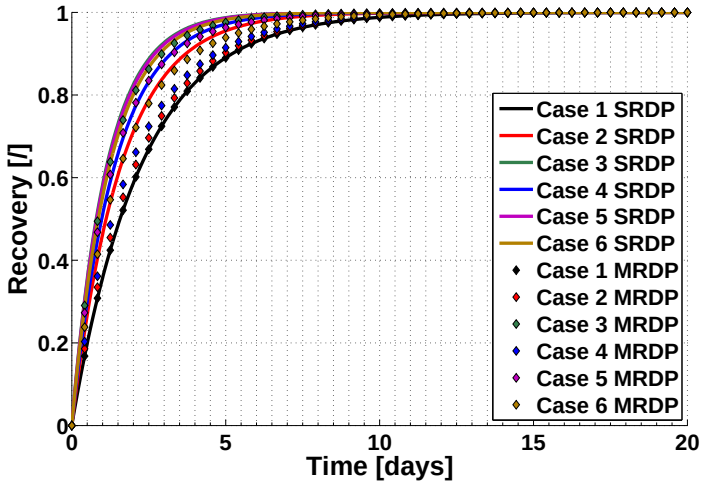

(a)

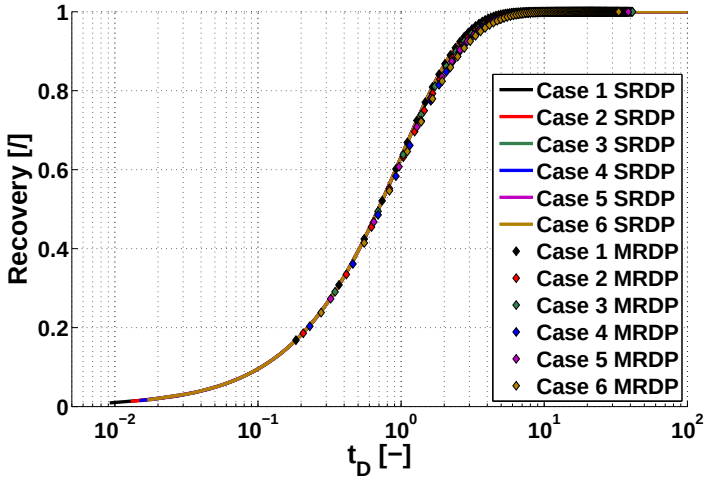

(b)

Figure 4.5: Normalized non-wetting fluid recovery obtained with the SRDP (solid lines) and the MRDP (diamonds) model as a function of time t (a) and dimensionless time t_D (b). Models with more smaller matrix blocks expel the non-wetting fluid faster due to the increased fracture-matrix surface area. Recovery curves obtained with SRDP and MRDP simulations for case 1 coincide for uniform matrix block size distribution. For cases 2 to 6, the recovery predicted with the SRDP model is always faster than the recovery predicted with the MRDP model.

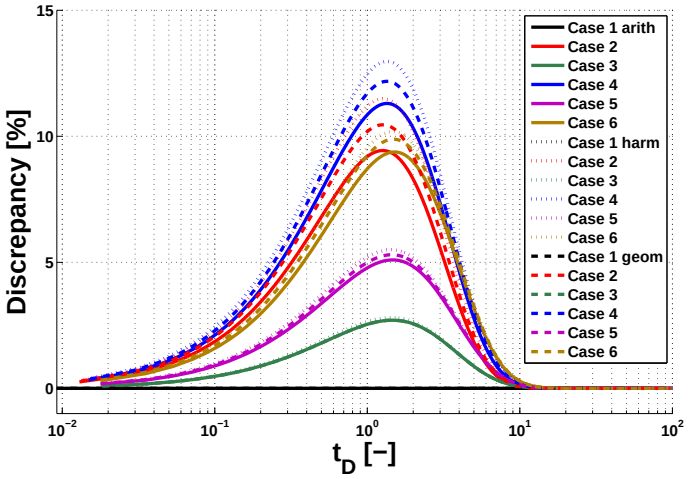

Figure 4.6: Relative discrepancy ΔR for SRDP and MRDP predictions. The solid lines represent the discrepancy to SRDP simulations using the arithmetic mean for averaging L_c, the dashed lines correspond to discrepancy for a geometric mean and the dotted lines show the difference between recoveries obtained with the MRDP model and the SRDP model using the harmonic mean. The more heterogeneous the model is, the higher is the discrepancy: for case 1 the difference between SRDP and MRDP simulations is zero because the matrix has uniform properties. In general, arithmetic mean for averaging L_c in the SRDP model leads to the smallest difference between the two DP models.

ror at intermediate times for both approaches, SRDP and MRDP, one should consider applying a different shape factor formulation.

4.3.2 *Different Matrix Permeability*

In the previous section, It was assumed that the matrix permeability is uniform. In most reservoirs, the matrix permeability will vary at the scale below a simulation grid block. Such heterogeneities have subtle impacts on capillary driven fracture matrix exchange: Blocks with higher permeability have orders of magnitude different transfer rate coefficients β compared to low permeability matrix blocks. To study the effect of heterogeneous permeability on fracture matrix transfer, $K_{m2} = 100\ mD$ is assigned to the smaller sub-domain, that is Ω_2 for cases 1, 2, 4 and 6, and Ω_1 for cases 3 and 5. The majority of the matrix volume is still occupied by rocks with $K_{m1} = 10\ mD$. The average permeability for SRDP simulations, K_Ω, is computed using arithmetic, harmonic or geometric mean weighted with the volumes of Ω_1 and Ω_2 (Table 4.4). Table 4.5 and 4.6 show the corresponding averaged transfer rate coefficients β_Ω and the multi-rate coef-

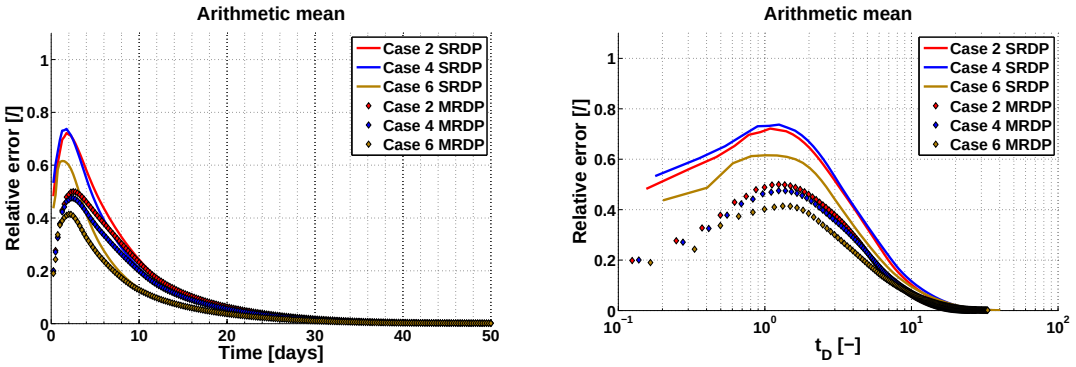

(a)

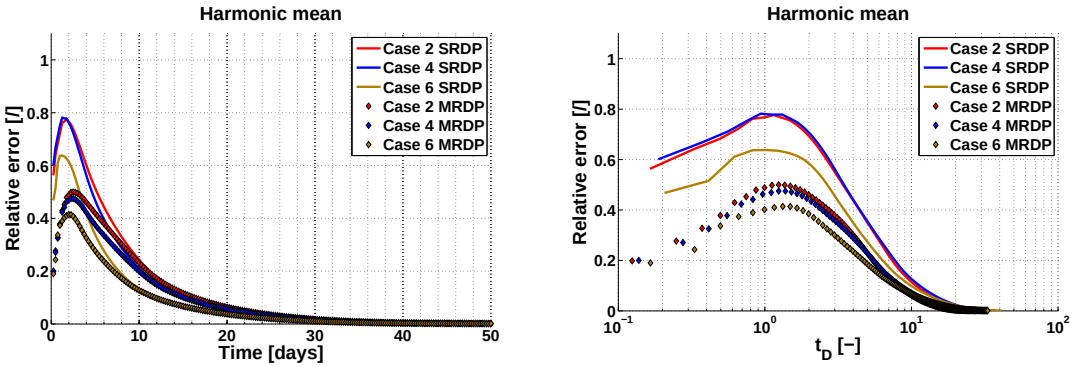

(b)

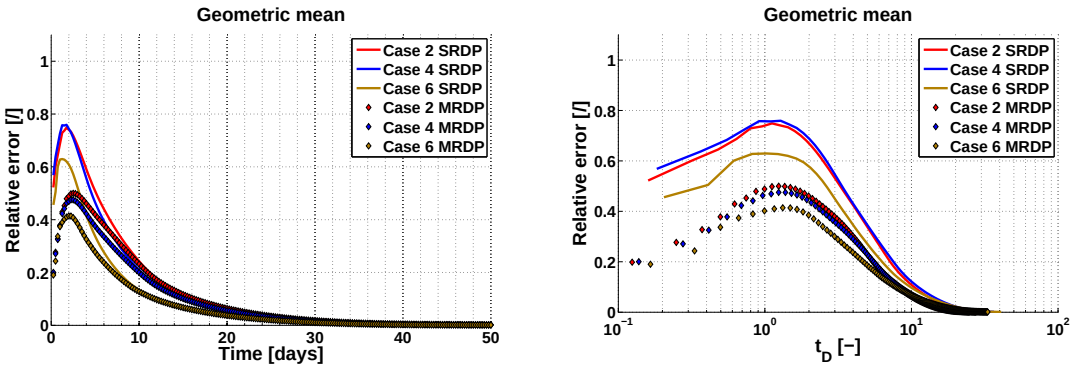

(c)

Figure 4.7: Relative error of SRDP and MRDP simulations for cases 2, 4, and 6 compared to fine-grid simulation results as a function of time t (left) and dimensionless time t_D (right) using arithmetic mean (a), harmonic mean (b) and geometric mean (c) for averaging L_c in the SRDP simulations. The MRDP model (diamonds) leads to better predictions of oil recovery than the SRDP model (solid lines).

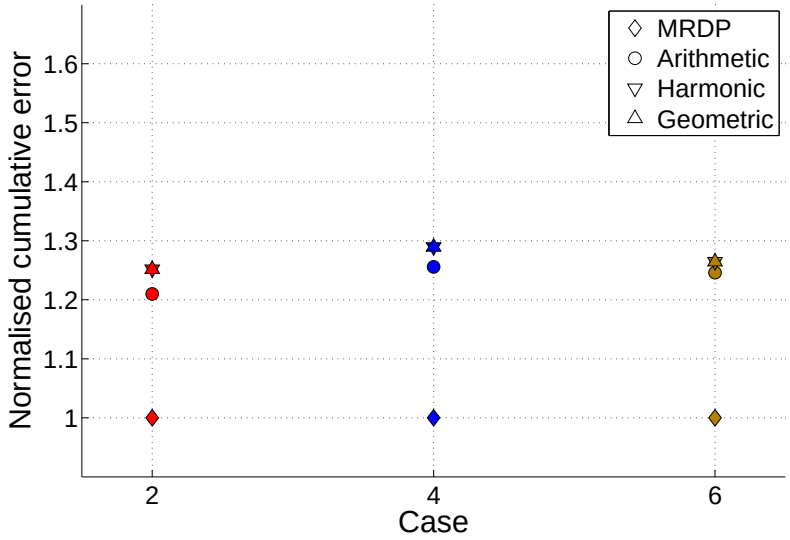

Figure 4.8: Normalised cumulative error of SRDP and MRDP simulations for case 2, 4 and 6 compared to fine-grid simulations. The cumulative error of the SRDP simulations is 25% higher than the cumulative error of the MRDP approach. The smallest error is obtained using the arithmetic mean for averaging L_c. Using harmonic or geometric mean results in the same cumulative error.

ficients β_{Ω_1} and β_{Ω_2}.

K_Ω $[mD]$	1	2	3
arithmetic mean	55.0	21.25	21.25
harmonic mean	18.18	11.26	11.26
geometric mean	31.62	13.33	13.33
K_Ω $[mD]$	4	5	6
arithmetic mean	32.50	32.50	55.0
harmonic mean	12.90	12.90	18.18
geometric mean	17.78	17.78	31.62

Table 4.4: Averaged matrix permeability K_Ω for SRDP simulations.

Varying the matrix permeability and averaging it for the SRDP model yields significantly different results for SRDP and MRDP simulations even for a very modest permeability differences of one order of magnitude. The discrepancy in predicted recovery between the SRDP and MRDP approaches is highest using the arithmetic mean and smallest using the harmonic mean (Fig. 4.9). This is exactly the opposite to the trend observed when only the shape factor varies (Fig. 4.6).

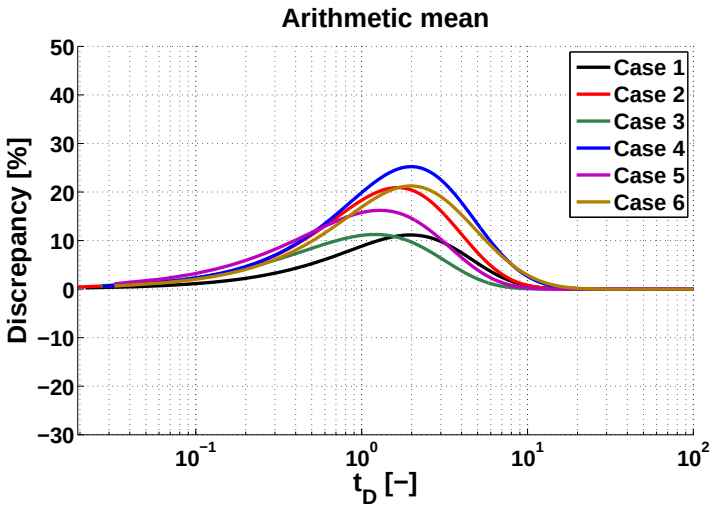

(a)

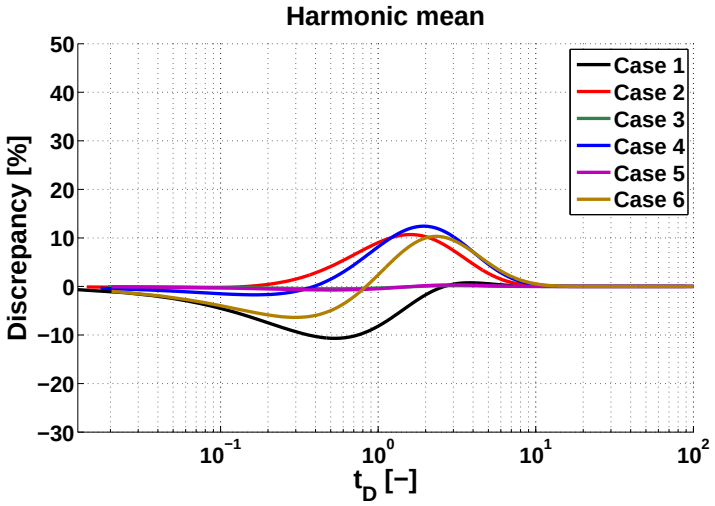

(b)

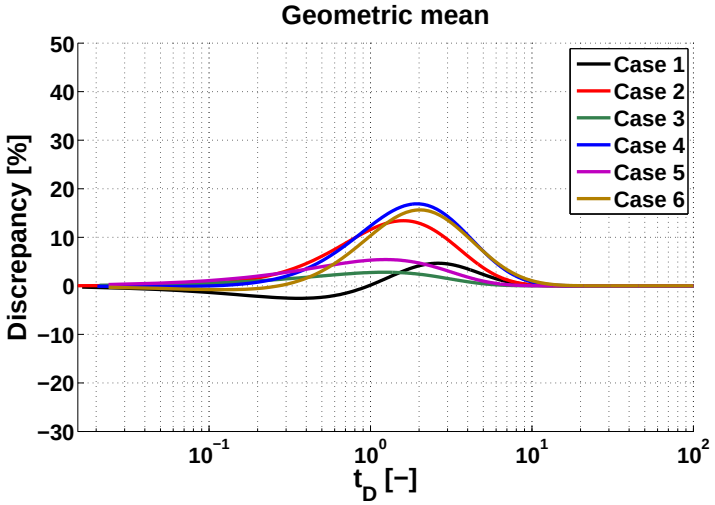

(c)

Figure 4.9: Relative discrepancy ΔR for SRDP and MRDP predictions of non-wetting fluid recovery against t_D, using arithmetic mean (a), harmonic mean (b) and geometric mean (c) when computing the averaged permeability K_Ω for SRDP simulations. The arithmetic mean gives the highest discrepancy for all models.

β_Ω $[sec^{-1}]$	1	2	3
arith. mean	1.20×10^{-5}	1.08×10^{-5}	1.47×10^{-5}
harm. mean	6.90×10^{-6}	7.85×10^{-6}	1.07×10^{-5}
geom. mean	9.09×10^{-6}	8.54×10^{-6}	1.17×10^{-5}
β_Ω $[sec^{-1}]$	4	5	6
arith. mean	1.53×10^{-5}	1.79×10^{-5}	2.22×10^{-5}
harm. mean	9.62×10^{-6}	1.13×10^{-5}	1.28×10^{-5}
geom. mean	1.13×10^{-5}	1.33×10^{-5}	1.69×10^{-5}

Table 4.5: Averaged transfer rate coefficients β_Ω for SRDP simulations including matrix heterogeneity.

	1	2	3
β_{Ω_1} $[sec^{-1}]$	5.12×10^{-6}	5.12×10^{-6}	1.62×10^{-5}
β_{Ω_2} $[sec^{-1}]$	1.62×10^{-5}	3.23×10^{-5}	1.02×10^{-5}
	4	5	6
β_{Ω_1} $[sec^{-1}]$	5.12×10^{-6}	1.62×10^{-5}	5.12×10^{-6}
β_{Ω_2} $[sec^{-1}]$	3.23×10^{-5}	1.02×10^{-5}	3.23×10^{-5}

Table 4.6: Multi rate transfer coefficients β_{Ω_1} and β_{Ω_2} for the MRDP simulations.

Increasing the permeability for the large matrix blocks in cases 3 and 5 doubles the transfer rate between matrix and fractures in the sub-domain Ω_1, which leads to approximately the same transfer rate coefficient that is present in Ω_2. In other words, both domains are releasing the non-wetting fluid at similar rates, hence little to no multi-rate characteristics are observed here. The SRDP with a transfer rate coefficient $\beta_\Omega \approx \beta_{\Omega_1} \approx \beta_{\Omega_2}$ will therefore lead to a good match of recovery curves from the fine-grid simulations. On the other hand, increasing the permeability to 100 mD in the smaller blocks (cases 1, 2, 4, and 6) triples the transfer rate for the sub-domain Ω_2. Therefore, fractures are filled with the non-wetting fluid six times faster and multi-rate behaviour can be expected. Figure 4.10 shows the results of SRDP and MRDP simulations for cases 2, 4 and 6. The SRDP simulations scaled with the dimensionless time t_D show the same recovery regardless of the matrix heterogeneity and shape factor because they were computed using one average transfer rate coefficient β_Ω. In contrast, the MRDP approach models the multi-rate behaviour observed in the fine-grid simulations. The small matrix blocks $M_{l_2} \in \Omega_2$ are releasing the the non-wetting fluid faster than the bigger blocks but are limited by the volume of Ω_2. Once the smaller blocks are depleted, recovery slows down to the rate of the fluid ex-

change between fractures and matrix blocks in the sub-domain Ω_1. The recovery curves map the same trend as the fine-grid simulations, but are slightly shifted in time. The relative error for MRDP simulations confirms this: It remains nearly constant at 40% until it drops to zero when the ultimate recovery is reached. Small decrease of the fitting parameter γ in Eq. 3.14 could lead to a better match between the fine-grid results and the MRDP results as it would slightly delay the recovery. In Fig, 4.10, it can also be observed, that the multi-rate behaviour is mostly prominent in case 6, where the two sub-domains Ω_1 and Ω_2 occupy the same volume. Therefore the transfer rates β_{Ω_1} and β_{Ω_2} have a similar influence on the recovery. In contrast, the multi-rate behaviour for cases 2 and 4 is less noticeable as one finds that $\Omega_1 > \Omega_2$, such that the recovery is more controlled by β_{Ω_1}. The relative error for SRDP simulations ranges between 80% and 100% using arithmetic mean, 40% and 70% using the harmonic mean and 40% and 80% for geometric mean, respectively (Fig. 4.11).

In general, one observes that the relative error for SRDP simulations using different averaging techniques is at least twice as high at the maximal turning point as the error for the MRDP model for very moderate matrix permeability contrasts of a factor 10. However, geological reservoirs often have much stronger permeability contrasts. Compared to similar cumulative error results obtained for different mean types when only the matrix block size varied (Fig. 4.8), the cumulative error for SRDP simulations here is more scattered and ranges between 15% and 40% above the MRDP cumulative error (Fig. 4.12). Here, using the arithmetic mean for averaging K_m leads to the highest error while the harmonic mean leads to the lowest error. Again, the error for SRDP and MRDP simulations can be reduced by choosing a different shape factor formulation.

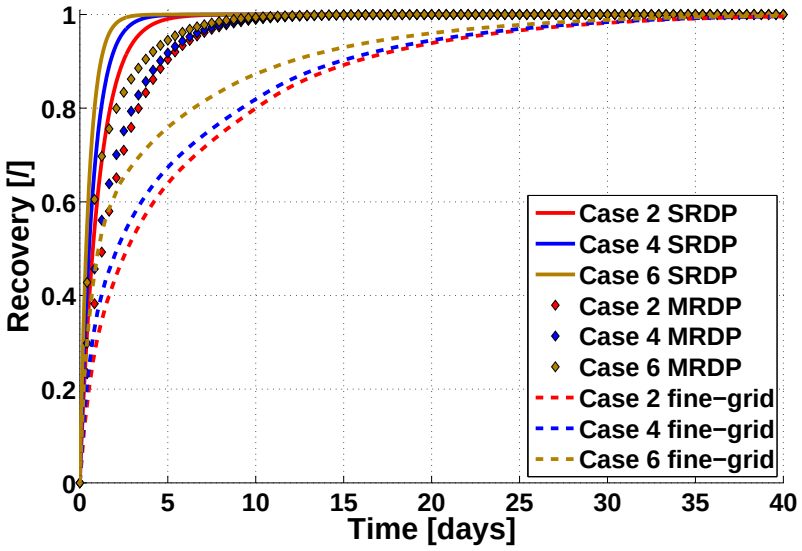

(a)

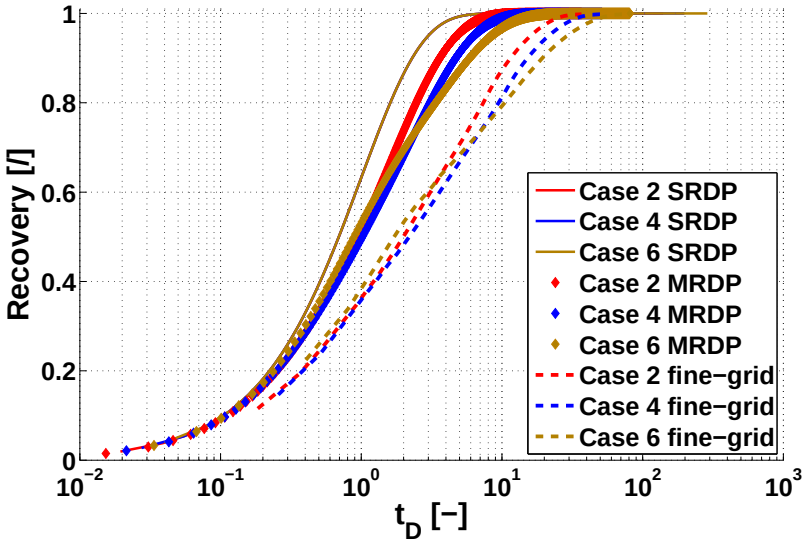

(b)

Figure 4.10: SRDP, MRDP and fine-grid simulations for cases 2, 4, and 6 but now including heterogeneity in matrix permeability as well as a function of time t (a) and dimensionless time t_D (b). The MRDP approach (diamonds) leads to better predictions of oil recovery than the SRDP model (solid lines). The recovery curves show the same trend as the fine-grid simulations (dashed line), but are shifted in time.

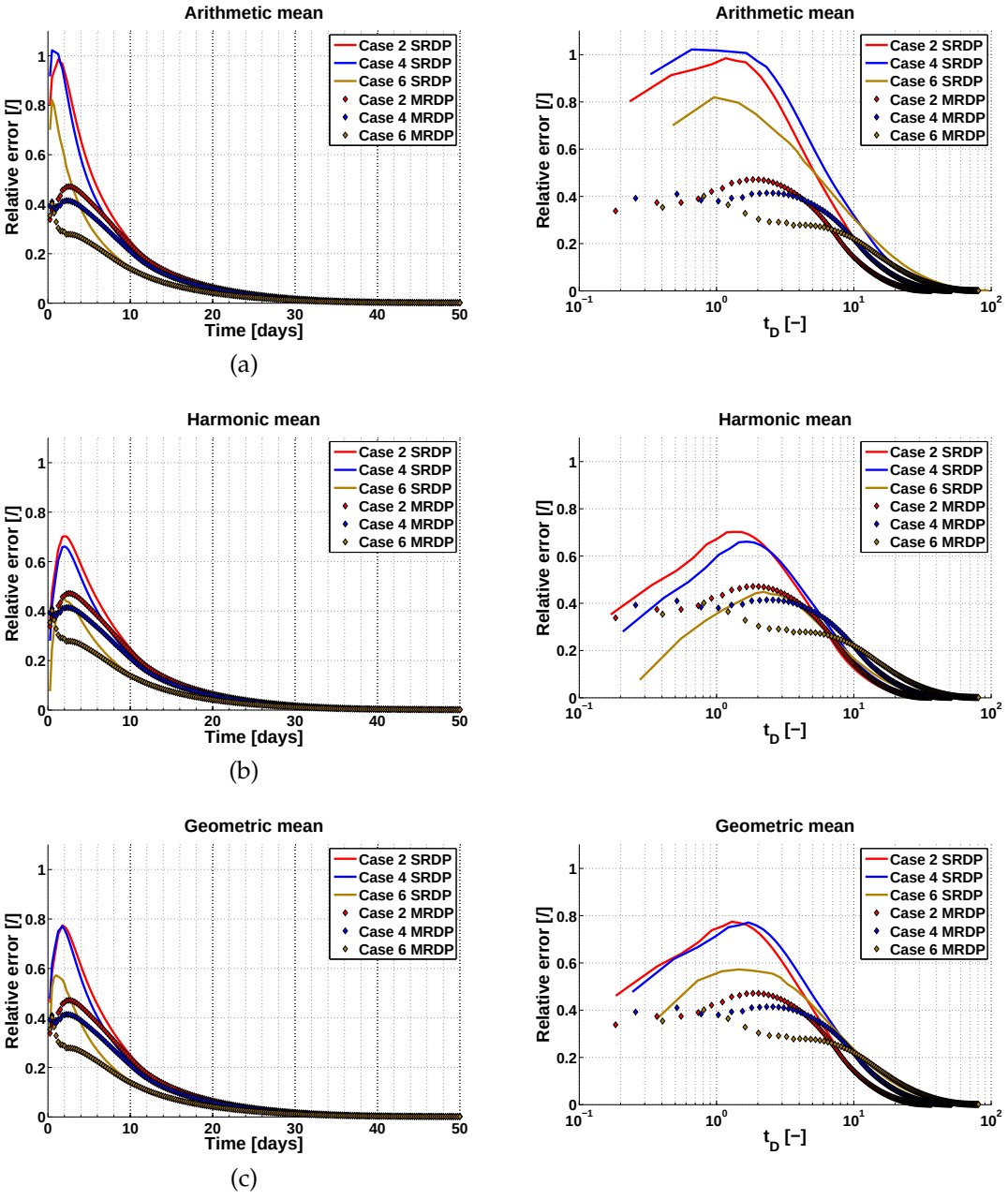

Figure 4.11: Relative error for SRDP and MRDP simulations compared to fine-grid simulations for cases 2, 4, and 6, now including heterogeneity in the matrix permeability as a function of time t (left) and dimensionless time t_D (right). The MRDP approach (diamonds) yields better predictions of non-wetting fluid recovery than the SRDP model (solid lines) using the arithmetic (a), harmonic (b) or geometric mean (c) averaging, except for case 6.

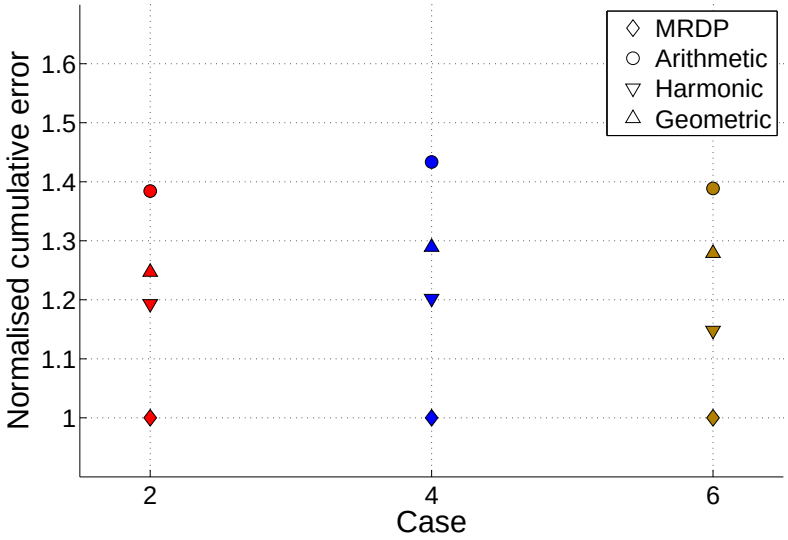

Figure 4.12: Normalised cumulative error of the SRDP and MRDP simulations compared to fine-grid simulations for variable matrix permeabilities.

4.4 SUMMARY

In this chapter the MRDP approach was presented. It allows for modelling sub-grid heterogeneities in a dual continuum model. The heterogeneous rock matrix in a simulation grid block is divided into N sub-domains defined by their respective parameter sets $(K_{mk}, \phi_{mk}, k_{rwk}, k_{rnwk}, P_{ck}, L_{ck}, \mu_w, \mu_{nw}, \rho_{rw}, \rho_{nw})$. Fluid exchange between the k_{th} matrix sub-domain and the fractures is defined individually using transfer functions T_k^{SI} (Eq. 4.7) or T_k^{GD} (Eq. 4.8) when capillary or gravitational forces dominate the process. The saturations in the flowing domain is then updated using the sum of the N transfer functions maintaining the material balance between fractures and rock matrix.

I then examined the effect of different sub-grid heterogeneity, that is different matrix block sizes and sub-domains with contrasting matrix permeability. MRDP results compared to fine-grid simulations gave a reasonable prediction of the recovery of the non-wetting fluid due to spontaneous imbibition. The multi-rate behaviour observed for the fine-grid simulations was modelled adequately with the MRDP approach, although recovery can be shifted in time. The MRDP predictions can be further improved by using a different shape factor which accounts for non-linear saturation gradients in a matrix block. Modelling multi-rate behaviour for SRDP simulations was attempted using different means to average

characteristic lengths L_c and matrix permeabilities K_m. The results in this chapter indicate that it is very difficult to find a universal procedure that could be used to average these properties. Here, the arithmetic mean yields better results to average L_c, where the harmonic mean suited to average K_m. Overall, the conventional SRDP model yields faster non-wetting fluid recovery than the MRDP model. Only on rare cases, that is when the matrix sub domains release the non-wetting phase at a similar rate, the SRDP gives reasonable approximation of recoveries. Such scenarios are very unlikely, considering that the small scale heterogeneity prevail in geological formations.

Although the effect of sub-grid heterogeneity in only capillary dominated systems was studied in this chapter, the small-scale heterogeneity will somewhat affect recovery in gravitational drainage processes. This effect is less prominent as for spontaneous imbibition processes as the transfer rate coefficient β^{GD} scales with $1/L$ only in contrast to $1/L^2$ for β^{SI}. This will be demonstrated in the next chapter (Ch. 5).

5

COMBINING UNSTRUCTURED GRIDS, DISCRETE FRACTURE REPRESENTATION AND DUAL-POROSITY MODELS FOR IMPROVED SIMULATION OF NATURALLY FRACTURED RESERVOIRS

5.1 INTRODUCTION

Most Naturally Fractured Reservoirs (NFR) contain large faults, fracture corridors, and fractures larger than a common reservoir simulation grid block, which can act as conduits or barrier to fluid flow (Fig. 5.2). However, they also contain regions with small-scale fractures that will affect the fluid flow at the scale below a reservoir simulation grid cell (Odling, 1997; Aydin, 2000; Berkowitz et al., 2000; Boro et al., 2013).

In Chapter 2, the Discrete Fracture and Matrix (DFM) approach was presented where fractures (faults, fracture corridors, and small-scale fractures) and the rock matrix can be modelled explicitly as discrete objects in the reservoir model. Although this approach is well-suited to represent complexly shaped fractures, it is intractable when modelling both, large- (above grid resolution) and small-scale (below grid resolution) fractures at reservoir scale. Hence, some degree of upscaling for the small-scale fractures is still required.

The most common approach to model fractures in NFR is to compute averaged rock properties for a given grid size and a given Discrete Fracture Network (DFN) by applying suitable upscaling methods (e.g., Oda, 1985). The choice of the grid size is a compromise between the reduction of the mesh size, which affects com-

putational time, and the representation of the heterogeneities in the reservoir. Once the fracture properties have been upscaled, the Dual-Porosity (DP) concept can be applied in the reservoir simulation model (Dershowitz et al., 2000; Cosentino et al., 2001; Ahmed Elfeel et al., 2010; Lemonnier and Bourbiaux, 2010; Hui et al., 2013). The disadvantage of this DFN and DP modelling approach is that sub-grid information can get lost when averaging fracture properties for each simulation grid cell. Therefore, an enhanced DP method, the Multi-Rate Dual-Porosity (MRDP) model was introduced in Chapter 4. In the MRDP model, sub-grid heterogeneity is accounted for by modelling the fluid exchange between fractures and matrix using a sum of transfer functions, one for each small-scale heterogeneity, rather than one average transfer function as in standard Single-Rate Dual-Porosity (SRDP) models. However, the MRDP model is only applicable to regions in the reservoir that contain well connected fracture networks.

In this chapter, a novel combination of the two reservoir simulation approaches are presented for NFR, i.e. a combination of the DFM and the MRDP approach. The reservoir geometry is divided into regions where faults and other large-scale fractures, as well as the rock matrix are modelled explicitly using the DFM approach. The MRDP model is applied in other regions with well connected fractures. Here, classical DFN upscaling can be used to obtain effective fracture permeabilities and shape factors in the reservoir (see Section 1.1.4). Upscaling is required because there are too many small-scale fractures to be represented explicitly in the DFM approach. The multi-scale heterogeneities of the reservoir can therefore be modelled more adequately by accounting explicitly for large faults and fractures in the DFM regions and using the MRDP approach to upscale regions where fractures are well connected.

5.2 DEFINITION OF THE DFM-MRDP MODEL

To combine the DFM and MRDP approaches, the geological model is divided into two regions, the DFM- and the MRDP-region prior to commencing a NFR simulation (Fig. 5.1). The DFM region is defined as a region comprising faults

and fractures above the size of a reservoir simulation grid cell. Here, fractures are sparse and should be represented explicitly because advective flow through the rock matrix may be equally important as flow through faults or fractures. On the other hand, the MRDP region is defined as a region where fracturing is intense such that flow occurs only in the fractures and the application of a dual continuum model is justified. The MRDP region itself is partitioned in two domains, the fracture (flowing) domain and the matrix (stagnant) domain as discussed in Chapter 3.

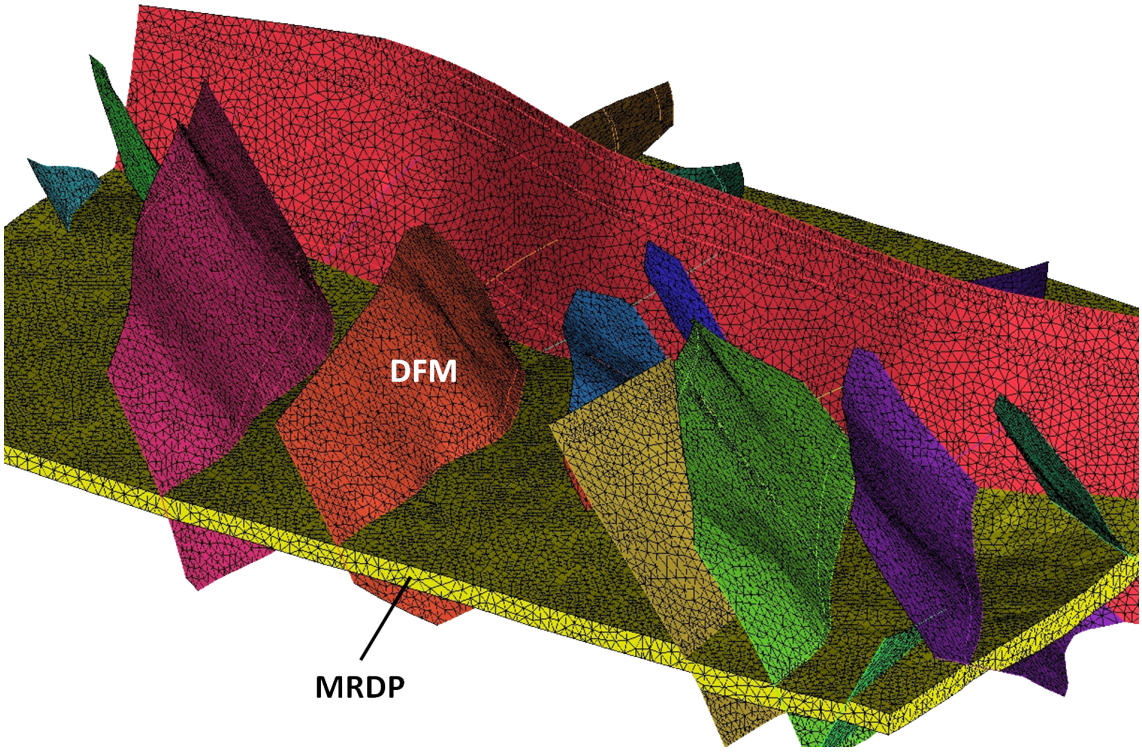

Figure 5.1: Unstructured finite element mesh with large-scale faults represented explicitly using the DFM approach (note that matrix is not shown here). The model also contains a single layer comprising a well-connected fracture network which defines the MRDP region (Mesh courtesy Caroline Milliotte, NFR Studies).

Two domains can now be identified in the NFR model:

1. The flowing domain: This domain comprises the DFM region and the fracture part of the MRDP region

2. The stagnant domain: This domain comprises the matrix part of the MRDP region.

The flowing domain is discretised using an unstructured hybrid element mesh that utilises Finite Element Method (FEM) and Finite Volume Method (FVM) as discussed in Chapter 2. The hybrid mesh enables to flexibly resolve the boundaries between the DFM and MRDP regions, but also to mesh the large-scale fractures in the DFM region. These unstructured grids are not restricted to only modelling fractures. As shown by Jackson et al. (2013) other sedimentary bodies can also be meshed readily with the FEM/FVM method. Volumetric modelling of large faults is possible but only required if the heterogeneity in the fault plane (e.g. fault gauge) itself needs to be represented as a 3D volume. Large scale fractures remain 2D surfaces because modelling them as 3D volumes increases the computational time as the small elements decrease the time step due to the Courant-Friedrich-Lewy (CFL) condition (Eq. 2.9).

Fig. 5.1 shows an example of a mesh that combines DFM and MRDP regions in a fractured reservoir. Values in the DFM regions that are bounded by surfaces contain uniform petrophysical properties. Likewise, each 2D fracture surface has uniform properties. In the MRDP region, average grid-block properties for the fractures can be computed for the flowing domain using, for example, Oda's method to compute effective fracture permeability and shape factors from the underlying DFN (Oda, 1986; Dershowitz et al., 2000).

An important aspect of the meshing process is to maintain the validity of a DP model assumption when selecting the size of the elements in the MRDP region. It has to be ensured that the grid cell size is larger than the largest fracture spacing in this region.

The stagnant domain is defined through a virtual grid that represents the matrix and the corresponding transfer function T (Eq. 4.6) for each grid cell of the MRDP region. In this context, additional variables need to be stored at each grid cell, i.e the matrix rock properties permeability K_m, porosity ϕ_m, relative permeability k_r, capillary pressure P_c, and matrix block size, i.e. the characteristic length L_c, and the residual saturations in the matrix (connate wetting phase saturation S_{wmc} and residual non-wetting phase saturation S_{nwmr}), the saturation of the third, immobile phase S_{im} and the actual fluid saturations (wetting phase sat-

uration S_{wm} and non-wetting phase saturation S_{nwm}). Although the DFM model can be combined with the SRDP approach, the general MRDP approach is employed here, i.e. a distribution of transfer functions is used in each grid cell. This implies that N sets of matrix variables are stored at the nodes rather than just one, according to the previously identified N matrix sub-domains in the MRDP approach (Eq. 4.1). Therefore, at the cell j in the MRDP region, the additional variables that represent the virtual matrix grid cells are:

$$\left(K^j_{mk}\ \phi^j_{mk}\ k^j_{rk}\ P^j_{ck}\ L^j_{ck}\ S^j_{wmck}\ S^j_{nwmrk}\ S^j_{imk}\ S^j_{wmk}\ S^j_{nwmk}\right),\ k = 1 \dots N \tag{5.1}$$

Using these matrix and fluid properties, the ratios of capillary forces to gravitational forces r^j_k (Eq. 3.2) are computed in each grid cell of the MRDP region, which yields the transfer rate coefficients at the cell j:

- $\beta^{SI,j}_k$ if capillary forces dominate (Eq. 3.12) or
- $\beta^{GD,j}_k$ if gravity forces dominate (Eq. 3.25).

Temporal discretisation uses the Implicit Pressure Implicit Saturation (IMPIS) algorithm (Chapter 2) for the entire flowing domain, regardless if a reservoir region belongs to the DFM or to the MRDP region. It is reiterated that the IMPIS method consists of sequential implicit solution of the pressure equation using FEM and an implicit solution of the saturation equation using FVM. The latter can be split further applying Strang operator splitting into an implicit solution of the advection equation using FVM and an implicit solution of the capillary diffusion equation using FEM. In the MRDP regions, an update of the saturations in the fractures and matrix after each IMPIS step is necessary to account for the fracture-matrix fluid exchange (Eq. 3.1).

The DFM region belongs entirely to the flowing domain, hence, further properties (Eq. 5.1)representing the virtual matrix are not needed. The additional variables for the virtual grid cells can either be set to zero or are not defined in first place to reduce the allocated memory. In both cases, the transfer rate coefficients are $\beta^{SI} = \beta^{GD} = 0$ and therefore, the transfer term is $T = 0$.

In summary, the DFM-MRDP approach for simulating flow in a NFR can be described as follows:

- Identify DFM and MRDP regions when modelling the reservoir and generating the finite element grid
- Upscale fracture properties in the MRDP regions and identify N matrix subdomains based on the heterogeneity of the rock properties and matrix volumes
- Compute and store the transfer rate coefficients in the MRDP regions
- Solve the pressure equation in the flowing domain (i.e. DFM domain and fractures in the MRDP domain) using FEM
- Compute the velocity field in the flowing domain
- Solve saturation equation in the flowing domain using FVM or apply Strang splitting to solve the advection equation using FVM and solving the diffusion equation using FEM
- Update saturation values of the flowing and stagnant domain of the MRDP regions using stored transfer rate coefficients.

5.3 OVERVIEW OF RESERVOIR SIMULATION MODELS AND SCENARIOS

This section provides an overview of the simulations using the DFM-MRDP approach. The simulations were performed to demonstrate the DFM-MRDP concept by studying different two-phase flow scenarios including spontaneous imbibition and gravity drainage. Fig. 5.2 shows an outcrop of a fractured Jurassic carbonate rock which acts as the motivation for the proof-of-concept studies that will be discussed in detail in the next sections.

In total, 6 flow scenarios are considered in the simulations. First, water flooding simulations are presented in a model containing three highly fractured layers (Section 5.4) which correspond to a scenario depicted in Fig. 5.2 (b). The three layers are identified as MRDP regions. Recall that Chapter 4 discussed a study

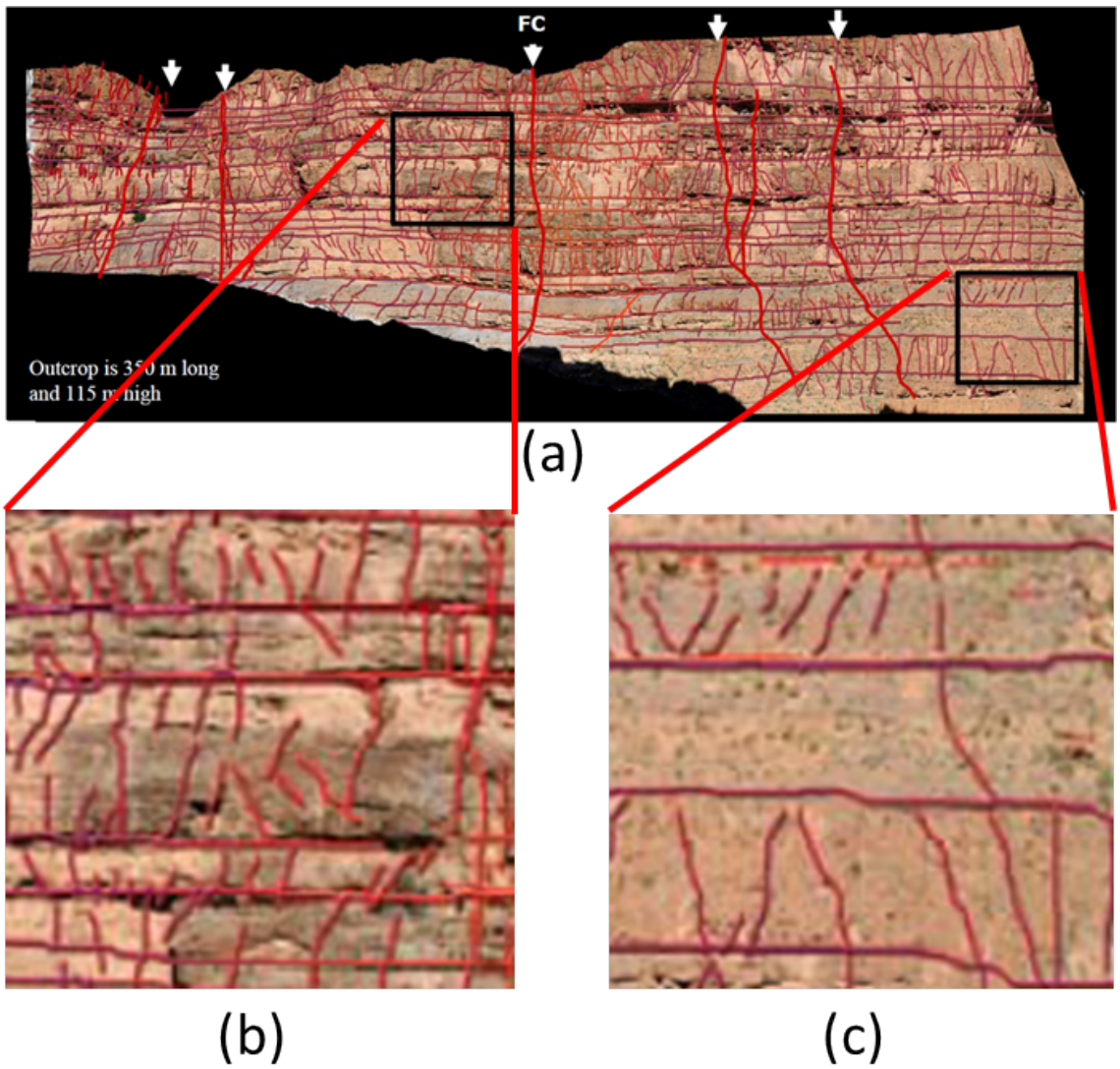

Figure 5.2: Above: Interpretation of fracture traces of a Jurassic Carbonate Ramp analogue from the High Atlas, Morocco (Agar et al., 2010). Below: two outcrop windows representing different multi-scale heterogeneity: several adjacent layers containing many bed confined fractures and heterogeneous rock matrix (b) and a less fractured layer between two highly fractured beds (c).

of the fluid transfer from matrix to fractures which were constantly filled with the wetting fluid. It was assumed that the the oil that was expelled due to spontaneous imbibition was immediately transported away in the fractures, that is the wetting phase saturation in the fracture was held constant at $1 - S_{nwr}$. Now a more realistic scenario is studied where advection in the flowing domain is considered and the saturations in the fracture can vary over time. Small-scale heterogeneities in the MRDP regions are introduced in the simulations discussed in Section 5.4 through different matrix block sizes, i.e. different characteristic lengths. Large-scale heterogeneity is included by assigning different rock matrix permeability to the individual layers. Whereas the same permeability is assigned to all three layers for simulation NFR1, higher permeability was chosen for the middle layer compared to the permeability of the top and bottom layer for the simulation NFR2 (Table 5.1). Strictly speaking these simulations do not employ the DFM-MRDP approach but rather the MRDP approach because no DFM regions are present. Nevertheless, the workflow discussed in Section 5.2 can be equally applied in a situation where the flowing domain consists only of the fractures in the MRDP domain and not the fractures and matrix in the DFM domain. For simplicity gravity effects were neglected by assigning the same density of $\rho = 1000\ kg/m^3$ to both fluids, oil and water. In this way the injected water did not flow preferentially through the lower layers; in other words, fluid flow is relatively evenly distributed in all three layers and therefore the impact of geological heterogeneity in each layer on fluid flow is more pronounced.

The complete DFM-MRDP approach is then demonstrated by simulating water flooding and gravity drainage experiments in a model that contains DFM and MRDP regions with two highly fractured layers connected by a sparsely fractured layer (Section 5.5); this corresponds to a scenario similar to the fracture geometries shown in Fig. 5.2 (c). Small-scale heterogeneity is again modelled by introducing different matrix block sizes in the MRDP regions, i.e. the top and bottom layers. Large-scale heterogeneity is represented by the fractures in the DFM region, i.e. the middle layer. In contrast to the simulations NFR1 and NFR2, gravity effects are also simulated by assigning different densities to the fluids. In simulation NFR3, the fluids are assumed to be oil and water, in NFR4 gas and

oil (Table 5.1).

Model Name	Geometry	Simulation	Fracture-Matrix Transfer
NFR1	Three highly fractured layers (MRDP regions). All three layers have matrix permeability of $K_m = 1\ mD$ (Fig. 5.3).	Water flooding	Spontaneous counter-current imbibition
NFR2	Three highly fractured layers (MRDP regions). Top and bottom layers have matrix permeability of $K_m = 1\ mD$. Central layer has a permeability of $K_m = 10\ mD$ (Fig. 5.3).	Water flooding	Spontaneous counter-current imbibition
NFR3	Two highly fractured layers at the top and at the bottom (MRDP regions). One central layer with few large-scale fractures (DFM region) (Fig. 5.6a).	Water flooding	Spontaneous counter-current imbibition
NFR4	Two highly fractured layers at the top and at the bottom (MRDP regions). One central layer with few large-scale fractures (DFM region) (Fig. 5.6b).	Gas injection	Gas gravity drainage

Table 5.1: Overview of simulation models using the DFM-MRDP approach

The model NFR3 is also used to study the numerical error arising from the operator splitting, i.e. from sequentially solving the pressure and the advection equation followed by the update of the saturation values due to fracture-matrix transfer in the MRDP regions (Section 5.6). The numerical error is studied by taking successively smaller time-steps from 10 *min* (largest) to 5 *sec* (smallest).

To investigate the effect of the small-scale (sub-grid) heterogeneity in the MRDP regions on the overall flow behaviour and the resulting oil recoveries, three different cases are considered for each simulation scenario listed in Table 5.1:

- MRDP case MR1: MRDP regions comprise two matrix sub-domains ($N = 2$) where the second sub-domain contains smaller matrix blocks than the first sub-domain

- MRDP case MR2: MRDP regions comprise two matrix sub-domains ($N = 2$) where the second sub-domain contains larger matrix blocks than the first sub-domain

- SRDP case SR1: MRDP regions comprise one matrix domain ($N = 1$). The characteristic length and the porosity are averaged such that they represent the same matrix volume as in MR1 and MR2. This case is used to compare the standard DP approach with the MRDP approach.

In contrast to SRDP and MRDP simulations in Chapter 4, a different formulation of the characteristic length L_c is used here. L_c was defined according to Ma et al. (1999):

$$L_c = \sqrt{\frac{V_b}{\sum_{i=1}^{n} A_i / l_{A_i}}}, \tag{5.2}$$

where V_b is the bulk volume of the matrix block, A_i the area open for imbibition in the i-th direction, and l_{A_i} the distance to the nearest no-flow boundary. This formulation was also used by Di Donato et al. (2007) for their experiments and takes the volume and the surface areas of the matrix blocks into account. This approach can be considered as a generalisation of the shape factor of Kazemi et al. (1976). In fact, assuming that all matrix blocks have the shape of a cube will lead to the same value for the characteristic length L_c, for both the shape factor of Kazemi et al. (1976) and that of Ma et al. (1999).

In order to compare simulation results for SRDP and MRDP approaches, the following relation

$$\phi_{m_{SRDP}} L_{c_{SRDP}} = \sum_{k=1}^{N} \phi_{mk} L_{c_k} \tag{5.3}$$

is used to scale the characteristic length of each matrix sub-domain, i.e. to ensure that in all three cases (SR1, MR1 and MR2) the overall matrix volume remains constant and the initial amount of oil in the matrix rock is the same, regardless of the approach used (SRDP or MRDP).

5.4 MRDP SIMULATIONS

In Chapter 4, the effect of sub-grid heterogeneity on non-wetting phase recovery was presented at the scale of a simulation grid cell size. In contrast, the universal transfer rate for spontaneous imbibition at inter-well scale is now used to illustrate the difference between SRDP and MRDP models. For this, two reservoir simulation models, NFR1 and NFR2, are considered (Table 5.1).

5.4.1 *Water Flooding Simulations NFR1 and NFR2 - Model Setup*

Simulations NFR1 and NFR2 are performed on a model containing three highly fractured layers (MRDP regions) (Fig. 5.3). The model dimensions are $16m \times 10m \times 7m$, which can be scaled to a field-size reservoir without loss of generality. Due to the small model size, simulations were run for only 200 days. The corresponding mesh contains 14k nodes (i.e. finite volumes) and 84k tetrahedral elements. Two vertical wells are introduced, an injector on the left side and a producer on the right side. The bottom hole pressure at the producer has been held constant at $2.0 \times 10^7 Pa$ whereas the injector operated at a constant injection rate of $1m^3/day$.

Table 5.2 shows the rock and fluid properties which were held constant for NFR1 and NFR2 simulation scenarios. To be consistent with the simulation results discussed in Chapter 4, the same pore-scale network relative permeabilities and capillary pressure curves from Oak (1990) and Valvatne and Blunt (2004) were used for a water-wet Berea sandstone (Fig. 3.7) when evaluating the universal transfer rate coefficient β^{SI} (3.12).

The matrix blocks were initially saturated with 60% oil and the residual oil saturation was set to 0.422. The residual saturations and the interfacial tension of 35 mN/m were taken from Behbahani et al. (2006). In the flowing (fracture) domain, the standard Brooks-Corey model with the quadratic relative permeabilities curves is applied. To avoid early water breakthrough, the fractures were

initially completely filled with oil. A viscosity ratio of one is assumed such that both, water and oil have a viscosity of $1.5 \times 10^{-3} Pa \cdot s$.

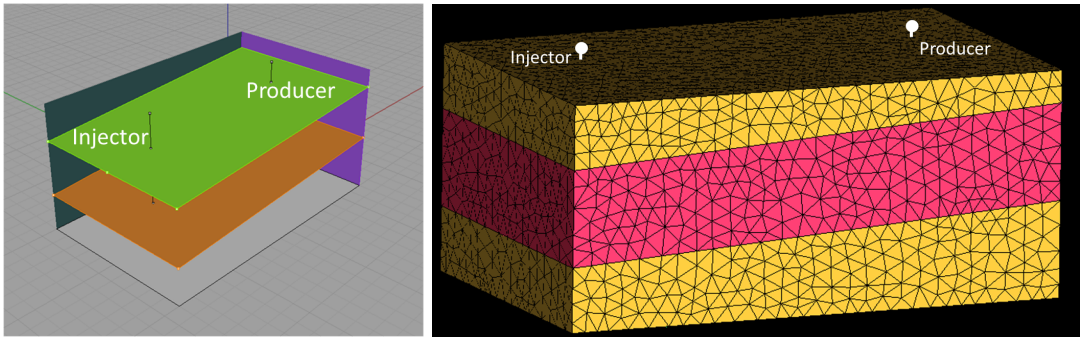

Figure 5.3: Idealised 3D reservoir model (dimensions $16m \times 10m \times 7m$) comprising three fractured layers for simulations NFR1 and NFR2 (Table 5.1). The model contains an injector on the left side and a producer on the right side. The left image shows the model geometry constructed with a CAD software and the right image shows the corresponding unstructured finite element grid (finite volumes are not shown). Each layer is assumed to contain well connected fracture networks. Matrix properties vary from layer to layer. Water is injected into the reservoir at a constant rate ($1m^3/day$), whereas the pressure is fixed at the producer at 2.0×10^7 Pa. The initial water saturation is $S_{wmi} = 0.4$ in all layers but zero in the fractures. Table 5.2 shows the detailed model parameters used in the simulations.

Parameter		Value	Unit
effective fracture permeability	K_f	105	mD
fracture porosity	ϕ_f	0.007	$[-]$
initial water saturation (flowing domain)	S_{wfi}	0.0	$[-]$
residual oil saturation (flowing domain)	S_{ofr}	0.0	$[-]$
initial water saturation (stagnant domain)	S_{wmi}	0.4	$[-]$
residual oil saturation (stagnant domain)	S_{omr}	0.422	$[-]$
interfacial tension	IFT	35	mN/m
viscosity water	μ_w	1.5×10^{-3}	$Pa \cdot s$
viscosity oil	μ_o	1.5×10^{-3}	$Pa \cdot s$

Table 5.2: Fluid and rock properties for SRDP and MRDP simulations on NFR1 and NFR2 models.

SRDP simulations $SR1_{NFR1}$ and $SR1_{NFR2}$ are assumed to have an average characteristic length of $L_c = 0.25$ and an average matrix porosity of $\phi_m = 0.25$ as listed in Table 5.3. The MRDP simulations $MR1_{NFR1}$ and $MR1_{NFR2}$ contain additional smaller matrix blocks with $L_{c2} = 0.05$. This would correspond to a geological scenario where parts of the matrix are heavily fractured (see also the results for

case 3 in section 4.3.1). In contrast, the MRDP simulations $MR2_{NFR1}$ and $MR2_{NFR2}$ contain additional large matrix blocks with $L_{c2} = 1.25$. This corresponds to a scenario where fracturing in parts of the matrix is less intense (see also the results for case 2 in section 4.3.1). I reiterate the SRDP and MRDP simulation results from Chapter 4: The SRDP model cannot account for the fact that parts of the rock matrix might be more ($MR1_{NFR1}$ and $MR1_{NFR2}$) or less ($MR2_{NFR1}$ and $MR2_{NFR2}$) fractured if the transfer rates of the corresponding sub-domains differ greatly. The MRDP model captures this heterogeneity by using N transfer rates for the different matrix sub-domains. The SRDP model employs only a single average transfer function to model the average rate of fracture-matrix fluid exchange, rather than the simultaneous occurrence of fast and slow transfer.

Simulation	L_{c1}	L_{c2}	ϕ_{m1}	ϕ_{m2}
$SR1_{NFR1}/SR1_{NFR2}$	0.25	–	0.25	–
$MR1_{NFR1}/MR1_{NFR2}$	0.25	0.05	0.1	0.75
$MR2_{NFR1}/MR2_{NFR2}$	0.25	1.25	0.1	0.03

Table 5.3: Properties describing the matrix shape and volume in the SRDP and MRDP simulations on the NFR1 and the NFR2 model (Table 5.1).

In the simulation NFR1, the matrix permeability is uniform at $K_m = 1\ mD$ in all three reservoir layers. For the simulation NFR2, the rock matrix permeability of the middle layer is increased to $K_{m2} = 10\ mD$. The permeability of the upper and lower layers was not altered and remained at $K_{m1} = 1\ mD$ (Fig. 5.3).

5.4.2 *Water Flooding Simulations NFR1 - Results*

Fig. 5.4 shows the normalised oil recovery profiles for the simulation NFR1. If the matrix contains additional smaller matrix blocks, i.e. for the MRDP simulation $MR1_{NFR1}$, more matrix surface area is exposed to the injected wetting fluid through these smaller matrix blocks. Hence spontaneous imbibition occurs faster compared to the SRDP case $SR1_{NFR1}$ where the characteristic length L_c implies that matrix blocks are uniform but have the same total volume as in the MRDP case. If the matrix contains larger blocks, i.e. for the MRDP case $MR2_{NFR1}$, oil re-

covery at late time is slower compared to the SRDP case $SR1_{NFR1}$ because transfer from the large matrix blocks occurs at a much lower rate (compare transfer rate coefficient β_2^{SI} in Table 5.4). In this case, the overall fracture-matrix surface area for fluid exchange has decreased. This is consistent with the results obtained for the L_c sensitivity analysis in Section 4.3.1.

Simulation	β_1^{SI} $[sec^{-1}]$	β_2^{SI} $[sec^{-1}]$
SR1	2.43×10^{-9}	-
MR1	3.85×10^{-9}	3.51×10^{-8}
MR2	3.85×10^{-9}	2.81×10^{-10}

Table 5.4: Transfer rate coefficients β_1^{SI} and β_2^{SI} for the MRDP water flooding simulations in NFR1 model.

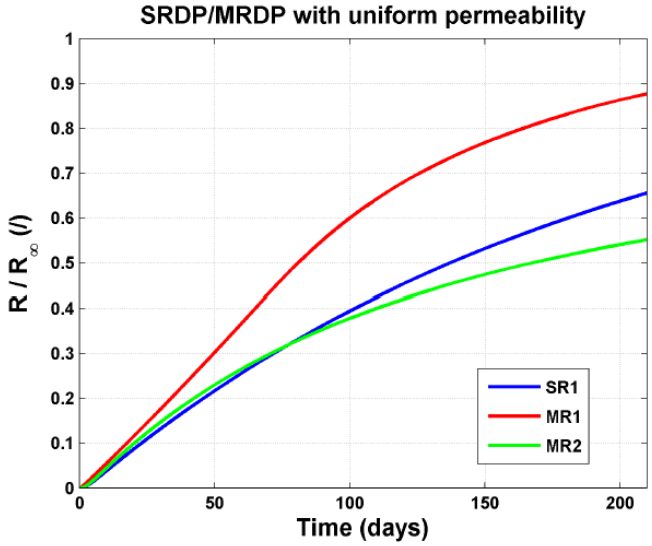

Figure 5.4: Comparison of predicted recoveries using SRDP and MRDP approaches on the NFR1 model. See Tables 5.2 and 5.3 for model parameters and Fig. 5.3 and Table 5.1 for model geometry. The matrix permeability is uniform at $K_m = 1\ mD$ for all three layers. Higher oil recovery is observed if the reservoir is assumed to have more fractures (case MR1). Oil recovery is significantly lower if the reservoir is assumed to have less fractures (case MR2). The SRDP case SR1 predicts slightly higher recovery than case MR2 due to the averaging of transfer rates.

In contrast to the studied cases in the previous chapter where flow in the fractures was neglected (i.e. constant water saturation $S_{wf} = const$), these simulations also account for the dynamic behaviour of flow in the fractures. Faster transfer from the smaller matrix blocks in MRDP case $MR1_{NFR1}$ leads to faster oil recovery but also slows down the rate at which the water front moves in the

flowing domain as more oil is transferred back into the fractures. This causes water breakthrough to be delayed compared to the SRDP case $SR1_{NFR1}$ or the MRDP case $MR2_{NFR1}$. Hence, the lowest final oil recovery is obtained if the reservoir is assumed to have less fractures and the highest recovery is obtained if the reservoir is assumed to contain highly fractured regions.

5.4.3 *Water Flooding Simulations NFR2 - Results*

Fig. 5.5 shows the normalised oil recovery profiles for the simulation NFR2. The higher matrix permeability results in increased transfer rates in the central layer (Table 5.5) and therefore increased final oil recovery for all cases $SR1_{NFR2}$, $MR1_{NFR2}$ and $MR2_{NFR2}$, compared to $SR1_{NFR1}$, $MR1_{NFR1}$ and $MR2_{NFR1}$. As more oil is transferred from the matrix blocks to the flowing domain in the middle layer, the water front advances slower and water breakthrough is delayed. Note that the recovery behaviour of SRDP simulations $SR1_{NFR1}$ and $SR1_{NFR2}$ versus MRDP cases $MR2_{NFR1}$ and $MR2_{NFR2}$ are qualitatively comparable: The SRDP simulations predicted faster and higher recovery compared to the MRDP simulations because larger matrix blocks cause oil to be released at a lower rate. This slows down recovery at late time. In contrast, the predicted recoveries from SRDP simulations $SR1_{NFR1}$ and $SR1_{NFR2}$ compared to the MRDP cases $MR1_{NFR1}$ and $MR1_{NFR2}$ are strikingly different. This is because the transfer rates in the MRDP simulation with uniform permeability for the entire model (case $MR1_{NFR1}$) are already high which delays water breakthrough and allows for more oil to be recovered from the stagnant (matrix) domain. In this case, increasing the matrix permeability of the central layer does not change this behaviour notably but does increase the transfer rates in SRDP case $SR1_{NFR2}$ and MRDP case $MR2_{NFR2}$ significantly. This affects in particular the early time recovery until the water breakthrough has occurred in the middle layer.

$K_{m1} = 1\ mD$ (upper & lower layer)		
Simulation	$\beta_1^{SI}\ [sec^{-1}]$	$\beta_2^{SI}\ [sec^{-1}]$
SR1	2.43×10^{-9}	-
MR1	3.85×10^{-9}	3.51×10^{-8}
MR2	3.85×10^{-9}	2.81×10^{-10}
$K_{m2} = 10\ mD$ (central layer)		
Simulation	$\beta_1^{SI}\ [sec^{-1}]$	$\beta_2^{SI}\ [sec^{-1}]$
SR1	7.70×10^{-9}	-
MR1	1.21×10^{-8}	1.11×10^{-7}
MR2	1.21×10^{-8}	8.89×10^{-10}

Table 5.5: Transfer rate coefficients β_1^{SI} and β_2^{SI} for the MRDP water flooding simulations in NFR2 model.

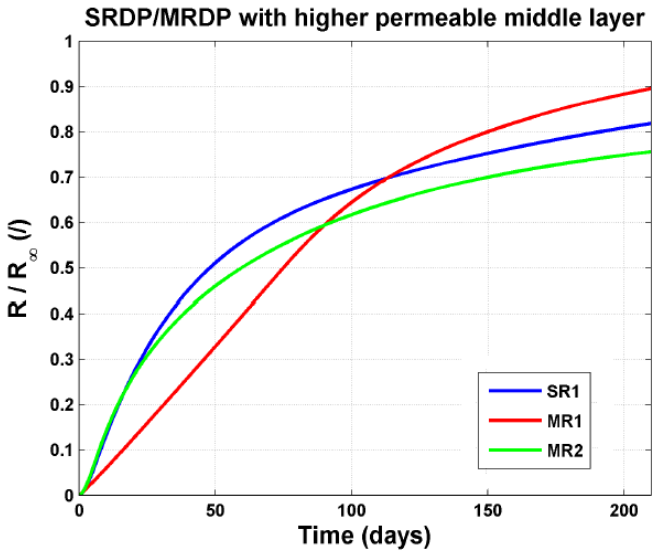

Figure 5.5: Comparison of predicted oil recoveries using SRDP and MRDP approaches in NFR2 model. See Tables 5.2 and 5.3 for model parameters and Fig. 5.3 and Table 5.1 for model geometry. A higher matrix permeability of $K_{m2} = 10\ mD$ is assigned to the central layer. The matrix permeability for the upper and lower layers remains at $K_{m1} = 1\ mD$. The recovery for SRDP case MR1 and MRDP case MR2 increased significantly in comparison to the NFR1 model. This is due to the increased transfer rates in the central layer (see Tab. 5.5). The transfer rates for MRDP case MR1 increased less, subsequently the predicted oil recovery for MR1 is almost identical with the oil recovery obtain for NFR1.

5.4.4 *Discussions of MRDP Simulation Results*

Although these simulations are idealised, they still demonstrate that a MRDP model is likely to predict oil recovery more accurately because it captures the sub-grid variability of fracture density and matrix permeability more adequately. The MRDP approach allows for fast and slow transfer rates to occur simultaneously in each grid block. Note that through the approach of averaging the characteristic length $L_{c_{SRDP}}$ and the matrix porosity $\phi_{m_{SRDP}}$ (Eq. 5.3), the averaged SRDP cases $\mathrm{SR1}_{NFR1}$ and $\mathrm{SR1}_{NFR2}$ are two possible representations of models described by MRDP cases $\mathrm{MR1}_{NFR1}/\mathrm{MR2}_{NFR1}$ and $\mathrm{MR1}_{NFR2}/\mathrm{MR2}_{NFR2}$, respectively. However, the multi-rate behaviour cannot be captured by a single, averaged transfer rate and the difference of expected oil recovery and rate of recovery between SRDP and MRDP cases is large. Depending on the matrix block size distribution (or permeability variations in the matrix), the SRDP can under- or over-predict the oil recovery in a very significant way. To summarise, accounting for sub-grid heterogeneities using the MRDP approach results in significantly different overall recoveries of hydrocarbons. The multi-rate transfer functions affect both the early and late time behaviour.

5.5 DFM-MRDP SIMULATIONS

In this section, simulations using the models NFR3 and the NFR4 (Table 5.1) are presented using the DFM-MRDP approach. The simulations account for both, capillary and gravitational forces, during fracture-matrix mass transfer. For this purpose, three water flooding and three gas gravity drainage simulations were carried out using the DFM-MRDP simulator on an idealised reservoir model (dimensions $10m \times 2m \times 10m$). In the gas gravity drainage simulations, an impermeable layer has been included at the top to prevent gas leakage (Fig. 5.6). Note that, as in the previous simulations (NFR1 and NFR2), the model can be scaled to a field-size reservoir without any loss of generality.

Multi-scale heterogeneity was introduced by defining two highly fractured areas where the matrix blocks are surrounded by fractures that are assumed to be

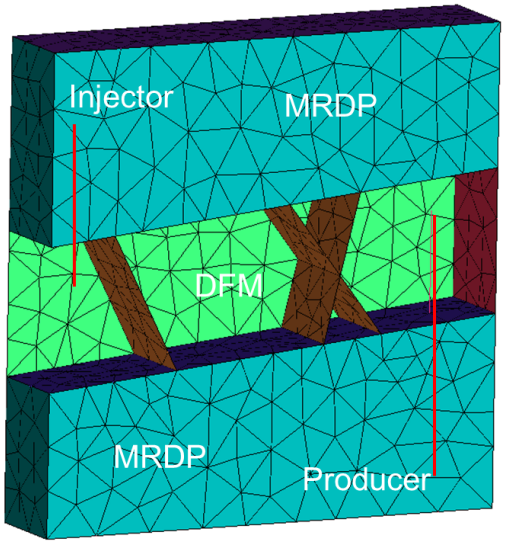

(a)

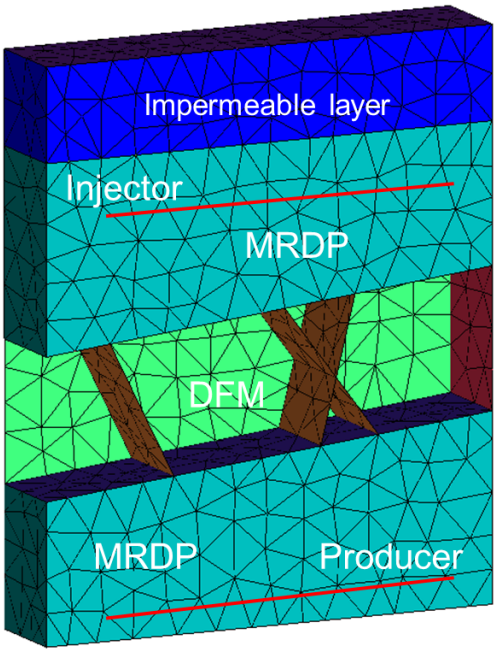

(b)

Figure 5.6: Simplified 3D fractured reservoir models ($10m \times 2m \times 10m$): NFR3 for water flooding simulations (a) and NFR4 for gas drainage simulations (b). The top and bottom layer of the reservoirs are considered to be highly fractured, containing small scale variations in matrix block size below the size of a grid cell and are identified as MRDP regions. The large scale fractures in the central layer (DFM region) are modelled explicitly as 2D surfaces while the surrounding rock matrix is represented by volumetric elements (not shown here). Vertical wells have been implemented for water flooding simulations whereas horizontal wells were placed for the gas gravity drainage simulations. Water was injected with a constant rate of 1 m^3/day. The injection rate of gas for the gravity drainage simulations has been set to 3 m^3/day to overcome gravity forces. In both cases, the bottom hole pressure has been held constant at 2.0×10^7 Pa. See Table 5.6 and Table 5.9 for rock and fluid properties.

smaller than the size of the grid cells at the top and the bottom of the model. A central layer is included that contains three large scale fractures. The first two layers are identified as MRDP regions, the latter layer defines the DFM region where fractures are modelled explicitly as 2D surfaces surrounded by the volumetric finite elements that represent the matrix. The mesh consists of approximately 6900 finite elements and around 1400 finite volumes.

5.5.1 *Water Flooding Simulations NFR3 - Model Setup*

For the simulation of water flooding two vertical wells are used. The injector is located in the upper left model area, penetrating the upper MRDP region and slightly the DFM region. It operates at a constant injection rate of 1 m^3/day. The producer is located in the lower right model area, penetrating the lower MRDP region and the DFM region. The producer operates at a constant bottom hole pressure of 2.0×10^7 Pa. As before, a two-rate model ($N = 2$) is considered for the MRDP regions.

For the first MRDP case MR1, a characteristic length of $L_{c1} = 0.25$ m and porosity of $\phi_{m1} = 0.15$ is assigned to the first matrix sub-domain which comprises with 75% the major part of the stagnant matrix volume. Few smaller matrix blocks with a characteristic length of $L_{c2} = 0.15$ m and porosity of $\phi_{m2} = 0.23$ were introduced as the second sub-domain. For the second MRDP case MR2, also a characteristic length of $L_{c1} = 0.25$ m and porosity of $\phi_{m1} = 0.15$ is assigned to the first matrix sub-domain. The second sub-domain which represents 25% of the stagnant matrix volume is assumed to be composed of few larger matrix blocks with $L_{c2} = 1.25$ m and $\phi_{m2} = 4.0 \times 10^{-4}$. The averaged properties for the SRDP case SR1 are $L_c = 0.25$ m and $\phi_m = 0.2$ that represent an identical to the MRDP cases matrix volume (Table 5.7).

The fluid and rock properties for simulation NFR3 are listed in Table 5.6. The rock matrix in the MRDP regions is initially filled with 60% oil. The residual oil saturation was set to 0.422. In the flowing domain of the model (DFM region

and fracture part of MRDP regions), the initial water saturation and the residual oil saturation have been set to zero. The standard Brooks Corey model with quadratic relative permeability curves has been applied here.

Parameter		Value	Unit
density oil	ρ_o	850	kg/m^3
density water	ρ_w	1050	kg/m^3
viscosity oil	μ_o	5.0×10^{-3}	$Pa \cdot s$
viscosity water	μ_w	5.0×10^{-4}	$Pa \cdot s$
MRDP region			
effective fracture permeability	$K_{f,MRDP}$	1.0	D
fracture porosity	$\phi_{f,MRDP}$	0.01	$[-]$
matrix permeability	$K_{m,MRDP}$	10.0	mD
initial water saturation (flowing domain)	S_{wfi}	0.0	$[-]$
residual oil saturation (flowing domain)	S_{ofr}	0.0	$[-]$
initial water saturation (stagnant domain)	S_{wmi}	0.4	$[-]$
residual oil saturation (stagnant domain)	S_{omr}	0.422	$[-]$
DFM region			
fracture permeability	K_f	84.0	D
fracture porosity	ϕ_f	0.001	$[-]$
matrix permeability	K_m	10.0	mD
matrix porosity	ϕ_m	0.25	$[-]$
initial water saturation	S_{wi}	0.0	$[-]$
residual oil saturation	S_{or}	0.0	$[-]$

Table 5.6: Fluid and rock properties for water flooding simulations on the NFR3 model.

Simulation	L_{c1}	L_{c2}	ϕ_{m1}	ϕ_{m2}
SR1	0.25	–	0.2	–
MR1	0.25	0.15	0.15	0.23
MR2	0.25	1.25	0.15	4.0×10^{-4}

Table 5.7: Properties describing the matrix shape and volume in the DFM-SRDP and DFM-MRDP simulations on the NFR3 model (Table 5.1).

For simplicity, gravitational effects are considered in the flowing domain but are neglected in the stagnant domain of the MRDP regions by setting the ratio of capillary to gravitational forces r (Eq. 3.2) to zero such that T^{SI} (Eq. 3.15) is the transfer function during the simulation. Since $\Delta\rho = 200\ kg/m^3$ and the matrix blocks in the sub-domains of the MRDP regions are comparatively low,

setting $r = 0$ is a valid assumption. The parameters listed in Tables 5.6 and 5.7 and pore-network derived capillary pressure and relative permeability curves for Berea sandstones published in Oak (1990) and Valvatne and Blunt (2004) (Fig. 3.7) were used again to compute β^{SI} (Eq. 3.12). The resulting transfer rate coefficients are listed in Table 5.8.

Simulation	β_1^{SI} $[sec^{-1}]$	β_2^{SI} $[sec^{-1}]$
SR1	7.62×10^{-7}	-
MR1	1.02×10^{-6}	1.52×10^{-5}
MR2	1.02×10^{-6}	6.09×10^{-7}

Table 5.8: Transfer rate coefficients β_1^{SI} and β_2^{SI} for the DFM-MRDP water flooding simulations.

5.5.2 *Water Flooding Simulations NFR3 - Results*

Fig. 5.7 shows the propagation of water fronts through the flowing domain of the reservoir for the SRDP case SR1 and the MRDP case MR1 after 5 hours (a), 10 hours (b), 20 hours (c) and 30 hours (d) of water flooding. At the beginning of the simulation, for both cases SR1 and MR1, the water travels quickly through the upper MRDP region until it reaches the first major fracture of the DFM region. The flow is then conducted through this fracture, thereby connecting the lower MRDP region to the flow. Hence, preferential water flow through the first fracture and into the lower MRDP region causes early water breakthrough. Once both fractures of the DFM region contain water and connect the two MRDP regions, oil is left behind in the tight matrix of the DFM region. This trapped oil in the DFM region is only slowly recovered due to low pressure gradient and therefore low fluid velocities in these areas.

Prior to the water breakthrough, the flow behaviour in the SR1 and MR1 simulations does not differ significantly. The main difference is that the flowing domain of the MRDP regions in the case MR1 contains less water than the flowing domain of the MRDP regions in the case SR1 because of the increased fracture-matrix fluid exchange. Hence, more oil is released from the rock matrix in the

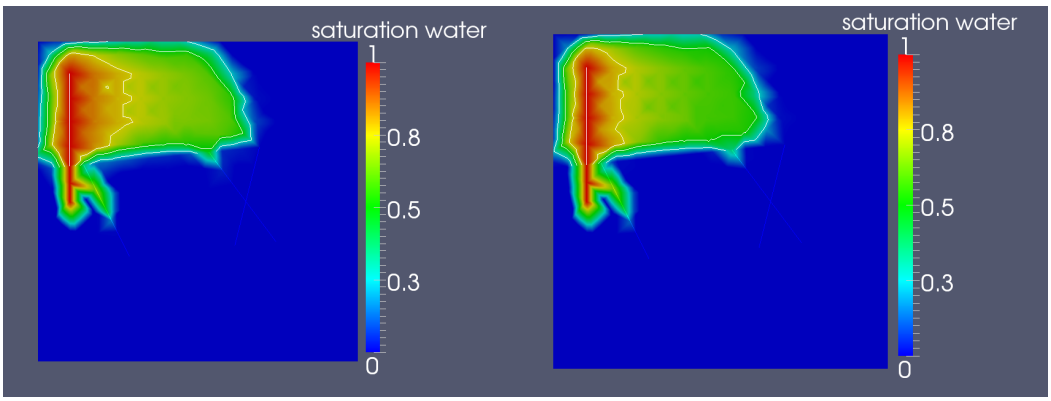

(a)

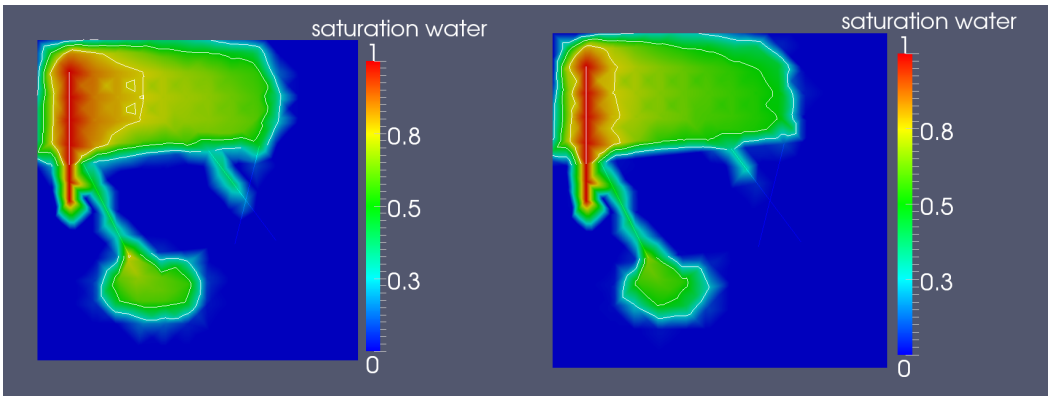

(b)

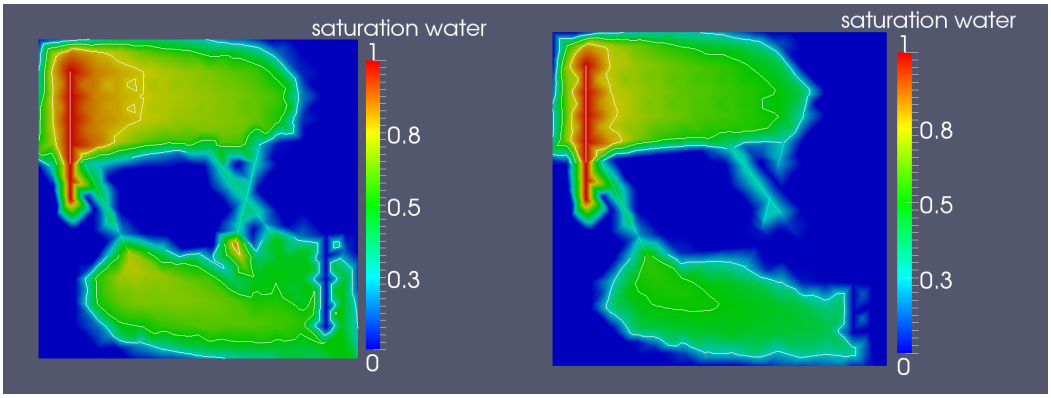

(c)

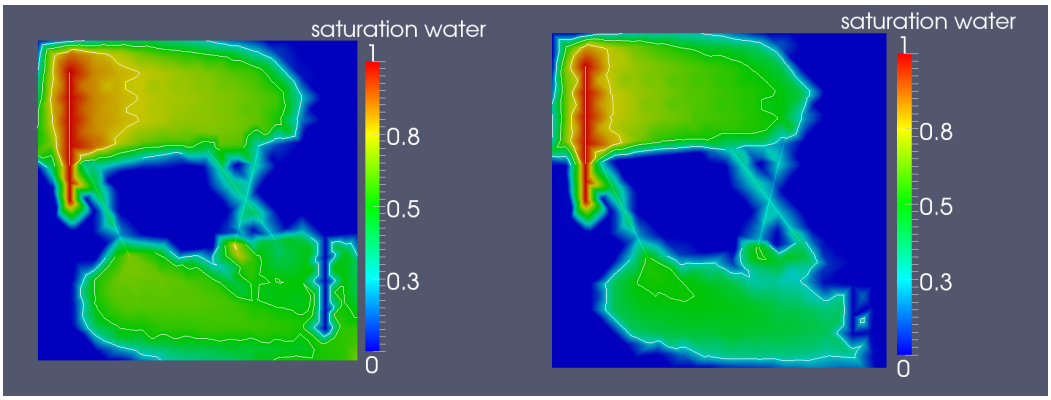

(d)

Figure 5.7: Water saturation distribution in the flowing domain for the MRDP case MR1 after 5 hours (a), 10 hours (b), 20 hours (c) and 30 hours (d) for the water flooding DFM-MRDP simulations. After early water breakthrough in the MRDP regions, water propagates into the fractures in the DFM region such that the oil in the DFM rock matrix becomes trapped. Some of this oil is later recovered due to capillary diffusion.

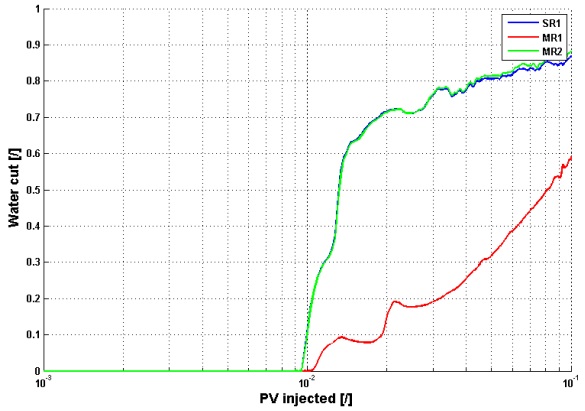

Figure 5.8: Water cut during the water flooding simulations using the DFM-MRDP approach. For rock and fluid properties see Table 5.6 and Table 5.7 and Fig. 5.6 and Table 5.1 for geometry information. The SRDP case SR1 and the MRDP case MR2 show essentially the same water cut. The water cut is much lower for the MRDP case MR1 where 25% of the matrix domain is assumed to contain smaller matrix blocks. This causes faster fracture-matrix transfer which reduces the water cut. The water cut is not monotonic because the conducting fractures deliver the water in pulses. The short term decline in water cut is caused by an increase in oil recovery due to spontaneous imbibition.

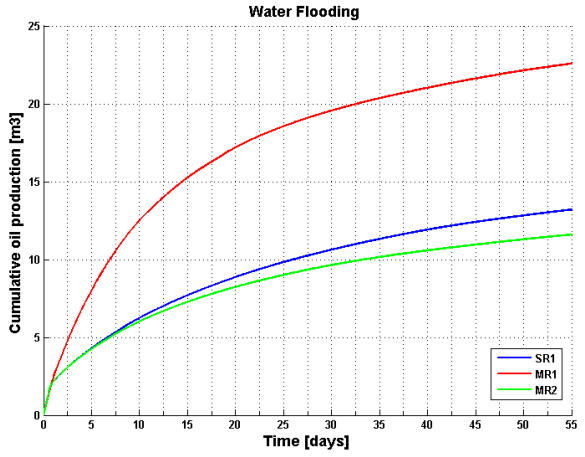

Figure 5.9: Predicted oil recovery for water flooding experiments using the DFM-MRDP approach. For rock and fluid properties see Table 5.6 and Table 5.7 and Fig. 5.6 and Table 5.1 for geometry information. MRDP case MR1 shows faster recovery compared to the MRDP case MR2 because MR1 contains a small value of smaller matrix blocks. The SRDP case SR1 predicts slightly higher recovery than case MR2 due to the averaging of transfer rates.

stagnant domain into the flowing domain in the case MR1.

In the case SR1, the quadratic relative water permeability and higher water saturations cause an acceleration of water propagation in the flowing domain. Water therefore reaches the second large fracture of the DFM region earlier than in the case MR1. This causes additional water to flow into the lower MRDP region and consequentially increases the water cut at the producer (Fig. 5.8). Water entering the second DFM fracture is notably delayed for the case MR1 which leads, additionally to the higher fracture-matrix transfer rates, to higher oil recovery (Fig. 5.9). The observed flow behaviour for the MRDP case MR2 is similar to the case SR1.

Water breakthrough occurs at the same time for all three cases MR1, MR2 and SR1 (Fig. 5.8). The key difference is however, that notably less water is produced for the MRDP case MR1. At this point, it should be noted that the water cut does not represent the cumulative water production but rather the fraction of water production with the total fluid production (water and oil) at a certain time. The arrival of additional water volumes at the producer well causes peaks in the water cut curves followed by a decline of water production for a short period of time. This decline results from the start of spontaneous imbibition process in the stagnant matrix domain which is caused by increase in water saturation in the flowing domain such that $T \neq 0$. An increase in transfer rates causes more oil to be transferred to the flowing domain and reduces the water production. As discussed above, additional water volume reaches the producer connecting the upper and lower MRDP region via the second DFM fracture. The arrival of the second water front at the producer is retarded for the MRDP case MR1 in comparison to the case SR1 and case MR2 because of higher transfer rate coefficients (Table 5.8). In the latter two cases water from the first and the second DFM fractures reached the producer almost simultaneously. Therefore only one major increase in the water production can be observed for the SR1 and MR2 simulations while for MR1 two discrete impulses emerged.

Fig. 5.9 shows the predicted cumulative recoveries of oil for all three water flooding simulations. A significantly higher recovery is observed for the sce-

nario where 25% of the rock matrix in the MRDP regions is assumed to contain smaller matrix blocks (case MR1). If the 25% of rock matrix are assumed to contain larger blocks, a lower final recovery is observed because the larger blocks release oil at a lower rate (case MR2). However, the flow pattern was comparable to the SRDP case SR1. This is consistent with previous results comparing SRDP and MRDP models for capillary driven fluid exchange between fractures and matrix (see Section 5.4). In general, the sub-grid heterogeneity in the MRDP regions affect the overall flow behaviour in the reservoir and, therefore, the production in a way that should not be neglected.

5.5.3 *Gas Gravity Drainage Simulations NFR4 - Model Setup*

To simulate gas gravity drainage, two horizontal wells were used in the model. The injector is located at the upper MRDP region and the producer is located at the lower MRDP region. As in the previous simulations the bottom hole pressure at the producer has been held constant at $2.0 \times 10^7\ Pa$. Initially, the reservoir is fully saturated with oil. Gas is then injected at a constant rate of 3.0 m^3/day in order to overcome the gravitational forces. To ensure that gravity is the driving force during the simulation a high density difference is used with a density of oil of 850 kg/m^3 and a gas density of only 200 kg/m^3. The viscosities are $5.0 \times 10^{-3}\ Pa \cdot s$ and $5.0 \times 10^{-5}\ Pa \cdot s$ for oil and gas, respectively (Table 5.9). An impermeable layer is added to prevent the leakage of gas across the top boundary of the model. This would correspond to a geological scenario of a cap rock.

Sub-grid heterogeneity in the MRDP regions was introduced by implementing two matrix sub-domains ($N = 2$). Again, a SRDP case SR1 is compared to two MRDP cases MR1 and MR2 with the same matrix volume. For case MR1, the first sub-domain contains matrix blocks with $L_1 = 1\ m$ and a porosity of $\phi_{m1} = 0.15$. The second sub-domain consists of smaller matrix blocks with $L_2 = 0.5\ m$ which have a porosity of $\phi_{m2} = 0.1$. The characteristic lengths for the MR2 case are $L_1 = 1.0\ m$ and $L_2 = 2.0\ m$ with the matrix porosities of $\phi_{m1} = 0.15$ and $\phi_{m1} = 0.025$, respectively. This corresponds to a scenario where the second sub-

domain consists of higher matrix blocks compared to the majority of the matrix volume. For the SRDP case, the heights of the matrix blocks are averaged as well as their porosities in the MRDP regions to $L = 2.0$ and $\phi_m = 0.1$, ensuring that the following relationship

$$\phi_{m_{SRDP}} L_{SRDP} = \sum_{k=1}^{N} \phi_{mk} L_k \tag{5.4}$$

is maintained. This way, the initial oil volume in the matrix remains the same and the simulation results for the oil recovery are comparable (Table 5.10).

Parameter		Value	Unit
density oil	ρ_o	850	kg/m^3
density gas	ρ_g	200	kg/m^3
viscosity oil	μ_o	5.0×10^{-3}	$Pa \cdot s$
viscosity gas	μ_g	5.0×10^{-5}	$Pa \cdot s$
MRDP region			
effective fracture permeability	$K_{f,MRDP}$	1.0	D
fracture porosity	$\phi_{f,MRDP}$	0.01	$[-]$
matrix permeability	$K_{m,MRDP}$	10.0	mD
initial gas saturation (fractures)	S_{gfi}	0.0	$[-]$
residual oil saturation (fractures)	S_{ofr}	0.0	$[-]$
initial gas saturation (matrix)	S_{gmi}	0.0	$[-]$
residual oil saturation (matrix)	S_{omr}	0.12	$[-]$
DFM region			
fracture permeability	K_f	84	D
fracture porosity	ϕ_f	0.001	$[-]$
matrix permeability	K_m	10.0	mD
matrix porosity	ϕ_m	0.25	$[-]$
initial gas saturation	S_{gi}	0.0	$[-]$
initial oil saturation	S_{or}	0.0	$[-]$

Table 5.9: Fluid and rock properties for gravity drainage simulations

Using the capillary pressure curve from Pedrera et al. (2002) and properties from Table 5.9, the ratio of capillary to gravitational forces is always larger than 1.0 (Table 5.11). Hence, the fluid exchange between the stagnant and flowing domain is gravity dominated and T_k^{GD} (Eq. 3.27) are the transfer functions used during the simulation. Setting the constant a to 2.0 in Eq. 3.25 resulted in

Simulation	L_1	L_2	ϕ_{m1}	ϕ_{m2}
SR1	2.0	–	0.1	–
MR1	1.0	0.5	0.15	0.1
MR2	1.0	2.0	0.15	0.025

Table 5.10: Properties describing the matrix shape and volume in the DFM-SRDP and DFM-MRDP simulations on the NFR4 model (Table 5.1).

Simulation	r_1	r_2	S^*_{g1}	S^*_{g2}
SR1	2.47	-	0.47	-
MR1	2.47	1.23	0.46	0.07
MR2	2.47	4.93	0.46	0.67

Table 5.11: Capillary-gravity ratio and the maximum gas saturation for the MRDP regions for gas gravity drainage simulations on the NFR4 model.

$\beta^{GD} = 1.78 \times 10^{-7}\ sec^{-1}$ for the average transfer rate coefficient for the SRDP case SR1. For the MRDP simulation MR1 one yield $\beta_1^{GD} = 2.38 \times 10^{-7}\ sec^{-1}$ and $\beta_2^{GD} = 7.15 \times 10^{-7}\ sec^{-1}$ for the first and second matrix sub-domain. Note that transfer rates for MR2 are the same as for MR1 although the height of the matrix blocks is different (Table 5.12). This is because the gravity drainage transfer rates β^{GD} are scaling with $(\phi L)^{-1}$ and for this particular case it is $\phi_{2,MR1} L_{2,MR1} = \phi_{2,MR2} L_{2,MR2}$. The difference in the recovery will therefore not be controlled by the rate of the fluid exchange but rather by the maximum possible gas saturation S^*_g in the matrix blocks. The capillary rise H will be the same for all scenarios. The maximum gas saturation therefore depends on the height of the matrix blocks. The larger the characteristic length L is, the more gas can enter the matrix. Subsequently, more oil can be drained from the matrix. The computed maximum gas saturations for the three simulations are listed in Table 5.11.

Simulation	$\beta_1^{GD}\ [sec^{-1}]$	$\beta_2^{GD}\ [sec^{-1}]$
SR1	1.78×10^{-7}	-
MR1	2.38×10^{-7}	7.15×10^{-7}
MR2	2.38×10^{-7}	7.15×10^{-7}

Table 5.12: Transfer rate coefficients β_1^{GD} and β_2^{GD} for the DFM-MRDP gas gravity drainage simulations.

5.5.4 *Gas Gravity Drainage Simulations NFR4 - Results*

Fig. 5.10 shows the gas distribution in the flowing and the stagnant domains of the reservoir after 10 hours (left), 15 hours (middle) and 20 hours (right) for MR1 case. The gas moves downwards through the upper MRDP region in a stable front until it reaches the DFM region. Here, gas flow is channelled through the fractures in the DFM region, connecting the upper and the lower MRDP regions. As soon as gas enters the second MRDP region, the transfer function T^{GD} becomes larger than zero in the gas saturated parts of the lower MRDP region such that drainage of oil from the matrix blocks commences. After gas breakthrough has occurred (Fig. 5.11), gravity forces cause gas to accumulate in higher regions of the model. Thus, most oil is recovered from the upper MRDP region followed by the lower MRDP region. The gas hardly enters the matrix in the DFM region as the gas preferably flows through areas that are already saturated with gas and hence have a high mobility. Thus the oil in the rock matrix of the DFM region is trapped until majority of the oil is drained from the MRDP regions.

Fig. 5.12 shows the cumulative oil recovery due to gravity drainage for the SRDP case SR1 and MRDP cases MR1 and MR2. Since gas breakthrough occurred simultaneously in all three cases, recovery is the same at early time. The recovery behaviour differs only slightly at late time where a different behaviour compared to the water flooding simulations can be observed. The final recovery is higher for the case MR2 where few higher matrix blocks were assumed to be present in the MRDP regions. Recovery is lowest for the case MR1 where smaller matrix blocks are assumed to be located in the MRDP regions. The rates at which the gas drains the oil from the matrix blocks is similar in all cases such that only the maximum gas saturation S_g^*, i.e. the height of the matrix blocks, controls the overall recovery. This observation is consistent with the results from Di Donato et al. (2007), who found that the transfer rate coefficient β^{GD} is less sensitive to the sub-grid heterogeneities of the matrix shapes compared to the transfer rate coefficient β^{SI}.

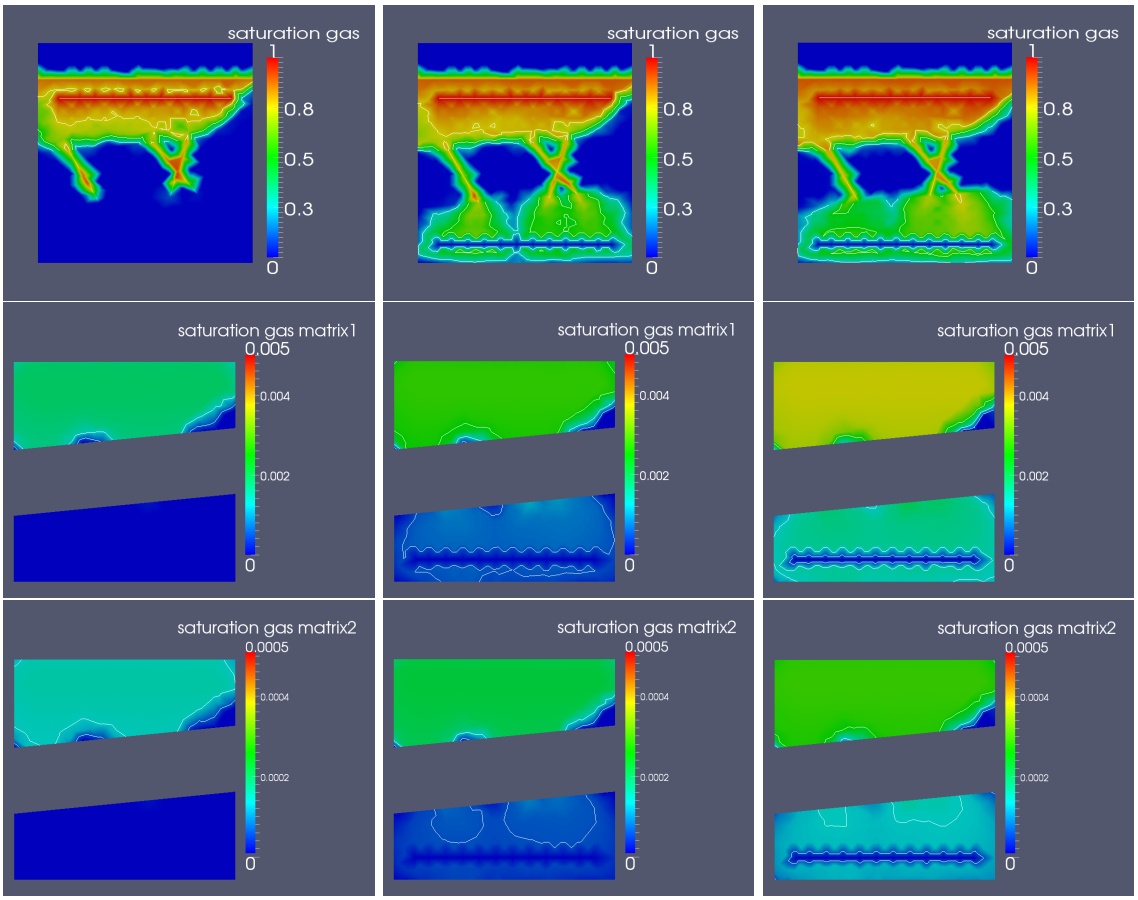

Figure 5.10: Gas saturation after 10 hours (left), 15 hours (middle) and 20 hours (right) for DFM-MRDP gas gravity drainage simulation. The top row shows gas saturation in the flowing domain for case MR1 (Table. 5.10). The middle and bottom rows show the gas saturation in the first and second matrix sub-domains of the MRDP regions, respectively. The injected gas propagates downwards through the upper MRDP region until it reaches the fractures of the DFM area. Here, the gas flows through the high permeable DFM fractures and connects the lower MRDP region with the upper MRDP region. As soon as the gas arrives in the lower MRDP region, the transfer function T^{GD} is larger zero and oil begins to drain from the stagnant matrix.

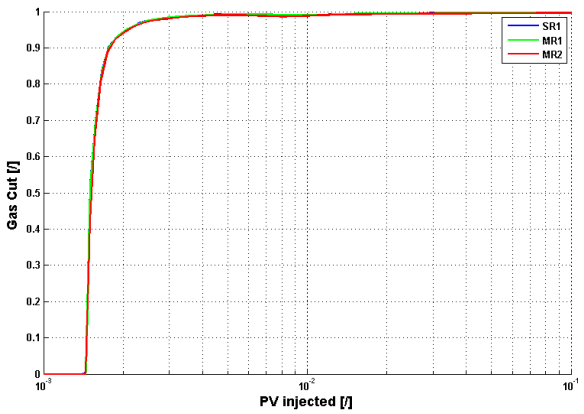

Figure 5.11: Gas cut at the producer. Note that the gas cut is identical for all three gas gravity drainage experiments.

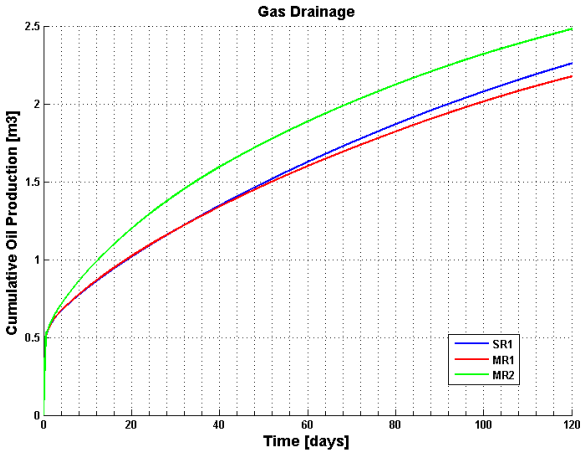

Figure 5.12: Cumulative oil recovery for SRDP (SR1) and MRDP (MR1,MR2) simulations during gas gravity drainage in the NFR4. Recovery differs only at late time after the gas breakthrough. The MRDP case MR2 predicts the highest recovery because MR2 contains small volume of high matrix blocks from which more oil can be drained.

5.5.5 *Discussions of DFM-MRDP Simulation Results*

Combining the DFM and MRDP approaches for flow simulation leads to fundamentally different simulation results compared to a classical SRDP approach when modelling large-scale and small-scale heterogeneities in NFR. Complex flow patterns developed that depend on the small-scale heterogeneity in the MRDP regions, which affected the ultimate oil recovery. The oil recovery was more affected when capillary forces dominated in the highly fractured MRDP regions compared to the gas gravity drainage case where small-scale heterogeneities introduced by different matrix block sizes affect only oil recovery at late time. This is because the transfer rate coefficient for spontaneous imbibition is more sensitive to the characteristic length of the matrix block sizes as it scales with $\beta^{SI} \approx 1/L_c^2$. In comparison, the transfer rate coefficient for gravity drainage β^{GD} scales with $1/L$. The complex flow patterns also affected the water production. Non-monotonic water cut curves including peaks and slight declines were observed. This behaviour was only observed if imbibition in the MRDP regions was fast enough to sufficiently delay the propagation of the water front in the flowing domain. If the injected fluid (water or gas) propagates faster or more stable in the flowing domain such that the fluid reaches the entire area of the producer at the same time, production of the injected fluid increases rapidly without occurrence of peaks.

5.6 OPERATOR SPLITTING ERROR ANALYSIS

The operator splitting employed in the DFM-MRDP approach solves the pressure and saturation equations sequentially using implicit time-stepping, followed by the update of the saturation values due to fracture-matrix transfer in the MRDP regions. Whereas the error due to numerical dispersion was discussed in Chapter 2.3.1 for the Buckley-Leverett problem, this section concentrates on the numerical error introduced by the operator splitting when it is applied to more complex geometries and flow systems. For this purpose, water flooding simulations in the model NFR3 (Fig. 5.9) are performed using different model time steps $\Delta t = \Delta t_{PresEq} \in [5\ sec,\ 15\ sec,\ 30\ sec,\ 45\ sec,\ 1\ min,\ 5\ min,\ 10\ min]$. This implies that the pressure field, and thus the velocity field as well, but also the saturation values in the stagnant domain and flowing domain due to the fracture-matrix transfer in the MRDP regions were updated after each time step Δt_{PresEq}. The time step for implicit solving of the advection equation Δt_{SatEq} is set such that it always satisfies the CFL condition (CFL multiplier = 1). Hence, the numerical dispersion of the saturation front is constant and small, but the error caused by the operator splitting may increase for larger model time steps because multiple solutions at sub-timesteps are necessary for the saturation equation if $\Delta t_{SatEq} < \Delta t_{PresEq}$. In contrast to Chapter 2.3.1, an analytical solution cannot be provided. Simulation results using a very small time step of $\Delta t = \Delta t_{PresEq} = 5\ sec$ are therefore used as a reference solution.

5.6.1 *Model Setup*

The same fluid and rock properties as in the simulations discussed in Section 5.5 were assigned to model NFR3 (Table 5.6 and 5.7). I emphasise that gravitational effects are considered but capillary effects in the flowing domain of the MRDP and DFM regions are neglected based on the assumptions that viscous and capillary forces dominate here. The impact of capillary forces in the flowing domain is subject to future work. In the stagnant domain of the MRDP regions capillary forces are taken into account by the fracture-matrix transfer rate coefficients (see

Chapter 3). Those are listed in Table 5.8 for different small-scale heterogeneities cases SR1, MR1 and MR2.

Previously, non-monotonic water cut curves were observed in simulations with comparatively low fluid velocities in the flowing domain, i.e. when the injected fluid has enough time to interact with the rock matrix in the stagnant domain and therefore to affect the entire flow pattern before water breakthrough occurs (Fig. 5.8). To analyse if this non-monotonic behaviour is physical or caused by a numerical error introduced in the operator splitting, two cases are considered for model NFR3: One where the fluid velocities are high and one where the velocities are low. To obtain high and low average fluid velocities, the pressures at the injector and producer where set accordingly to obtain steep and low pressure gradients in the reservoir. The pressure gradients were held constant during the simulations.

For the low velocity case, the pressure at the injector was fixed to $2.005 \times 10^7\ Pa$ and at the producer to $2.0 \times 10^7\ Pa$. This results in an initial average velocity of $v = 4.64 \times 10^{-7}\ m/s$ and a CFL time step of 352 sec. During the simulation, when the injected water reaches the fractures in the DFM region, the average fluid velocity increases to $v = 1.39 \times 10^{-5}\ m/s$, such that the CFL time step decreases to 12 sec. The time step for the reference solution is with $\Delta t = 5\ sec$ below the smallest CFL time step, hence we always find $\Delta t_{PresEq} = \Delta t_{SatEq}$ and therefore the effective CFL multiplier is ≤ 0.42. For the simulations with time step $\Delta t > 5\ sec$ one finds that $\Delta t_{PresEq} > \Delta t_{SatEq}$ holds for the majority of the simulation time and therefore $\Delta t >$ CFL time step if the CFL multiplier equals 1.

For the high velocity case the pressure at the injector was fixed to $2.05 \times 10^7\ Pa$ and to the producer at $2.0 \times 10^7\ Pa$. This results in an initial average velocity of $v = 4.64 \times 10^{-6}\ m/s$ and a CFL time step of 35 sec; this CFL time step is a factor 10 smaller than the CFL time step for the low velocity case. The average fluid velocity increases to $v = 1.39 \times 10^{-4}\ m/s$ as soon as the water front reaches the fractures in the DFM region. The CFL time step decreases then to 6 sec. However, the time step for the reference solution at $\Delta t = 5\ sec$ remains smaller than the CFL time step during the entire simulation. Thus, one always has $\Delta t_{PresEq} = \Delta t_{SatEq}$

and the effective CFL multiplier is ≤ 0.83. For the simulations with time step of $\Delta t > 5$ *sec* one always finds that $\Delta t_{PresEq} > \Delta t_{SatEq}$ and multiple solutions at sub-timesteps are necessary for the saturation equation.

5.6.2 *Simulations Results*

Figure 5.13 shows the predicted oil production (a) and the water cut (b) for the cases SR1, MR1 and MR2 using four different model time steps of $\Delta t = 5$ *sec*, 30 *sec*, 1 *min* and 10 *min*. The oil recovery but also the water cut results are comparable to the water flooding results presented in Section 5.5, where the highest oil recovery and the latest water breakthrough occurs when smaller matrix block sizes are assumed to be present in the MRDP regions (i.e. case MR1). If part of the MRDP regions is assumed to be less fractured (case MR2), the oil recovery after a model time of 10 days is lower and the water cut is higher compared to the case where all matrix block sizes are assumed to be uniform (case SR1). The non-monotonic behaviour of the water cut appears for all selected time-steps, which strongly indicates that this is a physical behaviour and not caused by a numerical error due to the operator splitting.

Although, increasing the model time step did not lead to a distinguishable difference between the simulation results because the recovery and water cut curves coincide (Fig. 5.13), calculating the L_2 error norm allows a further analysis of how the numerical error changes as the time-step is increased. Since an analytical solution cannot be defined in this case, the L_2 error is defined as follows:

$$\left\| F_{\Delta t > 5s}(t) - F_{\Delta t = 5s}(t) \right\|_2, t \in [0, 10\ days] \tag{5.5}$$

where F is the oil recovery or the water cut. Fig. 5.14 indicates that the L_2 norm, and hence the numerical error due to operating splitting, increases with increasing time step. The error in the L_2 norm for the oil recovery remains almost constant around $1\% - 4\%$ for $\Delta t \leq 60$ *sec*. For such small time steps, an acceleration in the Central Processing Unit (CPU) time of a factor 2 for the case SR1, of

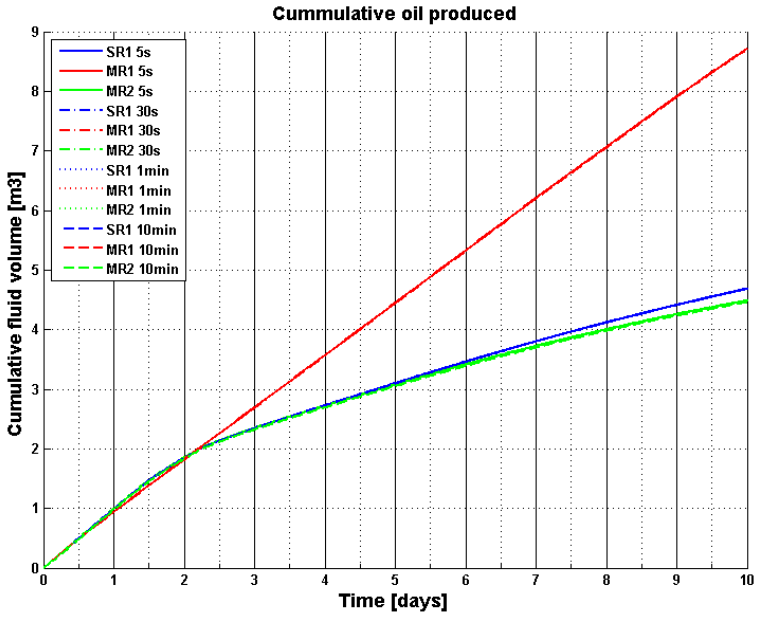

(a)

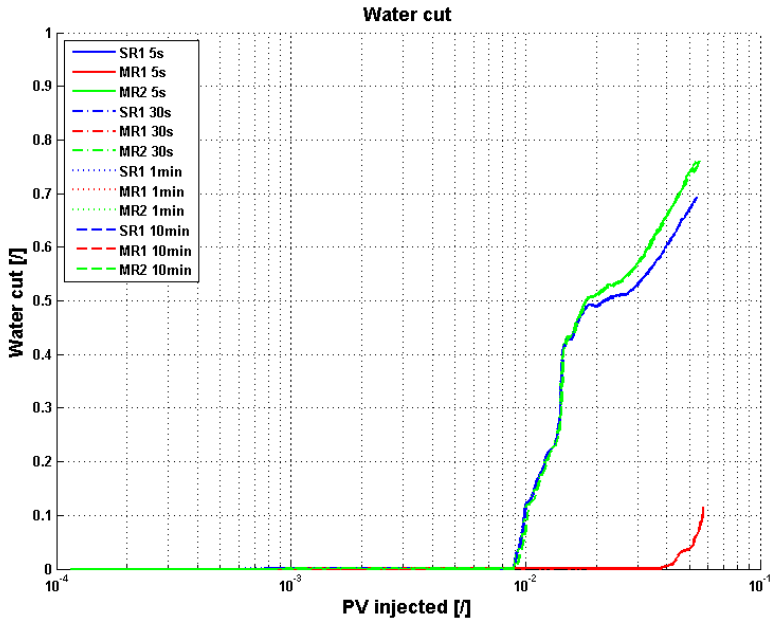

(b)

Figure 5.13: Predicted oil recovery (a) and water cut (b) for the low velocity case using different time steps for a model time of 10 days. No recognizable differences are noticeable in the recovery and water cut profiles and the simulation results are comparable to the results shown in Section 5.5.

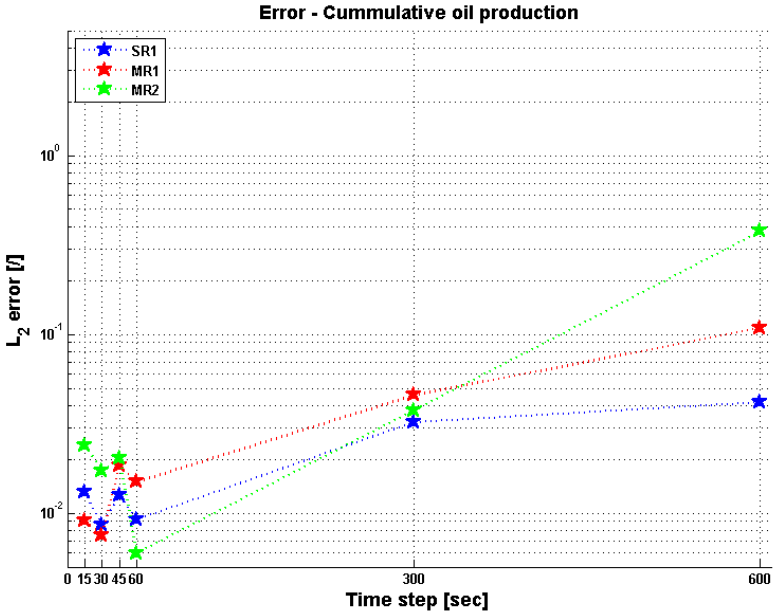

(a)

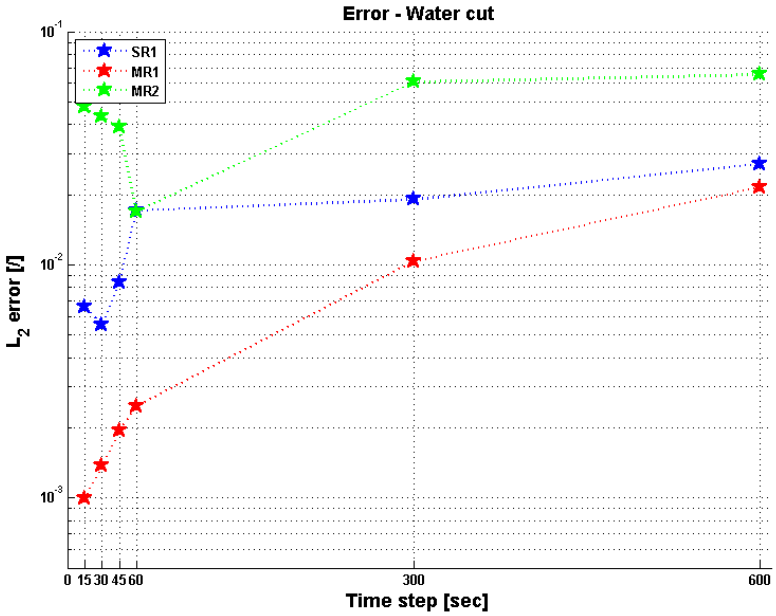

(b)

Figure 5.14: Numerical error caused by operator splitting measured in the L_2 norm for the predicted oil recovery (a) and water cut (b) for different model time steps Δt for the low velocity case in log 10 scale. The error in L_2 norm for the predicted oil recovery describes a similar trend for cases SR1, MR1 and MR2. The error remains nearly constant for small time steps of $\Delta t \leq 5$ CFL time step but increases significantly for larger time steps. The error for the water cut remains at the same order of magnitude for the cases SR1 and MR2 for all time steps, but increases by one order of magnitude in case MR1 if the time step is increased.

a factor 10 for the case MR1 and of a factor 4 for the case MR2 can be observed (Table 5.13). For larger time steps, the error in the L_2 norm increases by one order of magnitude to $5\% - 15\%$. The error in L_2 norm for the water cut remains under 10% for all time steps in model NFR3. It should be noted that for case MR1, i.e. where water breakthrough occurs significantly later compared to cases SR1 and MR2, the error in L_2 norm is remarkably small for time steps of $\Delta t \leq 30$ *sec*; the error remains below 1%. It then increases by one order of magnitude to approximately 3% but still remains lower than the error for the cases SR1 and MR2.

time step [sec]	5	15	30	45	60	300	600
SR1	23.56 h	10.76 h	7.01 h	5.82 h	10.70 h	3.55 h	3.61 h
MR1	51.23 h	10.95 h	7.18 h	5.57 h	5.25 h	3.85 h	3.75 h
MR2	23.97 h	11.14 h	7.26 h	5.95 h	5.36 h	3.56 h	3.59 h

Table 5.13: CPU time for the low velocity case simulations for a model time of 10 days.

In contrast to the low velocity case, a noticeable difference in predicted oil recovery and water cut is observed for $\Delta t = 10$ *min* compared to the reference solution with $\Delta t = 5$ *sec*. Larger time steps lead to higher oil recovery and higher increase in the water cut (Fig. 5.15). Accordingly, the error in the L_2 norm increases as well, indicating that the numerical error that is introduced by the operator splitting becomes more significant. The error for the predicted oil recovery reaches over 100% for case MR1 if $\Delta t \geq 5$ *min*. However, the error in the oil recovery remains below 10% if $\Delta t \leq 30$ *sec*. For Δt below 30 seconds, the CPU time reduces by a factor of 5 for cases SR1 and MR1 and by a factor of 2 for the case MR2. Although the CPU time generally decreases with increasing time step (at the expense of a less accurate simulation), the exact measure as to how much the CPU time decreases can be difficult to establish. If $\Delta t_{SatEq} < \Delta t_{PresEq}$, the fraction $n = \frac{\Delta t_{PresEq}}{\Delta t_{SatEq}}$ is not always an integer number. This implies that after $\lfloor n \rfloor$ iterative solutions of the advection equation one last solution has to be found with $\Delta t_{SatEq} = \Delta t_{PresEq} - \lfloor n \rfloor \Delta t_{SatEq}$. This time step might be very small, but will still demand the CPU time for building and solving the linear equation system.

The previous two test cases used a fixed CFL multiplier of 1. To study the effect of sub-time stepping during the solution of the advection equation on

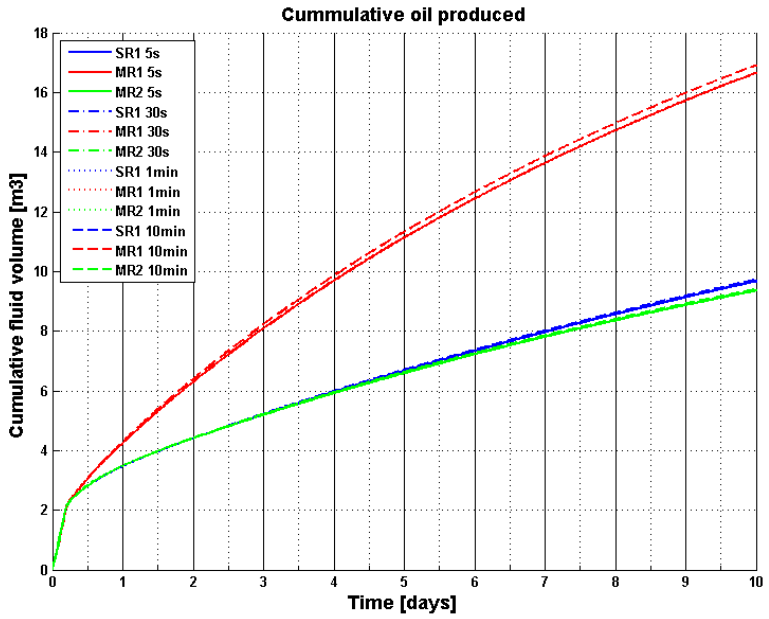

(a)

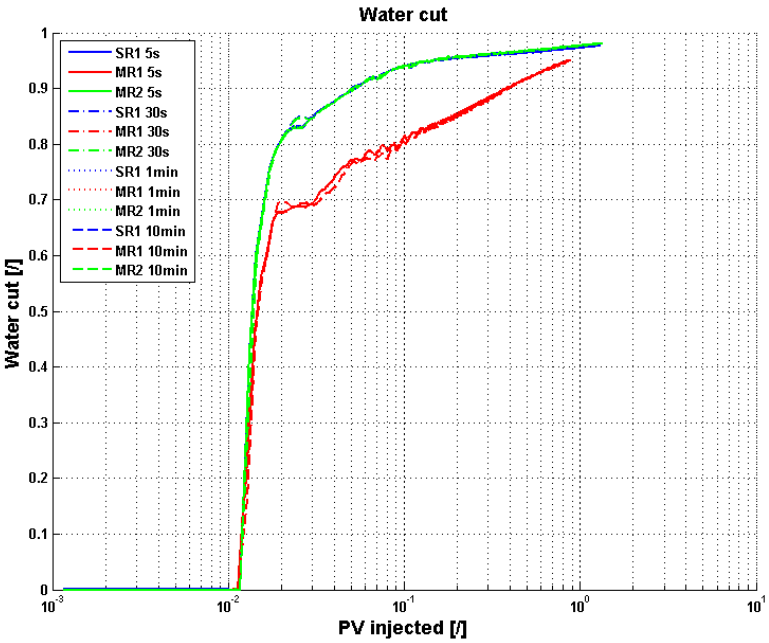

(b)

Figure 5.15: Predicted oil recovery (a) and water cut (b) for the high velocity case using different time steps. High fluid velocities in the flowing domain cause earlier water breakthrough and steeper water cuts compared to the low velocity case. Noticeable numerical error occurs for time steps of $\Delta t \geq 10$ where the oil recovery is slightly overpredicted.

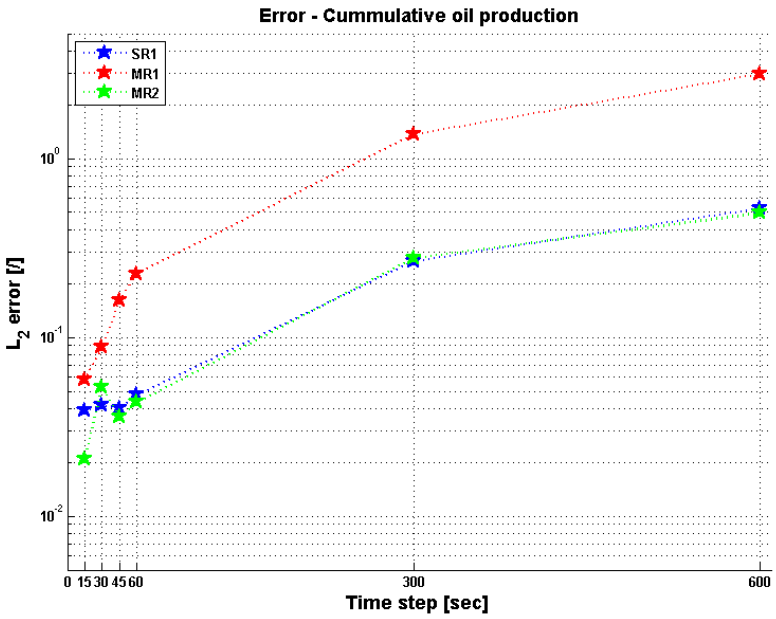

(a)

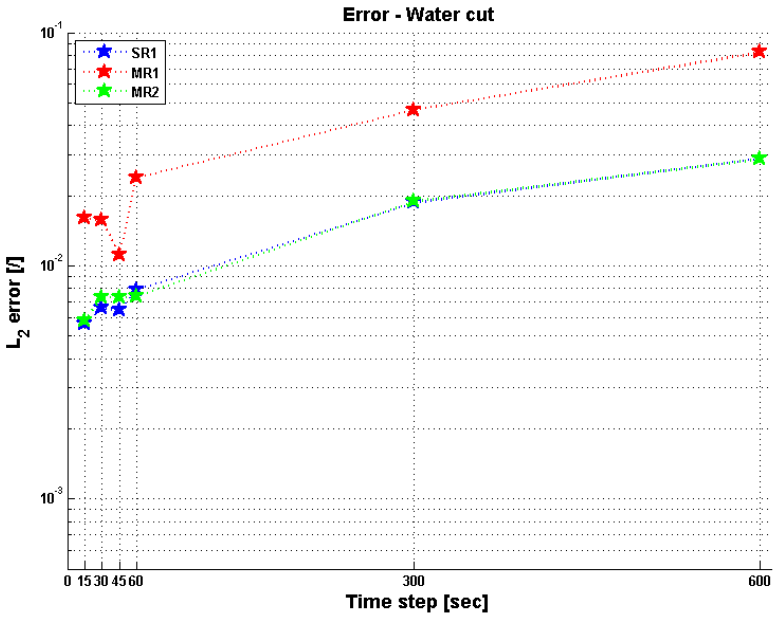

(b)

Figure 5.16: Numerical error due to operator splitting measured in L_2 norm for the predicted oil recovery (a) and water cut (b) for different model time steps Δt for the high velocity case in log 10 scale. The error increases with increased simulation time step but still remains low for small time steps $\Delta t \leq 30$.

time step [sec]	5	15	30	45	60	300	600
SR1	51.66 h	13.98 h	11.24 h	9.82 h	9.63 h	8.22 h	7.91 h
MR1	57.48 h	15.06 h	11.88 h	10.73 h	10.24 h	9.04 h	8.59 h
MR2	24.54 h	14.15 h	11.18 h	9.81 h	9.48 h	7.66 h	7.52 h

Table 5.14: CPU time for the high velocity case simulations for a model time of 10 days.

the overall error that is caused by the operator splitting, a further study was conducted where the CFL multiplier varied throughout the simulation. The CFL multiplier was chosen during each time step to ensure that one always obtains $\Delta t_{PresEq} = \Delta t_{SatEq}$ for the entire simulation.

Although the CFL multiplier is now ≥ 1, the error measured in L_2 norm still is of the same order of magnitude as the error for low velocity case where the CFL multiplier was fixed to 1 (Fig. 5.17). This shows the advantage of using an implicit solver for the advection equation: The solution still converges if the CFL multiplier is larger than 1 because the overall error is dominated by the operator splitting, not the numerical dispersion of the saturation front. Using the same time steps for the solution of the pressure and saturation equations, i.e. avoiding sub-time stepping, has the further advantage that the CPU time is reduced (see Table 5.15) since just one iterative solution of the saturation equation is needed during each update of the pressure field and therefore building and solving the linear system of equations, and evaluating the Jacobian, for a large number of small time-steps can be avoided.

time step [sec]	30	45	60
SR1	4.38 h	2.69 h	2.16 h
MR1	4.27 h	5.92 h	2.23 h
MR2	4.43 h	2.84 h	2.22 h

Table 5.15: CPU time for the low velocity case simulations for a model time of 10 days where the CFL multiplier was variable such that one obtains $\Delta t_{PresEq} = \Delta t_{SatEq}$ for the entire simulation.

5.6.3 *Discussions of Error Analysis*

The analysis of the numerical error presented in this section extended the error analysis for numerical dispersion in Section 2.3.1. It was shown, that by allowing overstepping for the saturation equation, the overall error is dominated by the error due to operator splitting. That is because the overstepping was comparatively small. For example, for a time step of $\Delta t = 60$ *sec*, one obtains CFL multiplier ≤ 5; in this case, the numerical error due to numerical dispersion was

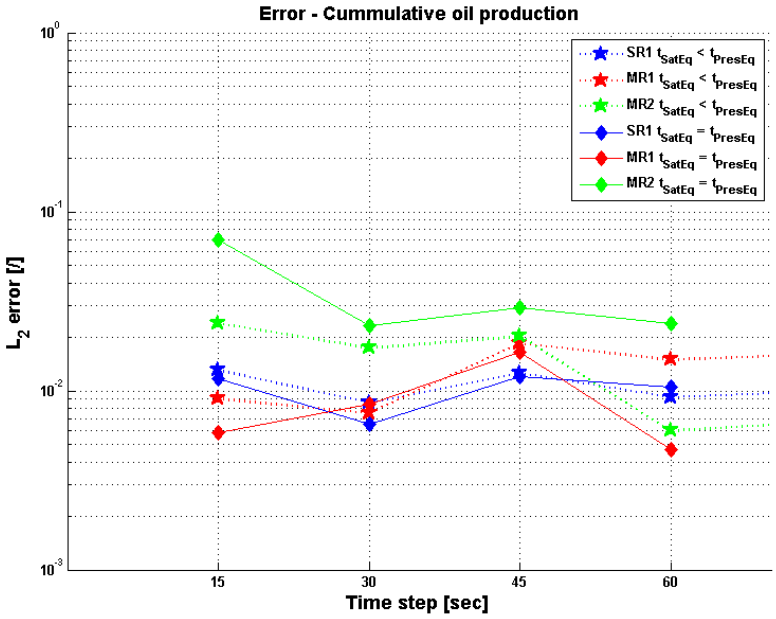

(a)

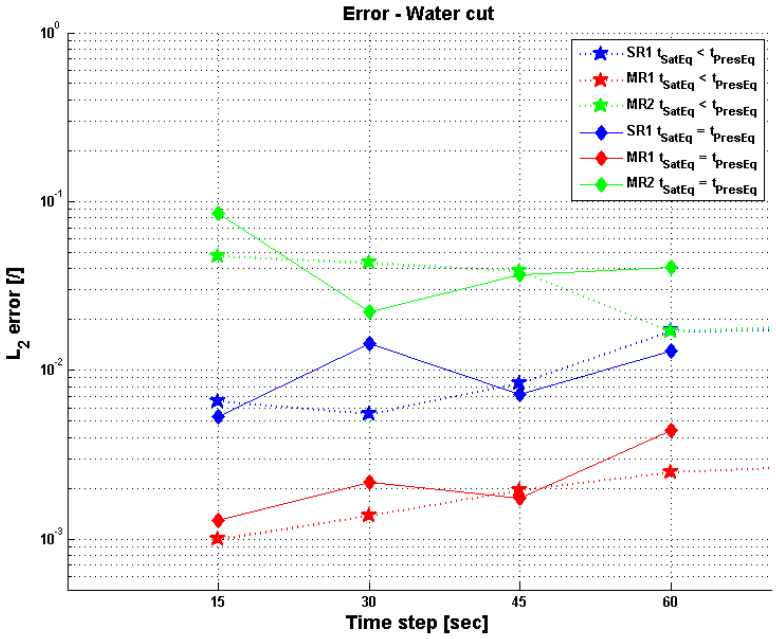

(b)

Figure 5.17: Numerical error due to operator splitting measured in L_2 norm for the predicted oil recovery (a) and water cut (b) for different model time steps Δt for the low velocity case in log 10 scale. In contrast to the error analysis shown in Fig. 5.14 and Fig. 5.16, the CFL multiplier was variable such that one always obtains $\Delta t_{PresEq} = \Delta t_{SatEq}$ for the emtire simulation.

negligible (Fig. 2.7 and Fig. 2.9). It should be noted that the analysis of the numerical error was performed on a particular model and may vary for different geometries.

5.7 SUMMARY

In this chapter, the multi-scale heterogeneities inherent to naturally fractured reservoirs are represented by the DFM-MRDP model. The division of the reservoir model into Discrete Fracture and Matrix (DFM) and Multi-Rate Dual-Porosity (MRDP) regions enables to combine two state of the art simulation approaches in one reservoir simulator. Fluid flow in regions with faults, fracture corridors, large faults or sparsely fractured regions is modelled using the DFM approach such that flow in both, fractures/faults and matrix can be simulated explicitly. This approach is physically more appropriate. On the other hand, regions with intense fracturing and well-connected fracture networks are modelled by the MRDP approach. Here, upscaled fracture properties are computed and fluid flow is simulated only in the flowing fracture domain. Fluid exchange between fractures and matrix is computed using the previously described MRDP approach (Chapter 4). Allowing for multiple transfer rates to be present is crucial because the rock matrix can rarely be considered homogeneous. Even small variations in rock (or fluid properties) can lead to differences by orders-of-magnitude in transfer rates and hence to fundamentally different recovery behaviours, especially if capillary forces dominate.

Proof of concept simulations demonstrated that the DFM-MRDP approach can model the complex behaviour of two-phase flow in naturally fractured reservoirs well and significant differences compared to DFM-SRDP models can be observed. It was studied how large fractures in the DFM region connect highly fractured MRDP regions such that complex flow patterns develop, possibly leaving large values of oil behind that is trapped in the rock matrix. The change of the main flow paths over the field life can be analysed due to the interplay of complex reservoir geometry and capillary or gravitational forces. An analysis of the nu-

merical error due to the operator splitting showed that the overall solution error is dominated by the operator splitting and not the numerical dispersion. However, this error leads to negligible variations in the water cut and oil production curves because of the relatively weak coupling between the pressure and saturation equation if viscous forces dominate. The numerical error can be controlled by choosing an appropriate global time-step. Further work is needed to explore if a predictor-corrector scheme or a global iteration (e.g. a Picard iteration) would allow us to choose arbitrarily large global time steps despite using a sequential solution of the pressure and saturation equation.

It is important to emphasise that the DFM-MRDP model presented here is not restricted to unstructured grids and can be applied to any structured grid simulator. The advantage of unstructured hybrid grid though is that large-scale fractures and faults as well as other geometrically complex geological bodies can be readily modelled. Attempting to model such geometries using corner point grids with two-point flux approximation can result in significant numerical error (Aavatsmark, 2002; Lie et al., 2012).

6

SUMMARY, CONCLUSIONS AND FUTURE WORK

6.1 SUMMARY AND CONCLUSIONS

Naturally Fractured Reservoirs (NFR) hold about half of the world's remaining oil reserves and are typically very heterogeneous. NFR are also important for many other subsurface engineering applications, including (nuclear) waste storage, CO_2 sequestration, groundwater aquifers, and geothermal energy extraction. They contain faults, fracture corridors, large fractures but also many small-scale fractures as well as heterogeneous rock matrix. Multi-phase flow in NFR is strongly influenced by this multi-scale heterogeneity. Therefore, accurate conceptual models that reliably quantify fluid flow in the fracture and fluid exchange between fracture and matrix are needed to forecast oil recovery and optimise production in fracture-dominated and fracture-assisted reservoirs.

Discrete Fracture and Matrix (DFM) models provide an accurate approach for NFR modelling as they use fully unstructured grids to resolve the fractures and other complex geological structure explicitly and solve the underlying physics of fluid flow in fractures and matrix simultaneously. However, the high computational cost of the DFM approach makes full field simulations intractable. On the other hand, the classical Dual-Porosity (DP) model has low computational cost but lacks accuracy when simulating multi-phase flow in NFR as they oversimplify the fracture network geometry and the key physics of fracture-matrix fluid exchange. DP model application is also restricted to certain areas of a NFR, since the model assumes that the underlying fracture network must be well connected. The objective of this work was to improve the performance of the DFM approach

in terms of computational cost and the performance of the DP model in terms of physical accuracy when modelling fracture-matrix fluid exchange. Ultimately, the improved DFM and DP models are combined to utilise the benefits of both approaches when simulating multi-phase flow in NFR. All developments and implementations were made in the research-grade reservoir simulator Complex Systems Modelling Platform (CSMP++), which employs unstructured finite element and finite volume methods. The key outcomes of this thesis are as follows:

- In Chapter 2, the Implicit Pressure Implicit Saturation (IMPIS) approach in a DFM model was implemented. It was demonstrated that the IMPIS approach compared to the Implicit Pressure Explicit Saturation (IMPES) approach applied to heterogeneous media has similar accuracy but is potentially faster if the contrast in fluid velocities is large.

- In Chapter 3, I introduced the classical Single-Rate Dual-Porosity (SRDP) model using transfer functions that are based on analytical solutions for spontaneous imbibition and gravity drainage. It was shown that pseudo steady-state shape factors, which account for the quasi radial propagation of the saturation fronts due to the saturation gradients, gave the best predictions of fracture-matrix mass transfer due to spontaneous imbibition.

- The SRDP model was then extended in Chapter 4 to the Multi-Rate Dual-Porosity (MRDP) model. The effect of small-scale heterogeneities in the rock matrix on oil recovery predictions was studied by varying the matrix permeability and matrix block sizes. The multi-rate behaviour observed in the fine-grid simulations was modelled adequately with the MRDP approach. The SRDP model usually predicted significantly faster recoveries than the MRDP model and yielded reasonable approximation of oil recoveries only when the multiple transfer rates were similar.

- In Chapter 5, the research-grade reservoir simulator CSMP++ was extended by combining the models introduced in Chapter 2, Chapter 3 and Chapter 4 to the DFM-MRDP model. The DFM-MRDP approach was tested using idealised NFR models that contain large fractures above the simulation grid cell size and small scale fractures below the grid cell size. It was demon-

strated how the DFM-MRDP approach models the complex flow behaviour caused by the multi-scale heterogeneity inherent to NFR.

6.2 FUTURE WORK

The key contribution of this thesis was the development and implementation of the DFM-MRDP approach. However, there are many areas where this approach should be improved in future work. Some of them are listed below.

- In this thesis, I considered only incompressible, immiscible and isothermal two-phase flow in presence of a third, immobile phase. However, in reality if three phases are present in a reservoir, they are likely to be all mobile and can interact with each other (e.g. gas can dissolve in the oil and water phase as the pressure increases). Modelling three phase flow is of a great importance for real hydrocarbon reservoirs, for example if they have a gas cap or if Enhanced Oil Recovery (EOR) such as Water-Alternating-Gas (WAG) injection should be simulated. Therefore, the DFM-MRDP model should be extended to a BlackOil simulator in the first instance, including PVT look-up tables. The first attempts to implement such a model in CSMP++ are currently underway.

- The MRDP transfer functions, which were presented in this thesis, model capillary and gravity driven fracture-matrix fluid exchange separately depending on the ratio of capillary to gravitational forces. Two other processes, i.e. fluid transfer due to fluid expansion and due to diffusion are still neglected. These transfer functions can be extended to a general transfer function as proposed by Lu et al. (2008) through substitution of their spontaneous imbibition term

$$\sqrt{\frac{K}{\phi}}\frac{\sigma}{\sqrt{\mu_w \mu_o}}\frac{1}{L_c^2}, \tag{6.1}$$

with the transfer rate coefficient based on the analytical solution for spontaneous imbibtion

$$\left(\frac{2A}{\phi L_c}\right)^2. \tag{6.2}$$

This transfer function would account for all four principal mechanism of fracture-matrix mass transfer and would remain applicable to arbitrary fluid and rock properties.

- In Chapter 3, it was shown that the exponential model of Aronofsky for modelling spontaneous imbibition in a DP model (Eq. 3.14) slightly underpredicts the recovery at early time but it provides a good approximation of the late time behaviour (i.e. for $t > t^*$). On the other hand, the analytical solution for spontaneous imbibition (Eq. 3.8) is valid only for $t < t^*$ where it yields the exact result of oil recovery during spontaneous imbibition. Therefore, a better prediction of oil recovery can be achieved by combining the analytical solution with the Aronofsky model:

$$R = \begin{cases} R_{analytical} & t \leq t^*, \\ R_{Aronofsky} & t > t^* \quad . \end{cases} \tag{6.3}$$

  In that way, the analytical solution would not only provide the transfer rate coefficient for Eq. 3.14 but also predict the exact recovery R at early times.

- The MRDP model gives only an evolution of the average wetting fluid saturation in the matrix block. If hysteresis effects should be considered during a simulation, the knowledge of the spatial distribution of the wetting and the non-wetting fluids is also important. Incorporating a Multiple Interacting Continua (MINC) model, where each matrix block itself is divided into different matrix-sub regions, each having its own pressure and saturation value, could provide a solution to this problem. Such a DFM-MRDP-MINC model would require additional transfer functions to compute the fluid exchange between the fractures and the outer matrix domains and subsequently the transfer between the outer and inner matrix domains. It is expected that through the preservation of the gradients in the matrix saturations the early time recoveries can be modelled since steep saturation gradients accelerate recovery at early time.

A

IMPLEMENTATION

A.1 IMPIS ON UNSTRUCTURED FE GRID

Closed source code CSMP++, free for academics
Compilable with:

g++ (4.6.4 linux)
clang++ (3.4.1 linux)
icpc (13.1 Linux)
VS2012 (Visual Studio 11, Windows)
VS2013 (Visual Studio 12, Windows)

Managed repository at MU Leoben
Contact Julian Mindel (julian.mindel@gmail.com) for obtaining the license

A.1.1 *Pseudocode for Implicit Solution for Transport Equation*

Listing 1: SolveTransportEquationImplicitly

```
NW_maxIt = 5;
LS_maxIt = 5;
NWiter = 1;
LSiter = 1;
NW_residual_target = 1.0 × 10^-3;
LS_residual_target = 0.99*NW_residual_target;
residual = 1.0;
residual_previous = 1.0;

//Newton loop
S_init = S_α^t;

while(residual > NW_residual_target && NWiter < NWmaxIt)
{
        for (each finite volume)
        {
                Calculate F(S_init); // accumulate residual vector
                Calculate F'(S_init); // accumulate Jacobian matrix
                Add source term q
        }
        // Solve equation system with algebraic multi-grid solver
        ΔS_NW = −F(S_init)/F'(S_init);

        //Line Search loop
        LScontinue = true;
        while(LScontinue && LSiter < LSmaxIt )
        {
                S_α^{t+Δt} = S_α^t + ΔS_NW 2^{−LSiter};
                Calculate residual = ||F(S_α^{t+Δt})||_2;

                if (residual > residual_previous && LSiter > 1)
                {
                        S_α^{t+Δt} = S_α^t + ΔS_NW 2^{−(LSiter−1)};
                        Calculate residual = ||F(S_α^{t+Δt})||_2;
                        LScontinue = false;
                }
                residual_previous = residual;
                LSiter++;
        }
        S_init = S_α^{t+Δt};
        NWiter++;
}

return S_α^{t+Δt};
```

A.2 ANALYTICAL SOLUTION FOR SPONTANEOUS IMBIBITION

Matlab code available upon request:

```
function SpontaneousImbibition( time )
%SPONTANEOUSIMBIBITION Summary
% Calculates the analytical solution for spontaneous imbibition for
% water-wet rocks and compares with experimental data
%
% INPUT: time [hours] (is converted to SI unit [s] later in script)
%
% The Eq numbers in the comments refer to
% Schmid, K. S., & Geiger, S. (2013). Universal scaling of spontaneous imbibition
% for arbitrary petrophysical properties: Water-wet and mixed-wet states and
% Handy's conjecture. Journal of Petroleum Science and Engineering, 1-18.
% doi:10.1016/j.petrol.2012.11.015
%
% Calculates among others:
% the Dispersion coefficient D(Sw) (Eq. 6)
% the fractional flow including capillarity F(Sw) (Eq. 11)
% the constant A (Eq. 8)
% the volumetric inflow Q(t) (Eq 9)
% the water saturation profile (x,Sw) (Eq 12)
% the time t_star until the analytical solution is valid (Eq 15)
% the transfer rate coefficient tau_c which can be used for DP simulations(Eq 20)
% the exponential recovey function after Aronofsky(1958) (Eq 28)
% ...
```

A.3 ECLIPSE CODE FOR SPONTANEOUS IMBIBITION EXPERIMENTS

A.3.1 *.data file*

```
– Three Dimensional Counter-current Imbibition
– WATER-WET Barea sandstone
– BASE CASE (Kr & Pc from Bourbiaux, B., & Kalaydjian, F. (1990). doi:10.2118/18283-PA)
– Matrix Swi = SWC = 40 %
– Matrix Snr = SNR = 42.2 %
– rock cubes surrounded by fractures(infinite volume)saturated with water, all faces open for imbibition
–
–
DEBUG
0 0 0 1 0 0 1 0 0 1 /

RUNSPEC ================================
TITLE
« Spontaneous Imbibition »
–
DIMENS
– NX   NY   NZ
102   102   102 /

– "ONLY OIL AND WATER PRESENT"
OIL
WATER
– "USING LAB UNITS"
LAB
– "ASSUME TWO REGIONS WITH THE SAME FLUID PROPERTIES"
EQLDIMS
2 /
```

```
TABDIMS
2  1  15  15  2 /
START
18 'FEB' 2014 /
FMTOUT
FMTIN
UNIFOUT
UNIFIN

GRID ==================================
– Corner point grid imported from Petrel
– Increased fracture porevolume assigning MULTPV=1.0E+006 to the fracture region to approximate S_wf = 1.0 constant
INCLUDE
'includes/grid.inc' /

– Isotropic permeability

COPY
PERMX PERMY /
PERMX PERMZ /
/

PSEUDOS
RPTGRID
COORD /

INIT
EDIT

PROPS =================================
– "USE SIMILAR FLUID PROPERTIES FOR TWO REGIONS"
DENSITY
– Densities @ surface condition lb/ft
```

```
– Oil    Water    GAS
0.788    1.012    7.0E-04 /

GRAVCONS
0.0/

– Rock compressibility
–     P    Cr
–    —-    —
ROCK
– Pref, atma    Cf, 1/atm
100.00    .30E-04 /

– PVT data for dead oil
– REF    PRESS    -BO    -COMPRESSIBILITY    -VISCOSITY    -VISCOSIBILITY
–    —-    —-    —
PVCDO
100    1.0    0.0e-5    5.0 0.0 /

– PVT data for water
–    P    Bw    Cw    Vis
–    —-    —-    —    —
PVTW

100.0    1.00    0.00E-06    0.5    0.0 /

INCLUDE
'includes/satfunc_Oak.inc' /

REGIONS ==================================
– " DEFINE TWO REGIONS FOR MATRIX (R-2) AND FRACTURE (R-1)"
INCLUDE
'includes/region.inc' /
```

```
RPTREGS
0 1 0 0 0 0 0 0 0 0 /
SOLUTION ==================================

INCLUDE
'includes/solution.inc' /

RPTSOL
1 1 1 0 0 0 0 2 1 0 0 /
SUMMARY ===================================
-- OUTPUT IN EXCEL FORMAT
EXCEL
-- SHOW AVERAGE OIL SATURATION IN REGIONS
ROSAT
1 2 /
-- SHOW AVERAGE WATER SATURATION IN REGIONS
RWSAT
1 2 /
-- SHOW AVERAGE OIL PRESSURE IN REGIONS
RPR
1 2 /
-- SHOW OIL EXCHANGE BETWEEN REGIONS
ROFTL
2 1 /
/

RPTONLY
SCHEDULE ==================================
TSTEP
600*120
/
END
```

A.3.2 *include files*

The grid.inc, region.inc and solution.inc files are too large to be included in this thesis and are available upon request.

A.3.2.1 *satfunc_Oak.inc*

SWOF

– fracture region: linear relperms & no capillary pressure

– Sw Krw Kro Pcw-o

0.0 0.0 1.0 0.0

1.0 1.0 0.0 0.0 /

– matrix region: Kr & Pc from Bourbiaux, B., & Kalaydjian, F. (1990). doi:10.2118/18283-PA

0.4 0 1 3.4

0.41 1.49E-08 0.919545271 0.266999466

0.42 7.41E-07 0.853394333 0.189457853

0.44 3.91E-05 0.730508295 0.136760631

0.46 0.000397478 0.615225436 0.114510221

0.47 0.000960057 0.559439333 0.107347973

0.49 0.004042798 0.450627004 0.096980128

0.50 0.007386653 0.397362557 0.093070844

0.51 0.012742176 0.344743546 0.089738294

0.52 0.02096145 0.292704328 0.086855826

0.54 0.050629663 0.190157871 0.082100381

0.55 0.075130486 0.139566987 0.080108943

0.56 0.108682752 0.089385225 0.078318562

0.57 0.153737944 0.039583971 0.076698219

0.578 0.2 0.0 0.075507563

/

A.4 PSEUDOCODE FOR DFM-MRDP

Listing 2: DFM-MRDP workflow for simulation of NFR: Part 1 preparing the reservoir simulation model

```
// Identify DFM and MRDP regions
if (Large scale fractures and faults or sparse fractured areas)
        DFM region;

else // areas of well connected fracture networks with small scale fractures
{
        MRDP region;
}

// Upscaling and definition of sub-grid heterogeneities
Upscale fracture properties of the MRDP region;
Identify N matrix sub-domains of the MRDP region by its heterogeneity;

// Build geometry of the NFR, modelling different geological features using a CAD
    software e.g. Rhinoceros®
Model DFM regions with beds, fractures and faults;
Model MRDP regions including large-scale heterogeneity e.g. beds;
Place wells;

// Mesh computation
Generate an unstructured volumetric mesh with a mesh generation software e.g. ANSYS
     ICEM CFD®;

//Populate mesh with parameters (CSMP++ code)
for each node and element in DFM region
{
        Store fracture/fault and matrix properties;
        Set initial and boundary conditions;
}

for each node and element in MRDP region
{
        Store upscaled fracture properties;
        Store N sets of matrix rock properties (virtual matrix cells);
        Set initial and boundary conditions;
}

//Definition of flowing and stagnant domains
Properties of flowing domain = DFM region properties + upscaled fracture properties
     of MRDP region;
Properties of stagnant domain = N sets of matrix rock properties of MRDP region;
```

Listing 3: DFM-MRDP workflow for simulation of NFR: Part 2 simulating fluid flow

```
for each node j in MRDP region
{
        Compute and store ratio of capillary to gravitational forces r^j;
        if (r^j > 1)
                for k = 1 to N
                Compute and store the transfer rate coefficients β_k^{GD,j};
        else
                for k = 1 to N
                Compute and store the transfer rate coefficients β_k^{SI,j};
}
// Reservoir flow simulation
for each time step
{
        if (rock or fluid properties in the MRDP region changed)
        {
                for each node j in MRDP region
                {
                        Update ratio of capillary to gravitational forces r^j;
                        if (r^j > 1)
                                for k = 1 to N
                                Update transfer rate coefficients β_k^{GD,j};
                        else
                                for k = 1 to N
                                Update transfer rate coefficients β_k^{SI,j};
                }
        }
        else
        {
                Solve pressure equation in flowing domain;
                for each node i // entire model
                {
                        Update pressure values p^i;
                }

                Solve saturation equation implicitly in flowing domain;
                for each node i // entire model
                {
                        Update saturation values S_w^i; S_nw^i = 1.0 − S_w^i;
                }

                for each node j of MRDP region
                {
                        // Update saturations in flowing and stagnant domain using
                            transfer functions
                        if (r^j > 1)
                                T^{GD,j} = Σ T_k^{GD,j} (β_k^{GD,j}, S_w^j, S_wm^j);
                                (S_w^j, S_wm^j) = F (T^{GD,j});
                        else
                                T^{SI,j} = Σ T_k^{SI,j} (β_k^{SI,j}, S_w^j, S_wm^j);
                                (S_w^j, S_wm^j) = F (T^{SI,j});
                }

        }
}
```

BIBLIOGRAPHY

I. Aavatsmark. An introduction to multipoint flux approximations for quadrilateral grids. *Computational Geosciences*, 6(3-4):405–432, 2002.

A. S. A. Abushaikha and O. R. Gosselin. Matrix-Fracture Transfer Function in Dual-Medium Flow Simulation: Review, Comparison, and Validation. In *SPE 113890 - presented at the 2008 SPE Europec/EAGE Annual Conference and Exhibition held in Rome, Italy, June*, 2008.

S. Agar, S. Geiger, S. Matthai, R. Alway, S. Tomas, A. Immenhauser, R. Shekhar, J. Paul, G. Benson, Z. Karcz, and L. Kabiri. The Impact of Hierarchical Fracture Networks on Flow Partitioning in Carbonate Reservoirs: Examples Based on a Jurassic Carbonate Ramp Analog from the High Atlas, Morocco. In *Proceedings of SPE Annual Technical Conference and Exhibition*. Society of Petroleum Engineers, 2010.

M. Ahmed Elfeel, G. Couples, S. Geiger, and J. Ma. Upscaled multi-phase flow properties of fracture corridors. In *Proceedings of SPE Caspian Carbonates Technology Conference*, pages 8–10. Society of Petroleum Engineers, 2010.

M. Ahmed Elfeel, M. Jamal, C. Enemanna, D. Arnold, and S. Geiger. Dfn upscaling on history matching and prediction of naturally fractured reservoirs. *SPE-164838, SPE Europec/EAGE Annual Conference, London, United Kingdom*, 2013.

M. Ahmed Elfeel, S. Agada, C. Maier, and S. Geiger. Integrating discrete fracture models for static and dynamic calibration of fractured reservoirs. *76th EAGE Conference and Exhibition, Amsterdam, Netherlands*, June 2014.

R. Annewandter, I. Main, and S. Geiger. High-Resolution Numerical Simulations of Capillary Trapping of CO2 in Fractured Formations. In *Proceedings of SPE Reservoir Characterisation and Simulation Conference and Exhibition*, number September, pages 16–18. Society of Petroleum Engineers, 2013.

J. S. Aronofsky, L. Masse, and S. G. Natanson. A model for the mechanism of oil recovery from the porous matrix due to water invasion in fractured reservoirs. *Petroleum Transactions, AIME*, 213:17–19, 1958.

A. Aydin. Fractures, faults, and hydrocarbon entrapment, migration and flow. *Marine and Petroleum Geology*, 17:797–814, 2000.

K. Aziz and A. Settari. *Petroleum reservoir simulation*, volume 476. Applied Science Publishers London, 1979.

T. Babadagli and C. U. Hatiboglu. Analysis of counter-current gas-water capillary imbibition transfer at different temperatures. *Journal of Petroleum Science and Engineering*, 55(3-4):277–293, 2007.

G. I. Barenblatt, I. P. Zheltov, and I. N. Kochina. Basic concepts in the theory of seepage of homogeneous liquids in fissured rocks. *J. Appl. Math. Mech., Engl.Transl.*, 24:1286–1303, 1960.

B. L. Beckner, H. M. Chan, A. E. McDonald, S. O. Wooten, and T. A. Jones. Simulating Naturally Fractured Reservoirs Using a Subdomain Method. *Proceedings of SPE Symposium on Reservoir Simulation*, 1991.

H. S. Behbahani, G. Di Donato, and M. J. Blunt. Simulation of counter-current imbibition in water-wet fractured reservoirs. *Journal of Petroleum Science and Engineering*, 50(1):21–39, 2006.

M. Belayneh. Palaeostress orientation inferred from surface morphology of joints on the southern margin of the bristol channel basin, uk. *Geological Society, London, Special Publications*, 231(1):243–255, 2004.

B. Berkowitz. Characterizing flow and transport in fractured geological media: A review. *Advances in Water Resources*, 25(8-12):861–884, 2002.

B. Berkowitz, O. Bour, P. Davy, and N. Odling. Scaling of fracture connectivity in geological formations. *Geophysical research letters*, 27(14):2061–2064, 2000.

T. I. Bjørnara and S. A. Mathias. A pseudospectral approach to the McWhorter and Sunada equation for two-phase flow in porous media with capillary pressure. *Computational Geosciences*, 17(6):889–897, 2013.

M. J. Blunt. Flow in porous media - pore-network models and multiphase flow. *Current Opinion in Colloid & Interface Science*, 6(3):197–207, 2001.

M. J. Blunt, M. D. Jackson, M. Piri, and P. H. Valvatne. Detailed physics, predictive capabilities and macroscopic consequences for pore-network models of multiphase flow. *Advances in Water Resources*, 25(8-12):1069–1089, 2002.

M. J. Blunt, B. Bijeljic, H. Dong, O. Gharbi, S. Iglauer, P. Mostaghimi, A. Paluszny, and C. Pentland. Pore-scale imaging and modelling. *Advances in Water Resources*, 51:197–216, 2013.

C. E. Bond, R. Wightman, and P. S. Ringrose. The influence of fracture anisotropy on CO2 flow. *Geophysical Research Letters*, 40(7):1284–1289, 2013.

H. Boro, G. Bertotti, and N. J. Hardebol. Distributed fracturing affecting isolated carbonate platforms, the latemar platform natural laboratory (dolomites, north italy). *Marine and Petroleum Geology*, 40:69–84, 2013.

B. Bourbiaux. Fractured Reservoir Simulation: a Challenging and Rewarding Issue. *Oil & Gas Science and Technology - Rev. IFP*, 65(2):227–238, 2010.

B. Bourbiaux and F. Kalaydjian. Experimental study of cocurrent and countercurrent flows in natural porous media. *SPE Reservoir Engineering*, 5(3), 1990.

S. E. Buckley and M. C. Leverett. Mechanism of fluid displacement in sands. *Trans. Am. Inst. Min. Metall. Pet. Eng.*, 146:107–116, 1942.

D. A. Budd and H. L. Vacher. Matrix permeability of the confined Floridan Aquifer, Florida, USA. *Hydrogeology Journal*, 12(5):531–549, 2004.

Z. Chen. *Reservoir simulation: mathematical techniques in oil recovery*, volume 77. Siam, 2007.

J. R. Christensen, E. H. Stenby, and A. Skauge. Review of WAG field experience. *SPE Reservoir Evaluation & Engineering*, 4(2):97–106, 2001.

M. A. Christie. Upscaling for Reservoir Simulation. *Journal of Petroleum Technology*, 48(11):1004–1010, 1996.

D. Civile, M. Zecchin, E. Forlin, F. Donda, V. Volpi, B. Merson, and S. Persoglia. CO2 geological storage in the Italian carbonate successions. *International Journal of Greenhouse Gas Control*, 19:101–116, 2013.

K. H. Coats. Implicit compositional simulation of single-porosity and dual-porosity reservoirs. *Proceedings of SPE Symposium on Reservoir Simulation*, pages 239–275, 1989.

L. Cosentino, Y. Coury, J. M. Daniel, E. Manceau, C. Ravenne, P. Lingen, J. Cole, and M. Sengul. Integrated Study of a Fractured Middle East Reservoir with Stratiform Super-K Intervals - Part 2: Upscaling and Dual Media Simulation. In *Proceedings of SPE Middle East Oil Show*. Society of Petroleum Engineers, 2001.

G. J. Crutchley, C. Berndt, S. Geiger, D. Klaeschen, C. Papenberg, I. Klaucke, M. J. Hornbach, N. L. B. Bangs, and C. Maier. Drivers of focused fluid flow and methane seepage at south Hydrate Ridge, offshore Oregon, USA. *Geology*, 41(5):551–554, 2013. ISSN 0091-7613.

L. Denoyelle, C. Bardon, and E. Couve de Murville. Interpretation of a CO2/N2 injection field test in a moderately fractured carbonate reservoir. *SPE Reservoir Engineering*, pages 220–226, 1988.

B. Dershowitz, P. LaPointe, T. Eiben, and L. Wei. Integration of Discrete Feature Network Methods With Conventional Simulator Approaches. *SPE Reservoir Evaluation & Engineering*, 3(2):165–170, 2000.

W. Dershowitz, R. Ambrose, D.-H. Lim, and M. Cottrell. Hydraulic Fracture and Natural Fracture Simulation for Improved Shale Gas Development. *AAPG Annual Convention and Exhibition, Houston, Texas, USA*, (April), 2011.

G. Di Donato, Z. Tavassoli, and M. J. Blunt. Analytical and numerical analysis of oil recovery by gravity drainage. *Journal of Petroleum Science and Engineering*, 54(1-2):55–69, 2006.

G. Di Donato, H. Lu, Z. Tavassoli, and M. J. Blunt. Multirate-transfer dual-porosity modeling of gravity drainage and imbibition. *SPE Journal*, 12(1):77–88, 2007.

F. Doster, E. Keilegavlen, and J. M. Nordbotten. A Robust Implicit Pressure Explicit Mass Method for Multi-Phase Multi-Component Flow Including Capillary Pressure And Buoyancy. In *Computational Models for CO2 Geo-sequestration & Compressed Air Energy Storage*, chapter 7. 2013. ISBN 978-1138015203.

L. J. Durlofsky. A Triangle Based Mixed Finite Element - Finite Volume Technique for Modeling Two Phase Flow through Porous Media. *Journal of Computational Physics*, 105(2):252–266, 1999.

R. Fucik, J. Mikyska, M. Benes, and T. H. Illangasekare. An improved semi-analytical solution for verification of numerical models of two-phase flow in porous media. *Vadose Zone Journal*, 6(1):93–104, 2007.

L. S. K. Fung. Simulation of block-to-block processes in naturally fractured reservoirs. *Society of Petroleum Engineers*, 6(4):477–484, 1991.

B. D. M. Gauthier, M. Garcia, and J. M. Daniel. Integrated Fractured Reservoir Characterization : A Case Study in a North Africa Field. (August):24–25, 2002.

S. Geiger, S. Roberts, S. K. Matthäi, C. Zoppou, and a. Burri. Combining finite element and finite volume methods for efficient multiphase flow simulations in highly heterogeneous and structurally complex geologic media. *Geofluids*, 4:284–299, 2004.

S. Geiger, T. Driesner, C. A. Heinrich, and S. K. Matthai. Multiphase Thermohaline Convection in the Earth's Crust: I. A New Finite Element - Finite Volume Solution Technique Combined With a New Equation of State for NaCl-H2O. *Transport in Porous Media*, 63(3):399–434, 2006.

S. Geiger, Q. Huangfu, F. Reid, S. Matthai, D. Coumou, M. Belayneh, C. Fricke, and K. S. Schmid. Massively Parallel Sector Scale Discrete Fracture and Matrix Simulations. *Proceedings of SPE Reservoir Simulation Symposium*, 2009a.

S. Geiger, S. Matthäi, J. Niessner, and R. Helmig. Black-Oil Simulations for Three-Component, Three-Phase Flow in Fractured Porous Media. *SPE Journal*, 14(2), 2009b.

S. Geiger, M. Dentz, and I. Neuweiler. A novel multirate dual-porosity model for improved simulation of fractured and multiporosity reservoirs. *SPE Journal*, 18 (4):670–684, 2013.

H. H. Gerke. Preferential flow descriptions for structured soils. *Journal of Plant Nutrition and Soil Science*, 169(3):382–400, 2006.

J. R. Gilman. An efficient finite-difference method for simulating phase segregation in the matrix blocks in double-porosity reservoirs. *SPE Reservoir Engineering*, 1(4):403–413, 1986.

J. R. Gilman and H. Kazemi. Improvements in simulation of naturally fractured reservoirs. *Society of Petroleum Engineers Journal*, 23(4), 1983.

J. R. Gilman and H. Kazemi. Improved Calculations for Viscous and Gravity Displacement in Matrix Blocks in Dual-Porosity Simulators (includes associated papers 17851, 17921, 18017, 18018, 18939, 19038, 19361 and 20174). *Journal of Petroleum Technology*, 40(1), 1988.

B. Gong and L. J. Durlofsky. SPE 102491 An Upscaling Procedure for Constructing Generalized Dual-Porosity / Dual-Permeability Models F rom Discrete Fracture Characterizations. 2006.

T. Graf and R. Therrien. Coupled thermohaline groundwater flow and single-species reactive solute transport in fractured porous media. *Advances in Water Resources*, 30(4):742–771, 2007.

R. Haggerty and S. M. Gorelick. Multiple-rate mass transfer for modeling diffusion and surface reactions in media with pore-scale heterogeneity. *Water Resources Research*, 31(10):2383–2400, 1995.

R. Haggerty, S. W. Fleming, L. C. Meigs, and S. A. McKenna. Tracer tests in a fractured dolomite: 2. analysis of mass transfer in single-well injection-withdrawal tests. *Water Resources Research*, 37(5):1129–1142, 2001.

J. Hagoort. Oil Recovery by Gravity Drainage. *Society of Petroleum Engineers Journal*, 20(3):139–150, 1980.

G. Hamon and J. Vidal. Scaling-Up the Capillary Imbibition Process From Laboratory Experiments on Homogeneous and Heterogeneous Samples. *Proceedings of European Petroleum Conference*, 1986.

C. U. Hatiboglu and T. Babadagli. Oil recovery by counter-current spontaneous imbibition: Effects of matrix shape factor, gravity, IFT, oil viscosity, wettability, and rock type. *Journal of Petroleum Science and Engineering*, 59:106–122, 2007.

R. Helmig. *Multiphase flow and transport processes in the subsurface: a contribution to the modeling of hydrosystems.* Springer-Verlag, 1997.

A. Hill and G. Thomas. A new approach for simulating complex fractured reservoirs. *Middle East Oil Technical Conference and Exhibition, Society of Petroleum Engineers*, 1985.

H. Hoteit and A. Firoozabadi. An efficient numerical model for incompressible two-phase flow in fractured media. *Advances in Water Resources*, 31(6):891–905, 2008a.

H. Hoteit and A. Firoozabadi. Numerical modeling of two-phase flow in heterogeneous permeable media with different capillarity pressures. *Advances in Water Resources*, 31(1):56–73, 2008b.

H. Hoteit and A. Firoozabadi. An efficient numerical model for incompressible two-phase flow in fractured media. *Advances in Water Resources*, 31(6):891–905, 2008c.

R. Huber and R. Helmig. Multiphase flow in heterogeneous porous media: A classical finite element method versus an implicit pressure - explicit saturation-based mixed finite element - finite volume approach. *International Journal for Numerical Methods in Fluids*, 29(8):899–920, 1999.

M. Hui, B. Gong, M. Karimi-Fard, and L. Durlofsky. Development and Application of New Computational Procedures for Modeling Miscible Gas Injection in Fractured Reservoirs. *Proceedings of SPE Annual Technical Conference and Exhibition*, pages 1–11, 2007.

M. Hui, B. Mallison, and K. Lim. An Innovative Workflow to Model Fractures in a Giant Carbonate Reservoir. *International Petroleum Technology Conference, Kuala Lumpur, Malaysia, December*, 2008.

M. R. Hui, B. Mallison, M. Heidary-Fyrozjaee, W. Narr, and C. Energy. Spe 166075 the upscaling of discrete fracture models for faster, coarse-scale simulations of ior and eor processes for fractured reservoirs. *Proceedings of SPE Annual Technical Conference and Exhibition, New Orleans, Louisiana, USA, September*, 2013.

P. S. Huyakorn, S Panday, and Y. S. Wu. A three-dimensional multiphase flow model for assesing NAPL contamination in porous and fractured media, 1. Formulation. *Journal of Contaminant Hydrology*, 16:109–130, 1994.

M. Jackson, A. Muggeridge, M. Blunt, B. Tollit, C. Pain, D. Pavlidis, A. El-Sheikh, and J. Gomes. Reservoir Modeling for Flow Simulation Using Surfaces, Adaptive Unstructured Meshes, and Control-Volume-Finite-Element Methods. In *Proceedings of 2013 SPE Reservoir Simulation Symposium*. Society of Petroleum Engineers, 2013.

P. Jenny, H. Tchelepi, and S. H. Lee. Unconditionally convergent nonlinear solver for hyperbolic conservation laws with S-shaped flux functions. *Journal of Computational Physics*, 228(20):7497–7512, 2009.

R. Juanes, J. Samper, and J. Molinero. A general and efficient formulation of fractures and boundary conditions in the finite element method. *International Journal for Numerical Methods in Engineering*, 54(12):1751–1774, 2002.

M. Karimi-Fard, B. Gong, and L. J. Durlofsky. Generation of coarse-scale continuum flow models from detailed fracture characterizations. *Water Resources Research*, 42:W10423, 2006.

H. Kazemi and J. R. Gilman. Multiphase flow in fractured petroleum reservoirs. *Flow and contaminant transport in fractured rock*, pages 267–323, 1993.

H. Kazemi, L. S. Merrill, K. L. Porterfield, and P. R. Zeman. Numerical simulation of water-oil flow in naturally fractured reservoirs. *Society of Petroleum Engineers Journal*, 16(6):317–326, 1976.

H. Kazemi, J. R. Gilman, and A. M. Elsharkawy. Analytical and numerical solution of oil recovery from fractured reservoirs with empirical transfer functions. *SPE Reservoir Engineering*, 7(2):219–227, 1992.

J. G. Kim and Milind D. Deo. Finite element, discrete-fracture model for multiphase flow in porous media. *AIChE Journal*, 46(6):1120–1130, 2000.

P. Lemonnier and B. Bourbiaux. Simulation of Naturally Fractured Reservoirs. State of the Art Part1. *Oil & Gas Science and Technology - Revue de l'Institut Français du Pétrole*, 65(2):239–262, 2010.

K. A. Lie, S. Krogstad, I. S. Ligaarden, J. R. Natvig, H. M. Nilsen, and B Skaflestad. Open-source matlab implementation of consistent discretisations on complex grids. *Computational Geosciences*, 16(2):297–322, 2012.

K. T. Lim and K Aziz. Matrix-fracture transfer shape factors for dual-porosity simulators. *Journal of Petroleum Science and Engineering*, 13:169–178, 1995.

H. Lu, G. Di Donato, and M. J. Blunt. General transfer functions for multiphase flow in fractured reservoirs. *SPE Journal*, 13(3):289–297, 2008.

S. Ma, N. R. Morrow, and X. Zhang. Generalized scaling of spontaneous imbibition data for strongly water-wet systems. *Journal of Petroleum Science and Engineering*, 18(3-4):165–178, 1997.

S. Ma, X. Zhang, and N. R. Morrow. Influence of fluid viscosity on mass transfer between rock matrix and fractures. *Journal of Canadian Petroleum Technology*, 38 (07), 1999.

C. Maier and S. Geiger. Combining Unstructured Grids, Discrete Fracture Representation and Dual-Porosity Models for Improved Simulation of Naturally Fractured Reservoirs. *Proceedings of SPE Reservoir Characterisation and Simulation Conference and Exhibition*, 2013.

C. Maier, K. S. Schmid, M. Ahmed Elfeel, and S. Geiger. Multi-rate Mass-transfer Dual-porosity Modelling Using the Exact Analytical Solution for Spontaneous Imbibition - (SPE-164926). 2013.

C. Maier, K. S. Schmid, and S. Geiger. A multi-rate dual-porosity model using analytical solution for spontaneous imbibition. *Submitted to Advances in Water Resources*, 2014.

C. C. Mattax and J. R. Kyte. Imbibition of Oil Recovery from Fractured, Water-Drive Reservoir. *SPE Journal*, 2(177–184), 1962.

S. K. Matthai and M. Belayneh. Fluid flow partitioning between fractures and a permeable rock matrix. *Geophysical Research Letters*, 31(7), 2004.

S. K. Matthai and H. M. Nick. Upscaling two-phase flow in naturally fractured reservoirs. *AAPG Bulletin*, 93(11):1621–1632, 2009.

S. K. Matthai, S. Geiger, S. G. Roberts, A. Paluszny, M. Belayneh, A. Burri, A. Mezentsev, H. Lu, D. Coumou, T. Driesner, and C. A. Heinrich. Numerical simulation of multi-phase fluid flow in structurally complex reservoirs. *Geological Society, London, Special Publications*, 292(1):405–429, 2007.

D. B. McWhorter and D. K. Sunada. Exact integral solutions for two-phase flow. *Water Resources Research*, 26(3):399–413, 1990.

H. W. Meinardus, V. Dwarakanath, J. Ewing, G. J. Hirasaki, R. E. Jackson, M. Jin, J. S. Ginn, J. T. Londergan, C. A. Miller, and G. A. Pope. Performance assessment of NAPL remediation in heterogeneous alluvium. *Journal of contaminant hydrology*, 54:173–193, 2002.

C. Milliotte and S. K. Matthai. From seismic interpretation to reservoir model: an integrated study accounting for the structural complexity of the Vienna Basin using an unstructured reservoir grid. *First Break*, 32(5):95–101, 2014.

B. Montaron. Carbonate Evolution. *Oil & Gas Middle East*, 2008.

J. E. P. Monteagudo and A. Firoozabadi. Control-volume method for numerical simulation of two-phase immiscible flow in two- and three-dimensional discrete-fractured media. *Water Resources Research*, 40(7), 2004.

J. E. P. Monteagudo and A. Firoozabadi. Comparison of fully implicit and IMPES formulations for simulation of water injection in fractured and unfractured media. *International Journal for Numerical Methods in Engineering*, 69(4):698–728, 2007a.

J. E. P. Monteagudo and A. Firoozabadi. Control-volume model for simulation of water injection in fractured media: Incorporating matrix heterogeneity and reservoir wettability effects. *SPE Journal*, 12(3):355–366, 2007b.

N. R. Morrow and G. Mason. Recovery of oil by spontaneous imbibition. *Curr. Opin. Colloid Interface Sci.*, 6:321, 2001.

W. Narr, D. S. Schechter, and L. B. Thompson. Naturally fractured reservoir characterization. *Society of Petroleum Engineers*, 2006.

R. A. Nelson. Geologic analysis of naturally fractured reservoirs. *Gulf Professional Publishing*, 2001.

H. M. Nick and S. K. Matthai. Comparison of three fe-fv numerical schemes for single- and two-phase flow simulation of fractured porous media. *Transport in Porous Media*, 90(2):421–444, 2011.

J. Niessner, R. Helmig, H. Jakobs, and J. E. Roberts. Interface condition and linearization schemes in the Newton iterations for two-phase flow in heterogeneous porous media. *Advances in Water Resources*, 28(7):671–687, 2005. ISSN 03091708.

J. Nocedal and S. J. Wright. *Numerical Optimization*. Springer, New York, 1999.

M. J. Oak. Three-phase relative permeability of water-wet berea. In *Proceedings of SPE/DOE Enhanced Oil Recovery Symposium*. Society of Petroleum Engineers, 1990.

S. O. Ochs, H. Class, A. Färber, and R. Helmig. Methods for predicting the spreading of steam below the water table during subsurface remediation. *Water Resources Research*, 46:W05520, 2010.

M. Oda. Permeability tensor for discontinous rock masses. *Geotechnique*, 35(4): 483–495, 1985.

M. Oda. An equivalent continuum model for coupled stress and fluid flow analysis in jointed rock masses. *Water Resources Research*, 22(13):1845–1856, 1986.

N. E. Odling. Scaling and connectivity of joint systems in sandstones from western Norway. *Journal of Structural Geology*, 19(10):1257–1271, 1997.

N. E. Odling, P Gillespie, B. Bourgine, C. Castaing, J. P. Chiles, N. P. Christensen, E. Fillion, A. Genter, C. Olsen, L. Thrane, R. Trice, E. Aarseth, J. J. Walsh, and J. Watterson. Variations in fracture system geometry and their implications for fluid flow in fractured hydrocarbon reservoirs. *Petroleum Geoscience*, 5(4): 373–384, 1999.

J. Oh, K. Kim, W. S. Han, T. Kim, J. Kim, and E. Park. Experimental and numerical study on supercritical CO2/brine transport in a fractured rock: Implications of mass transfer, capillary pressure and storage capacity. *Advances in Water Resources*, 62:442–453, 2013.

A. Paluszny, S. K. Matthäi, and M. Hohmeyer. Hybrid finite element-finite volume discretization of complex geologic structures and a new simulation workflow demonstrated on fractured rocks. *Geofluids*, 7(2):186–208, 2007.

M. N. Panda, J. G. Ambrose, G. Beuhler, and P. L. McGuire. Optimized EOR design for the Eileen West End area, Greater Prudhoe Bay. *SPE Reservoir Evaluation & Engineering*, Feb:25–32, 2009.

T. W. Patzek, F. Male, and M. Marder. Gas production in the Barnett Shale obeys a simple scaling theory. *Proceedings of the National Academy of Sciences of the United States of America*, 110(49), 2013.

B. Pedrera, H. Bertin, G. Hamon, and A. Augustin. Wettability Effect on Oil Relative Permeability During a Gravity Drainage. In *Proceedings of SPE Annual Technical Conference and Exhibition*. Society of Petroleum Engineers, 2002.

K. Pruess and T. N. Narasimhan. A practical method for modeling fluid and heat flow in fractured porous media. *Society of Petroleum Engineers Journal*, Feb: 14–26, 1985.

P. Quandalle and J. C. Sabathier. Typical features of a multipurpose reservoir simulator. *SPE Reservoir Engineering*, 4(4):475–480, 1989.

V. Reichenberger, H. Jakobs, P. Bastian, and R. Helmig. A mixed-dimensional finite volume method for two-phase flow in fractured porous media. *Advances in Water Resources*, 29(7):1020–1036, 2006.

J. C. Sabathier, B. J. Bourbiaux, M. C. Cacas, and S. Sarda. A New Approach of Fractured Reservoirs. In *Proceedings of International Petroleum Conference and Exhibition of Mexico*, pages 49–59. Society of Petroleum Engineers, 1998.

A. Sahni. Measurement Scanning of Three Phase Relative Permeability during Gravity Drainage using CT. In *Thesis, Stanford University, USA*, 1998.

A. Saidi. Simulation of naturally fractured reservoirs. *SPE Reservoir Simulation Symposium*, (SPE 12270), 1983.

T. H. Sandve, I. Berre, and J. M. Nordbotten. An efficient multi-point flux approximation method for Discrete Fracture-Matrix simulations. *Journal of Computational Physics*, 231(9):3784–3800, 2012.

K. S. Schmid and S. Geiger. Universal scaling of spontaneous imbibition for water-wet systems. *Water Resources Research*, 48(3):1–13, 2012.

K. S. Schmid and S. Geiger. Universal scaling of spontaneous imbibition for arbitrary petrophysical properties: Water-wet and mixed-wet states and Handy's conjecture. *Journal of Petroleum Science and Engineering*, pages 1–18, 2013.

K. S. Schmid, S. Geiger, and K. S. Sorbie. Semianalytical solutions for cocurrent and countercurrent imbibition and dispersion of solutes in immiscible two-phase flow. *Water Resources Research*, 47(2):W02550, 2011.

K. S. Schmid, S. Geiger, and K. S. Sorbie. Higher order fe-fv method on unstructured grids for transport and two-phase flow with variable viscosity in heterogeneous porous media. *Journal of Computational Physics*, 2013.

J. Šimůnek, N. J. Jarvis, M. T. van Genuchten, and A. Gärdenäs. Review and comparison of models for describing non-equilibrium and preferential flow and transport in the vadose zone. *Journal of Hydrology*, 272:14–35, 2003.

G. Strang. On the construction and comparison of difference schemes. *SIAM Journal on Numerical Analysis*, 5(3):506–517, 1968.

K. Stueben, T. Clees, H. Klie, B. Lu, and M. Wheeler. Algebraic Multigrid Methods (AMG) for the Efficient Solution of Fully Implicit Formulations in Reservoir Simulation. In *Proceedings of SPE Reservoir Simulation Symposium*. Society of Petroleum Engineers, 2007.

R. D. Sydansk and L Romero-Zeron. Reservoir conformance improvement. *Society of Petroleum Engineers*, 2011.

Z. Tavassoli, R. W. Zimmerman, and M. J. Blunt. Analytic analysis for oil recovery during counter-current imbibition in strongly water-wet systems. *Transport in Porous Media*, 58:173–189, 2005.

J. Tecklenburg, I. Neuweiler, M. Dentz, J. Carrera, S. Geiger, C. Abramowski, and O. Silva. A non-local two-phase flow model for immiscible displacement in highly heterogeneous porous media and its parametrization. *Advances in Water Resources*, 62, Part C(0):475–487, 2013.

L. K. Thomas, T. N. Dixon, and R. G. Pierson. Fractured reservoir simulation. *Society of Petroleum Engineers Journal*, 23(1):42–54, 1983.

P. H. Valvatne and M. J. Blunt. Predictive pore-scale modeling of two-phase flow in mixed wet media. *Water Resources Research*, 40:W07406, 2004.

N. R. Warpinski, M. J. Mayerhofer, M. C. Vincent, C. L. Cipolla, and E. P. Lolon. SPE 114173 Stimulating Unconventional Reservoirs : Maximizing Network Growth while Optimizing Fracture Conductivity. *SPE Unconventional Reservoirs Conference, Keystone, Colorado, U.S.A.*, (February), 2008.

J. E. Warren and P. J. Root. The behavior of naturally fractured reservoirs. *Society of Petroleum Engineers Journal*, 3(3):245–255, 1963.

H. J. Welge. A simplified method for computing oil recovery by gas or water drive. *Journal of Petroleum Technology*, 4(04), 1952.

M. Wheeler and I. Yotov. A multipoint flux mixed finite element method. *SIAM Journal on Numerical Analysis*, 44(5):2082–2106, 2006.

R. M. Younis, H. A. Tchelepi, and K. Aziz. Adaptively Localized Continuation-Newton Method–Nonlinear Solvers That Converge All the Time. *SPE Journal*, 15(2):526–544, 2010.

X. Zhang, N. Morrow, and S. Ma. Experimental Verification of a Modified Scaling Group for Spontaneous Imbibition. *SPE Reservoir Engineering*, 11(4):280–285, 1996.

D. Zhou, L. Jia, J. Kamath, and A. R. Kovscek. Scaling of counter-current imbibition processes in low-permeability porous media. *Journal of Petroleum Science and Engineering*, 33(1-3):61–74, 2002.

R. W. Zimmerman, T. Hadgu, and G. S. Bodvarsson. A new lumped-parameter model for flow in unsaturated dual-porosity media. *Advances in Water Resources*, 19(5):317–327, 1996.